Hybrid spin registers in NV centers: A testbed for studying quantum thermodynamic phenomena and their derived applications

May 30, 2022

Master thesis

Promotor: prof. dr. Milos Nesladek
Copromotor: prof. dr. Jacques Tempere
Copromotor: dr. Abhishek Shukla
Academic year 2021-2022

Offered to you by:
Boo Carmans

Universiteit Antwerpen

UHASSELT

Contents

1 List of abbreviations

AQST	amplitude quantum state tomography
CD	counteradiabatic driving
CNOT	controlled NOT
CVD	chemical vapor deposition
CW	continuous wave
ENDOR	electron nuclear double resonance
ESR	electron spin resonance
HPHT	high-pressure high-temperature
ISC	intersystem crossing
MW	microwave
NMR	nuclear magnetic resonance
NV	nitrogen-vacancy
ODMR	optical detection of magnetic resonance
PL	photoluminescence
PQST	phase quantum state tomography
QND	quantum non-demolition
QNMR	quantum nuclear magnetic resonance
QST	quantum state tomography
RF	radiofrequency
SNR	signal to noise ratio
STA	shortcuts to adiabaticity
ZFS	zero field splitting
ZPL	zero phonon line

2 Abstract

The nitrogen-vacancy (NV) center, a point defect occurring in diamond, provides new possibilities in quantum thermodynamics and quantum information science, triggering vivid theoretical and experimental activity. The centers offer atom-like properties (e.g. long spin coherence times and well-defined optical transitions), while being enclosed in a robust diamond material, enabling a scalable, room temperature quantum technology. In this master thesis, a theoretical framework for an NV-mediated quantum Otto cycle (based on an existing, experimentally demonstrated Otto cycle protocol) and initial thermal state preparation is presented and experimental steps are taken to provide the means for its implementation. In a first step, the NV electron spin is manipulated and read out employing continuous wave and pulsed optical detection of magnetic resonace (ODMR), and Rabi measurements. The electron π-pulse was ~ 800 ns, long enough to resolve the hyperfine structure in a pulsed ODMR experiment. This enables to apply narrowband nuclear spin-selective microwave pulses, resulting in the possibility of electron-nuclear double resonance measurements of the ^{14}N nuclear spin associated with the NV center. Pulsed ODMR and Rabi measurements are conducted on this nuclear spin and reveal a resonance frequency of 7.11 MHz for the $|m_S, m_I\rangle = |-1, 1\rangle \leftrightarrow |-1, 0\rangle$ transition, and a nuclear π-pulse of $\sim 16.5\mu$s. Using the electron and nuclear control parameters (resonance frequencies and π-pulse durations), the NV two-qubit system is initialized to the $|0, 0\rangle$ state with a sufficient polarization to increase the contrast of nuclear Rabi oscillations between states $|0\rangle_N$ and $|1\rangle_N$ approximately twofold. For this, the used pulse protocols had to be optimized for the laser pulse duration and the negative effects of applying RF waves: resonance frequency shift and sample drift. Lastly, nuclear state preparation and quantum state tomography (QST) protocols are introduced. The QST protocols are based on the adjacent measurements of Rabi oscillations of a reference state $|0\rangle_N$ and Rabi oscillations of the prepared state $|\psi\rangle$ around the x- and y-axis of the Bloch sphere. From inspection of these Rabi oscillations, using three different calculation protocols (based on either the amplitude or the phase of the Rabi signals) a maximum two-qubit fidelity of 0.9995 is obtained across seven measurements of three different states.

3 Samenvatting

Kwantum thermodynamica is een relatief recente tak van de fysica die de laatste jaren met grote interesse werd bestudeerd en die een bijzondere contributie heeft geleverd aan de ontwikkeling van nieuwe kwantum technologieën. Om een schaalbare kwantum technologie te kunnen creëren, moet voldaan worden aan twee contrasterende eisen. Enerzijds moeten de qubits precies te controleren zijn, anderzijds moet de technologie ook op industriële schaal kunnen worden vervaardigd. Een precieze qubit controle is reeds bewezen, bijvoorbeeld met supergekoelde atomen, maar tenzij iedereen in de toekomst een voorraad vloeibare stikstof in huis heeft, is deze technologie niet schaalbaar. Het kan dus dat de technologie van de toekomst niet koud wordt, maar wel glanzend: diamanten kwantum technologie is namelijk wel bijzonder schaalbaar, en significante verbeteringen worden geboekt in de controle van de vastestof qubits.

Diamant bestaat uit een tetrahedraal netwerk van koolstofatomen in een sp^3-hybridisatie. In het rooster kunnen defecten voorkomen, zoals ontbrekende atomen (gaten), dislocaties en interstitiële of substitutionele atomen, waarbij stikstof het vaakst voorkomt. Een specifiek puntdefect dat in diamanten kan voorkomen is het *nitrogen-vacancy* (NV) centrum, wat vertaald kan worden als het stikstof-gat centrum. Deze NV centra bestaan uit een substitutioneel stikstof atoom gekoppeld met een naburig gat en hebben de eigenschappen van geïsoleerde atomen, ondanks dat ze vastzitten langs één van de kristallografische assen van het diamantrooster. Dat maakt dat ze voldoen aan beide contrasterende eisen en een veelbelovend alternatief vormen voor de supergekoelde kwantum technologie. NV centra kunnen voorkomen in twee ladingstoestanden: neutraal (NV^0) of negatief geladen (NV^-). De negatief geladen centra zijn het meest abondant en worden ook gebruikt in deze thesis.

De Hamiltoniaan van een NV^- centrum in een extern magnetisch veld bevat bij benadering vijf termen: de nulveldsplitsing, het elektron Zeeman effect, de hyperfijnsplitsing, het nuclear quadrupool effect, en het kern Zeeman effect. Voor de doelen gesteld in deze masterproef kan deze Hamiltoniaan verder worden vereenvoudigd. Zo is de kern Zeeman term bijvoorbeeld erg klein en kan deze worden verwaarloosd tegenover de andere effecten. Daarnaast wordt ook enkel rekening gehouden met de kernspin van het stikstofatoom ^{14}N van het NV centrum zelf en niet met andere kernen die eventueel in het diamantrooster nog aanwezig kunnen zijn. Ten laatste is bij het gebruikte magneetveld enkel de component parallel met de NV as van belang en zorgt de aanwezigheid van het veld ervoor dat het effect van de transversale nulveldsplitsing verwaarloosbaar wordt. Deze aannames in gedachten wordt de benaderende Hamiltoniaan gegeven in formule 3 op pagina 18. De eigentoestanden van het systeem worden dan gegeven door $|S, m_S\rangle \otimes |I, m_I\rangle$ met S de spin van het ongepaarde NV elektron $S = 1$, $m_S = -1, 0, 1$ en I de kernspin van het stikstofatoom $I = 1$, $m_I = -1, 0, 1$. De bijbehorende eigenwaarden geven het spectrum van energietoestanden. Een aantal configuraties zijn hierbij belangrijk en kunnen worden afgeleid m.b.v. moleculaire orbitaaltheorie. Het is het eenvoudigste om hierbij eerst enkel te kijken naar het effect van de nulveldsplitsing en daarna de andere termen één voor één mee in acht te nemen, waarop de bekomen energieniveaus steeds verder opsplitsen. Dit is geïllustreerd in figuren 2 op pagina 18 en 3 op pagina 19.

De elektron spin van het NV centrum kan makkelijk optisch worden uitgelezen via *Optical Detection of Magnetic Resonance* (ODMR) en ook simpel optisch worden gepolariseerd. Hiervoor wordt het NV centrum geëxciteerd met groen laserlicht, waarna het terug naar de grondtoestand relaxeert via spin-afhankelijke paden. Als de electron spin van het NV centrum wordt gegeven door m_S = 0, dan zal het systeem na excitatie relaxeren via een radiatieve transitie, die spinbehoudend is. Als de electron spin gelijk is aan ± 1, dan vergroot de kans dat het systeem relaxeert via een donkere transitie, die de spin polariseert naar $m_S = 0$. Op deze manier kan de NV elektron spin op een tijd van enkele honderden nanoseconden tot 90$\%$ worden gepolariseerd naar $m_S = 0$. Voor de kernspin ontbreken deze eenvoudige uitlees- en polarisatieprocedures, maar het is wel mogelijk om de kernspin te manipuleren en uit te lezen via de elektronspin. Dit is één van de grote onderdelen van deze masterproef en beslaat de gehele sectie 7.1. Hierbij wordt als eerste op de elektron spin gefocust. Het protocol voor *continuous wave* ODMR wordt uitgelegd en het resultaat gedemonstreerd, alsook metingen van Rabi oscillaties tussen $m_s = 0$ en $m_S = -1$ (zie figuur 17 op pagina 57 en 18 op pagina 59). Rabi metingen tonen aan dat de π-puls $\sim$ 800 ns bedraagt. Dit is een vrij grote waarde zodat de hyperfijn resonanties onderscheiden kunnen worden in een gepulste ODMR meting.

Nadat de elektronspin kan worden gecontroleerd en uitgelezen, wordt er gefocust op de kernspin. Een nucleair Rabi protocol en een nucleaire ODMR worden uitgevoerd om de resonantie frequenties en de duratie van de nucleaire π-puls te bepalen (zie figuur 19 op pagina 60 en 20 op pagina 61). Hieruit volgen een π-puls van ~ 16.5 μs aan en een resonantiefrequentie van ~ 7.11 MHz voor de $m_I = 0 \leftrightarrow m_I = 1$ transitie in de elektronisch geëxciteerde toestand

$m_S = -1$. Deze waarden kunnen worden gebruikt in nucleaire protocollen, zoals een nucleaire spin polarisatie en een nucleaire Rabi met deze initialisatie. De eerste van deze sequenties is een uitbreiding van de elektron polarisatie en brengt het NV centrum naar de toestand $m_S = 0$, $m_I = 0$. De graad van polarisatie wordt uitgelezen met een gepulste ODMR meting van de elektron spin. Met een volledig gedepolariseerde nucleaire toestand zijn namelijk drie even grote hyperfijn pieken te zien voor één elektronische overgang (maximaal gemengde toestand van de drie kernspins), terwijl bij een volledig gepolariseerde nucleaire spin slechts één hyperfijn piek te zien is met een contrast dat drie keer zo groot is. Dit is te zien in figuur 22 op pagina 63 samen met gebruikte puls sequentie. De bekomen polarisatie is niet volledig en er blijft een kleine residuele populatie met spin verschillend van nul achter zodat de contrastverhoging beperkt blijft. Dan pas ik de vooraf gebruikte nucleaire Rabi sequentie aan door steeds eerst de nucleaire spin te polariseren tot $m_I = 0$ en vervolgens Rabi oscillaties tussen deze toestand en $m_I = 1$ op te meten (zie figuur 23 op pagina 64). De bekomen oscillaties hebben een contrast dat ongeveer tweemaal zo groot is als dat van Rabi oscillaties zonder initialisatie.

Om een optimale controle over de elektron en kernspin te verkrijgen, optimaliseer ik de gebruikte puls sequentie. De duratie en frequentie van de gebruikte microgolf en radiofrequente pulsen werd al onderzocht a.d.h.v. Rabi en ODMR metingen, maar ook de duratie van de laserpulsen is belangrijk. Deze moeten namelijk lang genoeg zijn om de elektronspin te polariseren naar $m_S = 0$, maar ook voldoende kort zodat de kernspin niet wordt gedepolariseerd. Via een parameterstudie wordt een optimale waarde van 500 ns bekomen voor de laserpuls duratie bij een laservermogen van 1 mW. Vervolgens wordt het effect van radiofrequente magnetische velden ook in detail bestudeerd. Wanneer veel of lange RF pulsen worden aangelegd, is er namelijk een verhoogde *sample drift* zodanig dat het NV centrum snel de focus van de laser verlaat. Om dit effect tegen te gaan, wordt een *target lock* functie ingebouwd in de meetsoftware om het NV centrum in focus te houden. Naast een drift in de locatie is er ook een verandering te zien van de resonantiefrequenties (meer bepaald van de nulveldsplitsing) naar lagere frequenties bij aanleg van langere of meer RF pulsen. Dit onverwachte gedrag wordt gelinkt aan de opwarming van het diamantsample en genoodzaakt dat de resonantiefrequenties opnieuw worden opgemeten bij elke (grote) verandering van de tijd waarin het sample wordt blootgesteld aan radiofrequente straling.

Een tweede onderdeel van deze thesis bekijkt de NV elektron en kernspin als effectieve twee-niveau systemen, zodat ze equivalent zijn aan twee spin qubits. Deze qubits kunnen in tegenstelling tot klassieke bits niet enkel in toestand $|0\rangle$ of $|1\rangle$ zijn, maar ook in elke lineaire combinatie van deze twee toestanden. In de experimenten in deze masterproef, zal de kernspin als qubit worden behandeld met de twee toestanden $m_I = 0$ en $m_I = 1$. Een algemene toestand van de kernspin qubit wordt dan gegeven door $|\psi\rangle_N = cos(\frac{\theta_N}{2}) + e^{i\phi_N} sin(\frac{\theta_N}{2})$, zodat onmiddellijk voldaan is aan de normalisatieconditie en een toestand dus bepaald wordt door twee hoeken θ_N en ϕ_N. Op deze manier stelt elk punt op de Blochsfeer een mogelijke toestand voor. Verder kan ook gebruikt worden gemaakt van de densiteitsoperator ρ_N om de kernspin qubit toestanden voor te stellen.

Met een meetprocedure genaamd *Quantum State Tomography* (QST) kunnen de elementen van de densiteitsoperator (en dus θ_N en ϕ_N) worden bepaald. In deze thesis worden twee specifieke protocollen gebruikt die beiden zijn gebaseerd op Rabi metingen: een amplitudo QST (AQST) en fase QST (PQST). Hiervoor werd het experimenteel protocol ontworpen o.b.v. een electron QST, de AQST berekeningen werden geoptimaliseerd en de PQST methode werd volledig zelf ontworpen. AQST maakt gebruik van de amplitudo van drie opeenvolgende Rabi oscillaties: één Rabi meting van rotaties rond de x-as (x-Rabi), één meting van oscillaties rond de y-as (y-Rabi) en één referentie Rabi tussen toestanden $|0\rangle_N$ en $|1\rangle_N$ om met deze maximale amplitudo de andere twee te normaliseren (de straal van de Blochsfeer is 1). Uit de ratio's van de verschillende amplitudo's en de vorm van de x- en y-Rabi signalen, kunnen dan de coördinaten (x, y, z) oftewel (θ_N, ϕ_N) van de Bloch vector worden bepaald met de formules (12) tot (14) op pagina 27 en 28. PQST gebruikt enkel de x- en y-Rabi en maakt gebruik van fase-informatie om θ_N en ϕ_N te bepalen, via formule (17) en (18) op pagina 29. Vanwege de sterke aanwezigheid van *sample drift* tijdens de metingen, is de fasegebaseerde methode succesvoller hier. De amplitudogebaseerde methode heeft echter als voordeel dat met de derde Rabi meting redundantie wordt ingebracht, zodat het resultaat op interne consistentie kan worden gecontroleerd. Hoe goed beide methodes werken kan worden gekwantificeerd a.d.h.v. de *fidelity* van een meting van een gekende toestand. Deze grootheid drukt uit in hoeverre de gekende en gemeten toestand overeen komen op een schaal van 0 tot 1. Een andere methode is om de Rabi oscillaties van de gekende toestand te plotten over de experimentele data en deze te vergelijken. Het QST protocol werd toegepast op een aantal nucleaire toestanden in verschillende regio's van de Blochsfeer. In nabijheid van de assen is het moeilijker om een toestand correct op te meten, maar behaalde ik toch een 2-qubit *fidelity* van minstens 0.9962 met de fasegebaseerde methode en een *fidelity* van 0.9733 met de amplitudogebaseerde methode. Op een algemene toestand, dus niet op de limiet van het meetbereik, behaalde ik maximaal een *fidelity* van 0.9995 met de fasegebaseerde methode en 0.9985 met de amplitudogebaseerde methode. Om deze waarden te kunnen behalen, werkte ik met het contrast van de Rabi oscillaties als amplitudo, i.p.v. de gemeten intensiteit. Voornamelijk bij aanwezigheid van *sample drift* verbeterde dit de resultaten.

Het laatste onderwerp dat in deze thesis wordt aangesneden is het gebruik van NV centra in een kwantum Otto cyclus. Kwantum motoren zijn een uitbreiding van de gekende klassieke motoren, zoals de Carnot of Otto motor, en kunnen worden gebruikt om warmte om te zetten in arbeid. Het verschil tussen deze klassieke en kwantum motoren ligt voornamelijk in de interpretatie van de thermodynamische variabelen van arbeid, warmte, volume en temperatuur. Via inspectie van een klassieke Otto cyclus kan worden afgeleid dat een kwantum motor kan worden gerealiseerd in elk systeem met ten minste twee verschillende energieniveaus die onder een tijdsafhankelijke Hamiltoniaan evolueren. Het leveren van/ ondergaan van arbeid wordt hier geïnterpreteerd als het verkleinen/ vergroten van de kloof tussen de twee energieniveaus van het twee-niveau systeem. Het opnemen of afgeven van warmte wordt in de kwantum thermodynamica geïnterpreteerd als het exciteren van populatie naar de toestand met hogere energie of het relaxeren van populatie naar de toestand met lagere energie. Op die manier is volume gerelateerd aan de energiekloof en temperatuur aan de populaties van de verschillende energieniveaus. Naast de interpretatie van de verschillende thermodynamische variabelen, verandert ook het concept van adiabatische overgangen. In de klassieke thermodynamica gebeuren deze overgangen snel, zodat er geen warmte met de omgeving kan worden uitgewisseld op de tijdsschaal van de overgang. In de kwantum thermodynamica betekent een adiabatische overgang echter dat er geen exctitaties mogen plaatsvinden, zodat de overgang quasistatisch moet gebeuren. Dit heeft echter het negatieve gevolg dat de vermogensuitvoer van de motor bij zulke lange overgangen daalt naar nul. In sectie 5.7.2 op pagina 39 wordt de kwantum Otto cyclus in een algemeen two-level systeem wiskundig besproken, waarna in de volgende sectie de netto geleverde arbeid en efficiëntie kunnen worden berekend en de positieve arbeid voorwaarde kan worden gesteld. In sectie 5.7.4 wordt een oplossing voor de de lage vermogensuitvoer besproken, namelijk het versnellen van de adiabatische overgangen door een proces genaamd *counteradiabatic driving*. Deze techniek gebruikt een externe controle Hamiltoniaan om ervoor te zorgen dat het systeem gedurende de hele overgang in de adiabatische eigentoestanden blijft en er geen excitaties kunnen gebeuren. Vervolgens wordt een mogelijke controle Hamiltoniaan voor een spinsysteem in een magneetveld $B_0(t)$ gegeven in formules (43) en (44) op pagina 45.

Met de voorgaande theoretische grondslag, stel ik een design voor een kwantum Otto motor prototype gebaseerd op NV centra in diamant voor. Dit materiaal werd reeds in 2017 gebruikt om kwantum effecten in microscopische motoren te demonsteren en bleef sindsdien erg interessant voor kwantum thermodynamica door zijn lange spin coherentie tijden, de mogelijkheid tot koppeling met nucleaire spinbaden in het diamantrooster en de optische polarisatie van de elektronenspin. Vooraleer in te gaan op de NV-gebaseerde Otto motor, wordt eerst een gelijkaardig systeem van een scalair gekoppelde ^{1}H en ^{13}C spin bekeken. Voor dit systeem werd een kwantum Otto cyclus reeds experimenteel gedemonstreerd, en de daarbij bekomen resultaten worden hier nagegaan. Vervolgens wordt beargumenteerd waarom een gelijkaardig protocol kan worden gebruikt met een NV electron en ^{14}N nucleaire spin (zie figuur 13 op pagina 49). Hierbij wordt ook een protocol voorgesteld om beide spins te initialiseren naar een bepaalde thermische toestand. Dit initialisatie protocol werd ook in zekere mate experimenteel getest, zoals te zien is op figuur 21 op pagina 62. Om ook effectief het volledige protocol te kunnen uitvoeren, moeten nog additionele experimenten verricht worden, bijvoorbeeld om de transitietempo's tussen verschillende energieniveaus onder laserlicht te bepalen.

4 Introduction

The field of thermodynamics is best known for its ability to represent reality with an amazingly small number of variables. For systems in equilibrium, the Hamiltonian is sufficient [1] to reconstruct the complete state of a system, from which then all other observables can be deduced. However, recent years were marked by an increasing interest in the thermodynamics of out-of-equilibrium quantum systems [2] [3]. Quantum thermodynamics, as the encompassing field is called, blends various branches of physics, such as quantum information science, quantum optics, condensed matter physics, etc. Theoretically, it argues that only a few additional variables are necessary to describe a quantum device such as a heat engine [1]. Apart from advances in the fundamental understanding of generalizing concepts of classical physics to the quantum realm, the field is also characterized by significant contributions to the development of new technologies that take advantage of quantum systems by actively manipulating them [4].

A scalable quantum technology requires meeting two conflicting demands, namely high precision control and easy scale-up. The first requirement is best fulfilled in single trapped atoms, but the second one is easier to find in solid-state, nanofabricated systems. In recent years, nitrogen-vacancy centers have emerged as a promising candidate platform for such a scalable quantum technology. These color centers offer atom-like properties such as long-lived spin states and well-defined optical transitions, but lie inside the robust solid-state material diamond, enabling not only the two demands but also room-temperature operation [5]. As the diamond lattice can contain other magnetic nuclei as well, the interactions between the NV electron spin and the nearby nuclei allow for NV-mediated access to individual nuclear spin states with extraordinarily long-lived quantum states exceeding 1 s [6]. In contrast to these long coherence times, the timescale on which the solid-state spins can be manipulated is very fast: electronic spin transitions can be driven in nanoseconds and nuclear spins can be rotated on microsecond timescales [5]. Because of this, the nearby nuclei can be used as additional states for logical operations or a long-lived quantum memory, and logical operations between qubits at short timescales can be performed by selectively exciting specific transitions within the multi-spin energy levels [5].

The benefit of using NV centers in quantum information science has been extensively investigated both theoretically and experimentally. Fundamental topics that were studied, included spin and charge dynamics, dynamical decoupling and dynamical nuclear spin polarization.

More advanced topics quickly followed. For example, NV centers in diamond were used to demonstrate a quantum error correction protocol [7] in 2016, which is paramount for large-scale quantum information processing. Last year, the standard quantum limit was beaten in ambient conditions [8] using an interferometer based on an NV electron spin, associated ^{14}N nuclear spin and a ^{13}C nuclear spin, allowing for more precise calculation than is typically achievable in room-temperature quantum systems. Furthermore, entanglement between two distant NV centers [9], multiparticle entanglement [10] and multiple quantum algorithms [11] [12] [13] have been demonstrated experimentally, thanks to the development of various quantum gates affecting either the NV electron spin, a nearby nuclear spin or both. A protocol for highly selective nuclear-nuclear quantum gates at room temperature has been proposed by Jiang and Chen. [14], showing fidelities higher than ~ 0.95. Also recently, NV centers have been used to control and read the state of synthetic polyproline with electron spins localized on molecular side groups, which lays the foundation for building larger quantum networks using well-established chemistry methods [15].

NV centers have also been extensively employed in quantum thermodynamics. For example, quantum signatures were demonstrated in an NV-based three-level quantum engine [16], the validity of quantum fluctuation relations in a driven open quantum system was experimentally verified for the first time using NV centers [17] and it was only last year that an autonomous dissipative Maxwell's demon was realized with a spin qutrit (three hyperfine states) formed by an NV center at room temperature [18].

But before one can venture further into the complex applications of NV centers in the field of quantum thermodynamics, one must first be able to perform simple quantum gates and realize simple quantum thermodynamic protocols. Therefore, the ultimate goal to which this work contributes is the construction of a quantum Otto engine based on nitrogen-vacancy centers in diamond, which will provide the foundation for more involved work later. In order to perform quantum operations, one must be able to control the electronic and nuclear spin of the NV center, as well as read out the spin state. Multiple protocols to control and read out the electronic and nuclear spin associated with an NV center are presented in and experimentally demonstrated, paving the way towards the practical implementation of the quantum Otto cycle.

5 Theory

5.1 The diamond lattice and different types of NV centers

The diamond lattice is formed by a rigid carbon network in sp^3-hybrid orbitals. Each of the carbon atoms is bound to four others in a tetrahedral structure, defining the four crystallographic axes. Defects such as vacancies, dislocations and interstitial or substitutional atoms occur naturally in this lattice. The most abundant impurity is nitrogen, and based on the amount of nitrogen impurities and their type, diamonds are usually classified in four categories [19]. The first type (Ia) occurs most commonly and has a high nitrogen percentage up to 0.3%. The second type (Ib) comprises mostly of synthetic diamonds and may contain up to 500 ppm of atomic nitrogen. Type IIa is rare and has a low nitrogen content. Lastly, type IIb is used to address p-type semiconductors. The aforementioned synthetic diamonds can be fabricated either by high-pressure high-temperature (HPHT) synthesis or by chemical vapor deposition (CVD).

A specific type of point defect that can be found in diamond material is the nitrogen-vacancy (NV) center, consisting out of a substitutional nitrogen atom and a vacancy replacing two neighboring carbon atoms. NV centers belong to the general class of color center defects, as their presence colors the transparent diamond in a purple to dark red hue. Although NV color centers have a similar behavior to isolated atoms in free space, they are confined in the solid-state lattice and aligned with the crystallographic axes [20] as shown in figure 1.

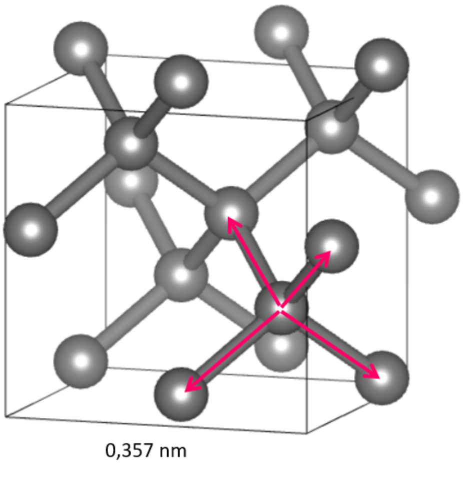

Figure 1: Diamond structure and crystallographic axes.

NV centers can occur in two different charge states: neutral (NV^0) or negatively charged (NV$^-$) [21]. When a nitrogen atom couples to a vacancy, three nitrogen electrons are used to form covalent bonds with neighboring carbon atoms and the remaining two form a lone pair. The vacancy contributes three electrons to the NV center (dangling bonds from the surrounding carbon atoms), of which two form a quasi-covalent bond and the third one remains unpaired. The complex is electrically neutral and has a C_{3V} symmetry with a threefold rotational axis through the NV bond axis. The unpaired vacancy electron is mostly responsible for the paramagnetic behavior of the NV^0 complex. In general, most NV centers capture an additional electron, which are often supplied by other impurities in the diamond lattice (e.g. substitutional nitrogen). The extra electron forms a spin pair with the third vacancy electron and is responsible for the extensive paramagnetic behavior of the NV$^-$ center. Theoretical evidence for a positively charged NV$^+$ center exists [22] and points out that it will most likely not be magneto-optically active. As the NV$^-$ center is mostly of highest interest for this thesis, it will simply be called NV center when there is no possible confusion.

5.2 The ground-state spin Hamiltonian of an NV$^-$ center

As the NV$^-$ center has a nonzero total spin magnetic moment, the Zeeman effect occurs whenever the center is being subjected to external magnetic fields. The Hamiltonian [23] and corresponding energetic spectrum will first be discussed in the absence of magnetic fields and then in their presence.

5.2.1 In absence of magnetic fields

Without external magnetic field, there are three contributions to the approximate ground-state spin Hamiltonian $\hat{H}$ of the NV defect: the zero-field splitting (ZFS), the hyperfine interaction with nearby nuclear spins (e.g. ^{14}N ($I = 1$), ^{15}N ($I = \frac{1}{2}$, ^{13}C ($I = \frac{1}{2}$), etc.), and the nuclear quadrupole effect.

$$\begin{aligned} \hat{H} &= \hat{H}_{ZFS} + \hat{H}_{HFS} + \hat{H}_Q \\ &= DS_z^2 + E(S_x^2 - S_y^2) + \textstyle\sum_{k=1}^{N} \mathbf{S} \cdot \mathbf{A}_k \cdot \mathbf{I}_k + \sum_{I_k > 1} \mathbf{I}_k \cdot \mathbf{P}_k \cdot \mathbf{I}_k \quad (1) \end{aligned}$$

Here the z-axis is taken to be the NV axis, D and E are the axial and transversal ZFS parameters, S_x, S_y and S_z are the components of the electron spin vector $\mathbf{S}$, $\mathbf{A}_k$ are hyperfine coupling tensors of the NV center to nearby nuclei with $\mathbf{I}_k$ ($k = 1$, ..., N) their respective spin vectors and $\mathbf{P}_k$ are the quadrupole tensors of these nuclear spins. D has a value of 2.87 GHz and depends on temperature, whereas the off-axis ZFS parameter E, which is always less than D, results from local strain in the diamond lattice. In high purity CVD grown diamonds E takes on values of around 100 kHz, in nanodiamonds this can rise to a few MHz [21].

5.2.2 In presence of magnetic fields

When magnetic fields are present, the Hamiltonian is expanded with one Zeeman term for each spin in the system (NV electron spin and possible surrounding nuclear spins). However, as the nuclear magneton is much smaller than the Bohr magneton for electrons, the nuclear Zeeman interaction is negligible for the purposes of this thesis and will be left out of the Hamiltonian. The full ground-state spin Hamiltonian of the NV defect in presence of an external magnetic field is then given by:

$$\begin{aligned} \hat{H} &= \hat{H}_{ZFS} + \hat{H}_{ZM} + \hat{H}_{HFS} + \hat{H}_{Q} \\ &= DS_z^2 + E(S_x^2 - S_y^2) + g\mu_B \mathbf{B} \cdot \mathbf{S} + \textstyle\sum_{k=1}^{N} \mathbf{S} \cdot \mathbf{A}_k \cdot \mathbf{I}_k + \sum_{I_k>1} \mathbf{I}_k \cdot \mathbf{P}_k \cdot \mathbf{I}_k \quad (2) \end{aligned}$$

Here, g is the Landé g-factor and μ_B the Bohr magneton. The E-splitting [21] relates mainly to external fields, strain and temperature and is smaller than the Zeeman splitting. It is rarely observed in presence of magnetic fields (which is the situation covered in this dissertation) and can therefore be omitted for further purposes. Additionally, the magnetic field $\mathbf{B}$ can be divided into a magnetic field component along the NV axis B_{NV} and a component perpendicular to it $\mathbf{B}_\perp = B_x\mathbf{e}_x + B_y\mathbf{e}_y$ (taking the NV axis in the z-direction). Two regimes can then be distinguished: the weak (< 100 mT [24]) and strong (> 100 mT) magnetic field regime [21]. In the weak field regime the transversal component of the magnetic field is small, so that the last term in the Hamiltonian can be left out and the energy dependence of the system on the magnetic field is approximately linear. In the strong field regime the energy is strongly correlated to the orientation of the magnetic field with respect of the color center and the NV axis no longer dictates the direction of the quantization axis. The projection of the spin along the NV axis, $|m_s\rangle$, is then no longer an eigenstate of the spin Hamiltonian, which leads to strong modifications of the spin dynamics of the NV center: spin polarization and spin dependent photoluminescence become inefficient and the contrast of resonance lines reduces (see further). Operation in the weak field is thus preferred and will be used in this thesis. In addition, the situation with the ^{14}N spin of the NV center as only nuclear spin will be investigated. Using the above approximations, the NV Hamiltonian can be written as:

$$\hat{H} = DS_z^2 + g\mu_B B_{NV} S_Z + AS_Z I_Z + PI_Z^2 \quad (3)$$

Instead of the hyperfine and quadrupole tensor, there are now only scalar constants. The electron - ^{14}N hyperfine coupling constant A is equal to -2.16 MHz and the nuclear quadrupole coupling constant P if the nitrogen nucleus is equal to -4.95 MHz [25].

5.3 The energetic structure of an NV center

Solving the Schrödinger equation using the Hamiltonian from formula 3 gives the possible states in which an NV center can occur and their corresponding energies. The eigenstates of the complete approximate Hamiltonian are given by a tensor product of the spin eigenstates $|S, m_S\rangle_e$ of the NV electron spin and $|I, m_I\rangle_N$ of the nitrogen nucleus, written in short notation as $|m_I, m_S\rangle$. When the hyperfine interaction is omitted, the eigenstates are simply the electronic eigenstates $|S, m_S\rangle_e$ (also written as $|m_S\rangle_e$ when there is no possible confusion).

The easiest way to understand the energy spectrum of the NV center is by starting with a Hamiltonian that only describes axial zero field splitting and then adding more terms and observing the changes.

5.3.1 Only axial zero field splitting

When there is only axial zero field splitting, the eigenstates of the system are purely electronic $|m_S\rangle_e$. In the ground state, the spin of the NV$^-$ center is S = 1 (triplet state) [21]. This can be seen using molecular orbitals. The NV$^-$ center has six electrons, which occupy four molecular orbitals. Filling these orbitals with electrons, it can be determined that the lowest energy state is a triplet state, also called the ^{3}A$_2$-state. This triplet state can have a magnetic spin quantum number of 0 (as is the case in the left molecular orbital (MO) scheme on figure 2a)), 1 (as in the right MO scheme) or -1 (similar to the right MO scheme, but with the top two spins inverted). The $|0\rangle_e$ state has the lowest energy, as can be seen in the many electron representation on the right of figure 2a) and the $|1\rangle_e$ and $|-1\rangle_e$ states are degenerate at higher energy. Depending on the temperature of the sample, a transition between the $|0\rangle_e$ and $|\pm 1\rangle_e$ degenerate state, can be invoked by a resonant microwave field around 2.87 GHz. A similar theory holds for a certain optically excited state of the NV center, the triplet ^{3}E state, for which the molecular orbitals (for $m_S = 0$ and $m_S = 1$) are shown in figure 2b), as well as the many electron representation.

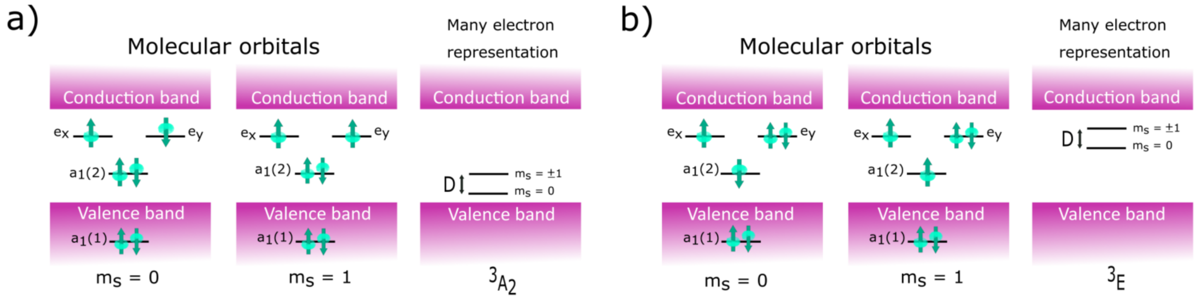

Figure 2: a) Molecular orbital and many electron representation of the ground spin triplet state ^{3}A$_2$ of the NV center. b) Molecular orbital and many electron representation of the excited spin triplet state ^{3}E of the NV center.

5.3.2 Effect of Zeeman splitting

The presence of a magnetic field [21] does not alter the energy of the $|0\rangle_e$ eigenstate, but lifts the degeneracy of the $|\pm 1\rangle_e$ state. As the magnetic moment associated with the spin of an electron always points opposite to this spin momentum, the energy of the aligned spin $|1\rangle_e$ will rise and the energy of the anti-aligned spin $|-1\rangle_e$ will drop. The energy difference is equal to $2g\mu_B B_{NV}$.

5.3.3 Effect of hyperfine and nuclear quadrupole interactions

For every NV center there is an associated nitrogen nuclear spin associated that also affects the electronic energy levels. The nitrogen atom can be either the ^{14}N isotope with spin $I = 1$ or the ^{15}N isotope with spin $\frac{1}{2}$. The abundancy [26] of the first isotope is much greater (naturally $99,63\%$), so that the occurrence of ^{15}N complexes is ignored. The interaction with ^{13}C nuclear spins is also not taken into account.

The effect of the hyperfine interaction and nuclear quadrupole effect depends on the values of both the electron and nuclear spin and results in a splitting of the electronic energy levels. The $|0\rangle_e$ level splits into two sublevels due to the nuclear quadrupole effect, whereas the other electronic levels split into three due to the hyperfine effect. Therefore the $|1\rangle_N$ and $|-1\rangle_N$ levels are degenerate for $|0\rangle_e$, but not for nonzero electronic spin. In practice, there will be a small gap between $|1\rangle_N$ and $|-1\rangle_N$ even in $|0\rangle_e$, because of the nuclear Zeeman effect. This can be ignored as the effect is very small and cannot be seen in the indicated transitions (it has the same effect on higher lying energy levels).

The total splitting of the energy levels shown in figure 2 due to the electron Zeeman effect, hyperfine coupling and nuclear quadrupole effect is illustrated in figure 3.

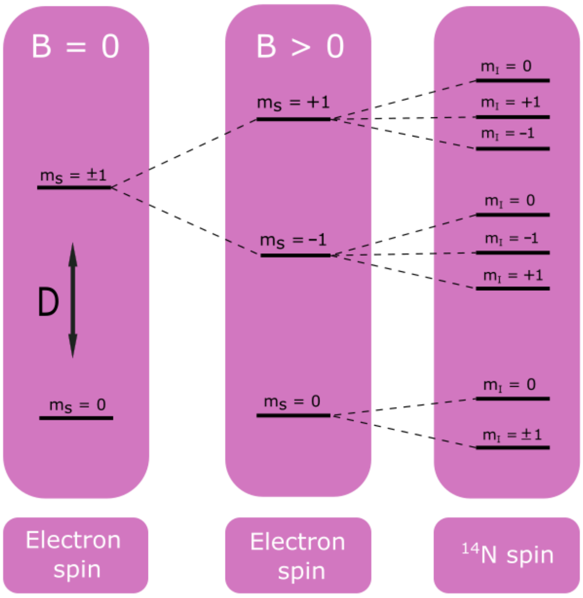

Figure 3: Splitting of the NV electronic energy levels due to the electron Zeeman effect, nuclear quadrupole effect and hyperfine coupling between the electronic and nuclear spin.

5.4 Optical manipulation and read-out of the NV spin state

In the previous paragraph, two possible states were described in which NV electrons can arrange themselves: the triplet ground state $^3A_2$ and a triplet excited state ^3E. In order to understand the optical properties of NV centers used in this thesis, two more energy levels need to be considered: the spin singlet states $^1A_1$ and ^1E. The energy of these states lies in the gap between $^3A_2$ and ^3E. The lifetime of the metastable ^1E state is around 300 ns and the lifetime of the $^1A_1$ state is $\sim$1 ns [27].

5.4.1 Polarization of the electron spin

One of the advantages of working with NV centers is that their electronic spin can be easily polarized. To see how, a schematic drawing of the electronic energy levels of interest (in presence of magnetic fields, but without hyperfine interaction) is presented in figure 4. The states $^3A_2$, ^3E, $^3A_1$ and ^1E are shown as purple boxes, wherein the spin-dependent energy levels lie.

In between the different energy levels, arrows depict the possible transitions. In thermal equilibrium (at room temperature), the electronic state is maximally mixed (see section 5.5 for more information about mixed quantum states) and the occupation probability of each energy level is $1/3$. When applying laserlight, the spin dependency of the indicated transitions allows to polarize the electronic spin to $m_S = 0$.

The absorption maximum of NV centers in the ground state lies in the green region (532 nm). By shining laser light of this wavelength on an NV center, it can be excited to the ^{3}E state. Then the center can relax back to the ground state in multiple ways. Either it can emit a red 637 nm photon, which brings the center back to ^{3}A$_2$ in a single step and conserves the electron spin, or the system can relax via a non-radiative pathway (infrared transition) known as the intersystem crossing (ISC), taking the center first through the singlet states ^{1}A$_1$ and ^{1}E which changes the electron spin to m_S = 0. The probability of undergoing either transition depends on the spin of the NV electron. Studies [27] [28] have shown that the $|\pm 1\rangle_e$ spin sublevel of ^{3}E has a probability of $\sim \frac{1}{3}$ to decay non-radiatively, in contrast to a probability of only a few percent for $|0\rangle_e$. As a result the non-radiative process occurs more for the $|\pm 1\rangle_e$ states than the $|0\rangle_e$ states. As radiative decay preserves the electron spin, the system ends up in the $|0\rangle_e$ sublevel of ^{3}A$_2$ regardless of the starting spin value, which results in a polarization of the center under continuous illumination by green laser light. At room temperature, the transitions from ^{1}E to ^{1}A$_1$ to ^{3}A$_2$ take $\sim$ 200 ns [29], so that in this time a polarization of $\sim$90$\%$ can be obtained.

5.4.2 Optical read-out of the NV spin state: ODMR

Because of the spin-dependent probability of relaxing via emission of a red photon, a measurement of the red light intensity in a photoluminescence (PL) spectrum can be used to determine the electronic spin state m_S and thereof derived values (e.g. energy differences and the external magnetic field). Because of the hyperfine coupling between the electronic and nuclear spin, the nuclear spin state can also be determined via electron-nuclear double resonance (ENDOR) techniques [30]. As the control of the nuclear spin is one of the goals of the thesis, this will be explained in detail later.

First, assume there is no magnetic field and no hyperfine coupling present. As seen in the previous section, the NV centers in state $|\pm 1\rangle_e$ are more inclined to follow the non-radiative ISC, so they emit less fluorescence than their $|0\rangle_e$ counterparts during their decay. The photolumines-

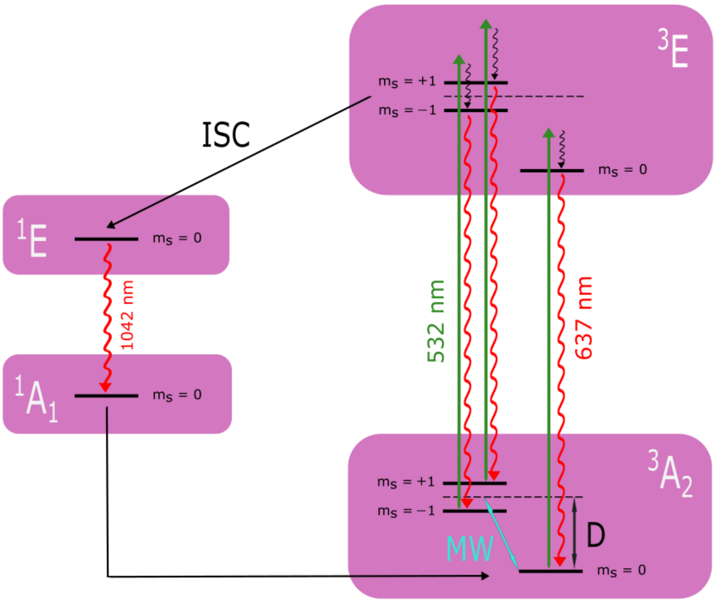

Figure 4: Simplified energetic structure of an NV center in an external magnetic field without hyperfine coupling. The purple blocks indicate many electron states and the black lines show possible variations in magnetic spin quantum number for these states. A blue arrow indicates the possibility of MW excitation, whereas green arrows show excitations for which green (532 nm) laser light is used. Black wiggly lines show internal conversion and red wiggly lines relaxation via emission of red (637 nm) or infrared (1042 nm) light. Straight black lines give a dark transition called the intersystem crossing.

cence (PL) of the NV center is thus substantially higher when the $|0\rangle_e$ state is populated and this enables the detection of electron spin resonance (ESR) of the defect. In this specific case, the experimental readout method is known as the optical detection of magnetic resonance (ODMR) [21] and relies on the simultaneous application of laser light and a microwave field which is swept in the region of the resonance frequency of the transition $|0\rangle_e \leftrightarrow |\pm1\rangle_e$. If the NV center is initially polarized in the $|0\rangle_e$ state, the photoluminescence drops when the exact resonance condition is reached, because of an increase in non-radiative decay. The resonance frequency reflects the ZFS and is approximately 2.87 GHz at room temperature.

When a magnetic field is applied to the NV center, the $|\pm1\rangle_e$ state splits into the $|1\rangle_e$ and $|-1\rangle_e$ states due to the Zeeman effect. This creates two possible resonance conditions $\nu_\pm$ given by formula (4). This also allows to calculate the ambient magnetic field in the direction of the NV center axis B_{NV} from the distance between the resonances.

$$\nu_{\pm} = D \pm g\mu_B B_{NV} \quad (4)$$

The previously mentioned ODMR technique is also known as CW-ODMR because of the continuous illumination of the NV centers with green laser light, continuous sweeping of the frequency of the MW field and continuous measurement of the PL intensity. CW-ODMR has a limited frequency resolution of several MHz due to power broadening of the laser and MW pulses, but the fast scan speed makes it useful in extracting the resonant frequency of an NV electron spin [5]. For more advanced applications, pulsed protocols can be used to probe and manipulate the state of an NV center. The pulsed schemes allow to achieve a projection-noise limited sensitivity as the tools for manipulating and measuring the spins (laser light, MW field, RF field, ...) do not interfere with the free precession of the electrons [31].

5.5 Qubit representation of the NV center spins

Although the aim of this thesis is to investigate the use of NV centers in the field of quantum thermodynamics, it is useful to look first at quantum information theory [32]. This is because throughout this work, the NV center is often regarded as a two level system, which is what a qubit is by definition. Qubits are the quantum equivalent of bits (binary digits), the classical information unit. The logical value of a bit can either be 0 or 1, nothing else and nothing in between. Because different laws govern quantum systems, qubits (quantum bits) can assume the logical values 0 and 1, but also any linear combination of these two states. In experiments, qubits can be physically represented by any quantum object with two well defined distinct eigenstates, e.g. two orthogonal photon polarization states (such as horizontal-vertical).

Mathematically, the eigenstates of a qubit are represented by $|0\rangle$ and $|1\rangle$. In our NV center system, we could look at either the electron spin qubit with logical state vectors $|0\rangle_e$ and $|1\rangle_e$ or the ^{14}N nuclear spin qubit with logical state vectors $|0\rangle_N$ and $|1\rangle_N$. It is very important to note that these logical states do not necessarily correspond to the "real" $|m_S\rangle_e$ and $|m_I\rangle_N$ eigenstates. It is possible that the real spin eigenvalue associated with logical state $|1\rangle_e$ is indeed $m_S = 1$, but depending on which two levels are chosen to create the approximate two-level system, this could also be $m_S = -1$ or $m_S = 0$ or any pair of orthogonal linear combinations of these eigenvectors.

Using the computational basis set $\{|0\rangle, |1\rangle\}$, all possible states $|\psi\rangle$ of the qubit can be written as [32]:

$$\begin{aligned} |\psi\rangle &= a|0\rangle + b|1\rangle & \text{(5a)} \\ &= \cos\left(\tfrac{\theta}{2}\right)|0\rangle + e^{i\phi}\sin\left(\tfrac{\theta}{2}\right)|1\rangle & \text{(5b)} \end{aligned}$$

Here, a and b are two complex numbers related to each other by the normalization condition $|a|^2+|b|^2 = 1$, such that the state can also be parametrized by angles $\theta \in [0, \pi]$ and $\phi \in [0, 2\pi[$ for which holds that $a = cos(\frac{\theta}{2})$ and $b = e^{i\phi} sin(\frac{\theta}{2})$. This allows for a geometric visualization of the qubit state as a point on the surface of a unit radius sphere (which is called the Bloch sphere) as can be seen in figure 5. Another useful representation of a qubit is the density operator (also called density matrix) ρ [32], which is defined in formula 6. This is because in quantum information science one frequently deals with situations in which the state vector of the system is unknown, but one does know that a set of possible states $\{|\psi_i\rangle\}$ can occur with a probability $\{p_i\}$ ($p_i > 0$ and $\sum_i p_i = 0$).

$$\rho = \sum_i p_i |\psi_i\rangle\langle\psi_i| \quad (6)$$

The density operator has a few interesting properties. First of all, it is a positive operator, which means that its eigenvalues are real and non-negative. Secondly, due to the conservation of probabilities, the trace of ρ is always equal to 1. Lastly, if the trace of ρ^2 is also equal to 1, then the corresponding quantum state is a pure state. The concepts of pure and mixed states are important in quantum mechanics, as they follow from a classical probability theory (deterministic and random states) [33]. To understand these concepts better, it is interesting to look at the singular value decomposition of a density operator $\rho = \sum_i \lambda_i |\psi_i\rangle\langle\psi_i|$. As ρ is positive, this means that $\lambda_i \geq 0$. Furthermore because of the trace condition, the sum of all λ_i must be equal to 1. This means that the eigenvalue vector $\lambda = (\lambda_1, ..., \lambda_n)$ of ρ can be interpreted as a probability distribution. This distribution can vary between two extreme cases:

1. If $\lambda = (1, 0, 0, ..., 0)$ ρ corresponds to a pure state $|\psi\rangle$ and can be written as $|\psi\rangle\langle\psi|$.
2. If $\lambda = (1/n, 1/n, 1/n, ..., 1/n)$ ρ corresponds to a maximally mixed state and can be written as I/n, where I is the identity matrix.

On the Bloch sphere, pure states lie on the surface, whereas mixed states lie inside the sphere (along the vertical line between the two basis states of which the system state is a mixture). For example, suppose a state $|\psi\rangle$ is equal to $|0\rangle$ with a probability p and equal to $|1\rangle$ with a probability $1 - p$, then the density matrix ρ of $|\psi\rangle$ is given by [33]:

$$\rho = \begin{pmatrix} p & 0 \\ 0 & 1-p \end{pmatrix} \quad (7)$$

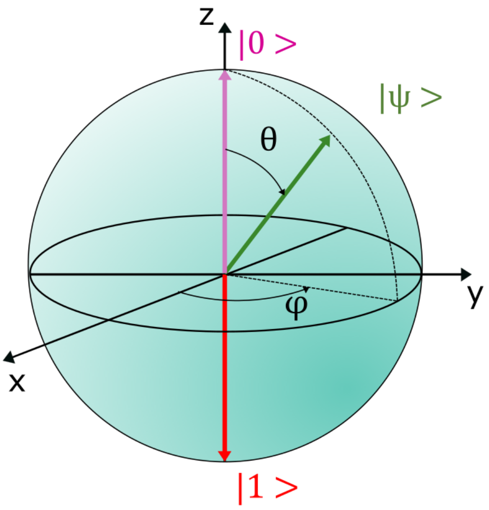

Figure 5: The Bloch sphere representation of a qubit state vector $|\psi\rangle$ determined by the angles θ and ϕ. The intersections of the sphere with the z-axis (at $z = 1$ and $z = -1$) give the end points of the two basis vectors $|0\rangle$ and $|1\rangle$. The x- and z-axis are in real units and the y-axis in imaginary units.

The density operator of a qubit in a generic pure state $|\psi\rangle$ (as in formula 5) can be determined as follows:

$$\begin{aligned} \rho &= |\psi\rangle\langle\psi| \\ &= \begin{pmatrix} \cos\left(\frac{\theta}{2}\right) \\ e^{i\phi}\sin\left(\frac{\theta}{2}\right) \end{pmatrix} \begin{pmatrix} \cos\left(\frac{\theta}{2}\right) & e^{-i\phi}\sin\left(\frac{\theta}{2}\right) \end{pmatrix} \\ &= \frac{1}{2}\begin{pmatrix} 1+\cos(\theta) & e^{-i\phi}\sin(\theta) \\ e^{i\phi}\sin(\theta) & 1-\cos(\theta) \end{pmatrix} \quad (8) \end{aligned}$$

Using the Euler relation and the Pauli matrices (see formula 9), this can be written as $\rho = \frac{1}{2}(I + \vec{r}_\rho \cdot \vec{\sigma})$. Here, I is the identity matrix, $\vec{\sigma}$ is the three-element vector of Pauli matrices (X, Y, Z) and $\vec{r}_\rho$ is the unit Bloch vector $(\cos(\phi)\sin(\theta), \sin(\phi)\sin(\theta), \cos(\theta))$.

$$X = \begin{pmatrix} 0 & 1 \\ 1 & 0 \end{pmatrix} \;,\; Y = \begin{pmatrix} 0 & -i \\ i & 0 \end{pmatrix} \;,\; Z = \begin{pmatrix} 1 & 0 \\ 0 & -1 \end{pmatrix} \quad (9)$$

As stated in section 5.3, the NV set-up used in this thesis contains both an electron and nuclear spin qubit. The density operator of the total system in a generic state $|\psi\rangle_e \otimes |\psi\rangle_N$ can then be written as:

$$\begin{aligned}\rho_{tot} &= (|\psi\rangle_e \otimes |\psi\rangle_N)({}_e\langle\psi| \otimes_N \langle\psi|) \\ &= \rho_e \otimes \rho_N \qquad (10)\end{aligned}$$

Here, state $|\psi\rangle_e$ is equal to $\cos{(\frac{\theta_e}{2})}|0\rangle_e + e^{i\phi_e}\sin{(\frac{\theta_e}{2})}|1\rangle_e$ as in formula 5 and an analogous expression holds for $|\psi\rangle_N$. The second equality follows from a property of the tensor product [34]. The other way around ρ_e and ρ_N can also be found from the total density matrix by taking the partial trace with respect to the other qubit.

$$\begin{aligned}\rho_e &= Tr_N[\rho_{tot}] &= \textstyle\sum_{i=0}^{1}(I_e \otimes_N \langle i|)\rho_{tot}(I_e \otimes |i\rangle_N) \quad (11a) \\ \rho_N &= Tr_e[\rho_{tot}] &= \textstyle\sum_{i=0}^{1}({}_e\langle i| \otimes I_N)\rho_{tot}(|i\rangle_e \otimes I_e) \quad (11b)\end{aligned}$$

5.6 Quantum state tomography of the NV center

Quantum state tomography (QST) is used to address measurement procedures that allow to determine the matrix elements of the density operator of a system. This is essential in quantum thermodynamics and quantum information science, because it allows to check intermediary or final qubit states and to follow quantum processes. Various methods can be used to do this. For example it is possible to determine either the electronic or the nuclear spin state of an NV center using three Rabi measurements, where one is used as a reference measurement, and the other two to determine θ and ϕ. This method relies on the amplitudes of the Rabi measurements and will thus be referred to as the amplitude QST or AQST. The experimental method and formulas used to determine the density operator are based on previous work at Hasselt University [35]. At this time the proposed scheme was used to determine the NV electron state. In this thesis, I have designed a similar QST protocol to determine the ^{14}N nuclear spin state, and have extended on the method of calculating the density matrix using the Rabi amplitudes. Furthermore, I have demonstrated that it is also possible to perform a quantum state tomography using only two Rabi measurements. This method relies on the phases of the Rabi oscillations and is therefore called phase QST or PQST. This method can also be used to determine the electronic spin state.

5.6.1 Amplitude quantum state tomography

AQST can be explained more visually with the aid of the Bloch sphere, so this method will be addressed first. As stated in the previous section, any qubit state can be represented by a point on the Bloch sphere (which indicates the end point of the corresponding state vector). Determining the coordinates (x, y, z) of this point is thus equivalent to determining the quantum state. One relation is already obtained from the unit radius of the Bloch sphere, namely $x^2 + y^2 + z^2$=

1. Then one additional equation is necessary to determine the values of θ_N and ϕ_N. However, it is useful to perform two more measurements in order to check for internal consistency.

In the presented AQST protocol, a reference Rabi measurement starts off the measurement sequence. Here, the amplitude A_R of the Rabi oscillations between $|0\rangle$ and $|1\rangle$ is determined. Theoretically, this is the largest amplitude that can occur in any Rabi measurement and is used to normalize the next two measurements. The phase of the RF field in this experiment is not important as all phases would give the same maximum amplitude. Therefore the same reference nuclear Rabi measurement (e.g. fig. 19) can be used for all tomography measurements. However, due to the possibility of experimental conditions changing over time it's better to conduct all three Rabi measurements adjacently and measure a new reference Rabi each time.

After the reference measurement, the nuclear spin is brought from $|0\rangle$ to $|\psi\rangle_N$, which is the state to be measured. It is important to prepare the system to a known state, so that the QST results can be compared with this. Once the method proves to be viable, this state preparation stage can be replaced by any quantum protocol manipulating the nuclear spin to a known or unknown state. For now, the state preparation consists out of an initialization to $|0\rangle_N$, after which a transition specific RF pulse is used to tilt the nuclear spin vector over a certain angle θ_N towards $|1\rangle_N$. The next step of the state preparation happens in overlap with the following Rabi measurements. In these measurements, RF magnetic field pulses of a certain duration τ are applied to induce rotations of this nuclear spin state around the x- or y-axes. By applying RF waves with a certain phase and choosing the zero-point of this phase angle ϕ_N to be the positive x-axis, one can effectively rotate $|\psi\rangle$ to the azimuthal angle $-\phi_N$. Together, these two controls generate a uniquely determined nuclear state.

The x-component of the qubit state vector is determined using a second Rabi experiment, where $|\psi\rangle_N$ rotates around the x-axis. If the amplitude of the oscillations is equal to A_x, then this means that the Bloch vector is tracing a circle around the x-axis with radius A_x/A_R. The third Rabi measurement, used to find the y-coordinate, is analogous: one brings the system to $|\psi\rangle_N$ again and then measures Rabi oscillations around the y-axis. Then in the same way, if the amplitude is A_y, then the Bloch vector is tracing a circle around the y-axis with radius A_y/A_R. This concept is depicted schematically in figure 6.
Using the formulas for a sphere and a circle (technically a cylinder) in Cartesian coordinates,

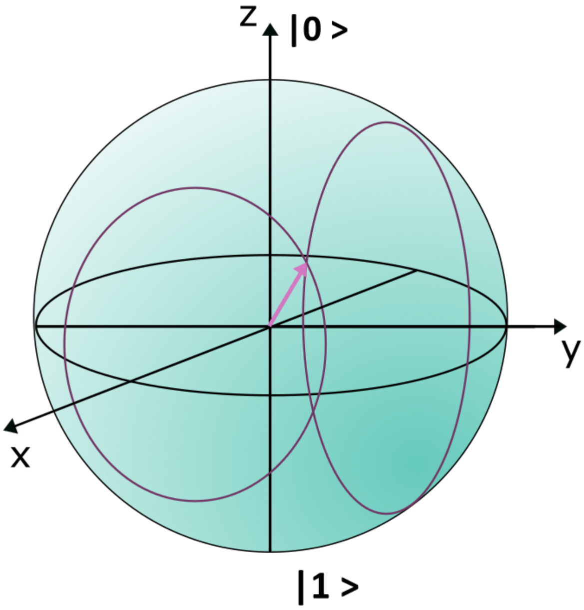

Figure 6: Schematic representation of the state vector $|\psi\rangle$ (purple arrow) on the Bloch sphere. During the two Rabi measurements, this vector traces the two purple circles on the sphere around the x- and y-axis.

one can write three equations for x, y and z:

$$\begin{aligned} x^2 + y^2 + z^2 &= 1 && \text{(12a)} \\ y^2 + z^2 &= (\tfrac{A_x}{A_R})^2 && \text{(12b)} \\ x^2 + z^2 &= (\tfrac{A_y}{A_R})^2 && \text{(12c)} \end{aligned}$$

This set of equations can be solved for x, y and z as follows:

$$\begin{aligned} x^2 &= 1 - (\tfrac{A_x}{A_R})^2 && \text{(13a)} \\ y^2 &= 1 - (\tfrac{A_y}{A_R})^2 && \text{(13b)} \\ z^2 &= \tfrac{A_x^2 + A_y^2}{A_R^2} - 1 && \text{(13c)} \end{aligned}$$

Equation 13 does not yet uniquely specify (x, y, z) as there is a sign ambiguity. In order to determine the signs of x, y and z, one has to look at the shape of the Rabi oscillations. For this, one has to keep in mind that in the employed Rabi protocols, the measured PL signal is inversely proportional to the probability of being in $|0\rangle_N$. This is the case because the fluorescence signal will be measured using pulsed ODMR with a π-pulse whose frequency corresponds to the $|0, 0\rangle \leftrightarrow |-1, 0\rangle$ transition. Thus, when the probability of being in $|0\rangle_N$ rises, the PL intensity drops (the resonance peak gets deeper). This means that if a Rabi signal starts off in a downward trend, then the Bloch vector is brought closer to $|0\rangle_N$. For the x-Rabi this means that y is positive, since the rotation is positive. Analogously, an x-Rabi starting in an upward trend signifies a negative y, a y-Rabi starting in a downward trend signifies a negative x and a y-Rabi starting in an upward trend signifies a positive x. The z-coordinate can be found by looking at whether the x- and y-Rabi start above our below their mean value. If the Rabi oscillations start off with an above average PL signal, then this means that z is negative, otherwise z is positive.

When x, y, and z are uniquely determined, θ_N and ϕ_N can be calculated using formula (14). This way, $|\psi\rangle_N$ can be determined easily using formula (5).

$$\theta_N = \tan^{-1}(\frac{\sqrt{x^2+y^2}}{z}) \quad (14a)$$

$$\phi_N = \tan^{-1}(\frac{y}{x}) \quad (14b)$$

By definition, $\tan^{-1}(a)$ returns a value $\alpha \in]\frac{-\pi}{2}, \frac{\pi}{2}[$. However, also by definition $\theta_N \in [0, \pi]$ and $\phi_N \in [0, 2\pi[$. Since $tan(\alpha + \pi) = tan(\pi)$, an angle π should be added to θ_N if it is smaller than zero. For a negative ϕ_N, one has to look at the sign of x. If x is negative, then an angle π should be added to ϕ_N. If x is positive, then an angle 2π should be added to ϕ_N.

5.6.2 Phase quantum state tomography

In performing AQST, three measurements are necessary to determine the coordinates (x, y, z) of the quantum state. Since the endpoint of this state vector is confined to the Bloch sphere (normalization condition), these coordinates are not independent of each other and in fact two variables (θ_N, ϕ_N) are sufficient to fully describe the quantum system. This implies that two measurements should also suffice to determine these angles and sparked the idea for PQST, where the phases α and β of respectively the x- and y-Rabi measurement can be linked to the angles θ_N and ϕ_N describing quantum state $|\psi\rangle_N$.

The simplest approach is to first find α and β as a function of θ_N and ϕ_N. As can be seen on figure 7, geometrical arguments can be used. Since the the Rabi oscillations of the reference measurement define the x-axis as rotation axis (more information can be found in section 7.2), this offsets ϕ_N automatically by 270 degrees. Therefore, the formulas will be derived first for a situation where $|\psi\rangle_N$ lies in the octant of the Bloch sphere with $\theta_N \in [0°, 90°]$ and $\phi_N \in [180°, 270°]$. To simplify calculations, ϕ_N will be measured from the negative y-axis for now and then later corrected with the 270 degree offset. The angle ϕ'_N will be used to denote the phase angle measured from the negative y-axis so that $\phi_N = 270 - \phi'_N$.

The top left of figure 7 shows the 3D Bloch sphere representation of state $|\psi\rangle_N$ and the angles θ_N and ϕ_N. Then there are three projections of the Bloch sphere in different directions: a top view along the z-axis and two side views along the x- and y-axis. The last two also show the rotations of $|\psi\rangle_N$ around the corresponding axes in Rabi measurements with a light purple circle.

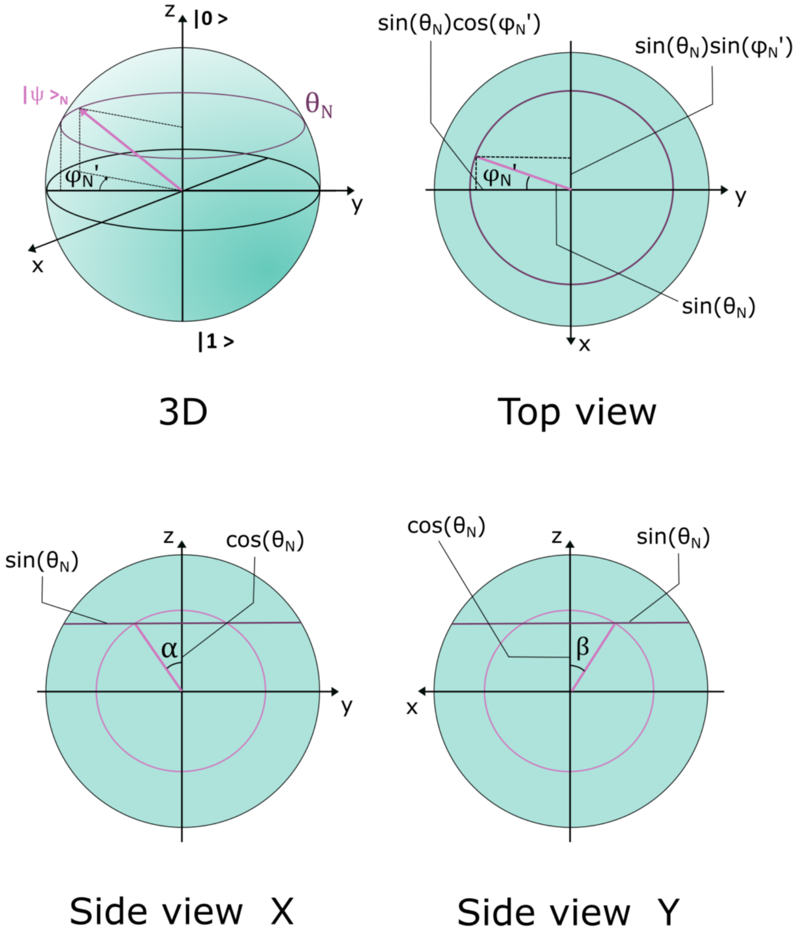

Figure 7: Determination of the phase angles $\alpha(\theta_N, \phi_N)$ and $\beta(\theta_N, \phi_N)$ of the x- and y-Rabi for $\theta \in [0°, 90°]$ and $\phi \in [180°, 270°]$. The dark purple circle is located at θ and the light purple circle is the circle over which $|\psi\rangle$ moves in an x-Rabi measurement (side view X) or y-Rabi measurement (side view Y).

From this figure, the phase angle α of the x-Rabi can be calculated as follows:

$$\alpha \quad = \quad \tan^{-1}[\tfrac{sin(\theta)cos(\phi')}{cos(\theta)}] \quad (15)$$

On figure 7 it can be seen that α and β have opposite signs. In the calculations here, these signs are not taken into account and corrections are made for that when necessary. I chose this approach so that the formulas used are the same for every octant and the signs of the angles can be determined at the end. However, one should know that the Rabi phase angles α and β are both restricted to the domain $[-180°, 180°]$ and that their sign varies from octant to octant. Keeping this in mind, phase angle β of the y-Rabi can be determined in a similar manner:

$$\beta \quad = \quad \tan^{-1}[\tfrac{sin(\theta)sin(\phi')}{cos(\theta)}] \quad (16)$$

Now that $\alpha(\theta_N, \phi'_N)$ and $\beta(\theta_N, \phi'_N)$ are known, the inverse relations can be determined. To find $\phi'_N(\alpha, \beta)$ isolate $cos(\theta_N)$ in both formulas and equate them. This gives:

$$\phi'_N \quad = \quad \tan^{-1}[\tfrac{\tan(\beta)}{\tan(\alpha)}] \quad (17)$$

This formula for ϕ'_N can be substituted in either one of the starting equations, giving $\theta_N(\alpha, \beta)$:

$$\begin{aligned} \theta_N \quad &= \quad \tan^{-1}[\tfrac{\tan(\alpha)}{\cos\left(\phi'_N\right)}] \quad (18a) \\ &= \quad \tan^{-1}[\tfrac{\tan(\beta)}{\sin\left(\phi'_N\right)}] \quad (18b) \end{aligned}$$

Note that only now ϕ'_N can be adjusted for the offset of 270 degrees and the elements of the density operator can be determined using $\phi_N = 270° - \phi'_N$ and θ_N.

PQST calculations in other octants of the Bloch sphere

The formulas (15) to (18) are created in such a way that they are valid in each one of the eight octants of the Bloch sphere, without altering any signs. However, in order to do so, one must adapt the meaning of θ_N and ϕ_N according to which octant $|\psi\rangle_N$ lies in. For example, when θ_N is larger than 90°, this would mean that $cos(\theta_N)$ becomes negative. However, the above calculations are based on geometrical arguments and the length of a line is never negative, nor can an angle of a right-angled triangle be greater than 90 degrees. Therefore, when θ_N is larger than 90 degrees, one should instead use $\theta'_N = 180° - \theta_N$ in the calculations. For ϕ_N, there are more options, as it can be either in $[0°, 90°]$, $[90°, 180°]$, $[180°, 270°]$ or $[270°, 360°]$. The third case was already discussed before and it involved redefining the zero-axis of ϕ_N to the negative y-axis at 270° and then correcting for this later. Once again, this was done since the calculations were all based on geometrical arguments in right-angled triangles, so no angle can be larger than 90 degrees. If ϕ_N lies in another octant, one can use the same trick.

To find α and β as a function of the known angles θ_N and ϕ_N, for example when constructing the ideal Rabi oscillations for a known state, the following step-by-step plan can be used.

1. When $\theta_N \in [0°, 90°]$ take $\theta'_N = \theta_N$. When $\theta_N \in [90°, 180°]$ take $\theta'_N = 180° - \theta_N$.
2. When $\phi_N \in [0°, 90°]$, take $\phi'_N = 90° - \phi_N$. When $\phi_N \in [90°, 180°]$ take $\phi'_N = 180° - \phi_N$. When $\phi_N \in [180°, 270°]$ take $\phi'_N = 270° - \phi_N$. When $\phi_N \in [270°, 360°]$ take $\phi'_N = 360° - \phi_N$.
3. Solve formulas (15) and (16) using θ'_N and ϕ'_N instead of θ_N and ϕ_N and α' and β' instead of α and β.
4. If θ_N is smaller than 90 degrees, $\alpha = \alpha'$ and $\beta = \beta'$. If θ_N is larger than 90 degrees, α = 180° - α' and β = 180° - β'.
5. The sign of α and β is determined by the range of ϕ_N.

$\phi_N \in$	α	β
$[0°, 90°]$	-	+
$[90°, 180°]$	-	-
$[180°, 270°]$	+	-
$[270°, 360°]$	+	+

The use of the above plan will now be illustrated using a state $|\psi\rangle_N$ with $\theta_N \in [90°, 180°]$ and $\phi_N \in [0°, 90°]$, as can be seen on figure 8. Starting with the first step, θ_N should be replaced in the calculations by $\theta'_N = 180° - \theta_N$. Next, ϕ_N lies between 0 and 90 degrees, so that $\phi'_N = 90° - \phi_N$ should be used in the calculations. Looking at figure 8, one can see that using these choices of θ'_N and ϕ'_N guarantee that the formulas (15) and (16) are still valid to find α' and β'. Then, as θ is larger than 90 degrees, α is equal to $180° - \alpha'$ and β is equal to $180° - \beta'$. Lastly, $\alpha < 0$ and $\beta > 0$ because $\phi_N \in [0°, 90°]$.

When starting from an unknown state $|\psi\rangle_N$, one can determine θ_N and ϕ_N from the phases α and β of the x- and y-Rabi measurement using the following step-by-step plan

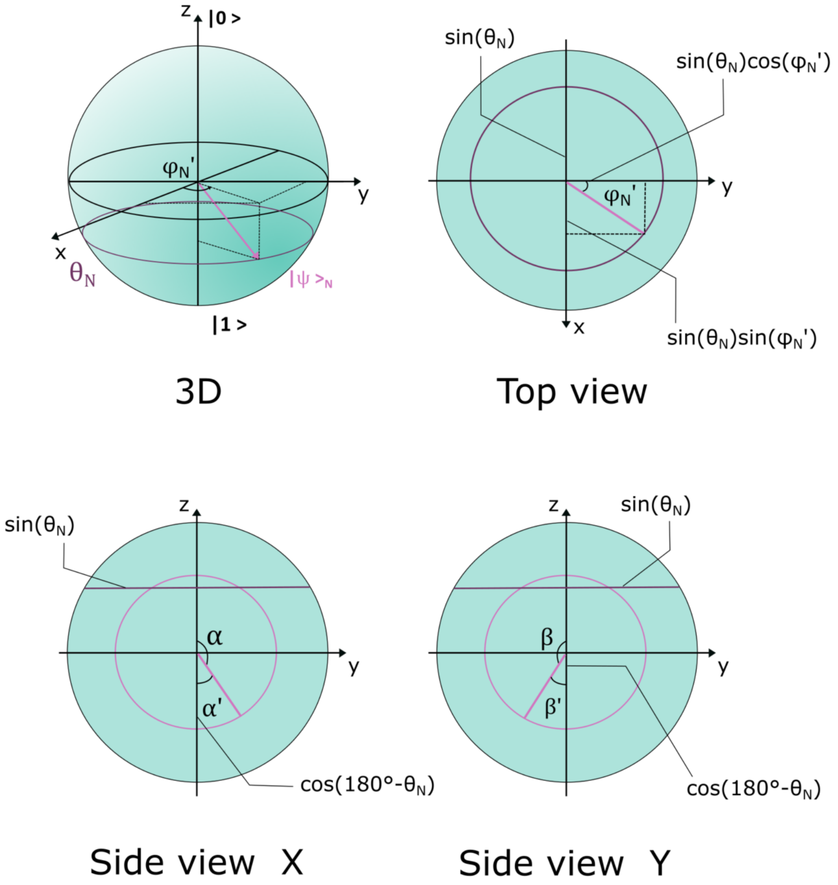

Figure 8: Determination of the phase angles $\alpha(\theta_N, \phi_N)$ and $\beta(\theta_N, \phi_N)$ of the x- and y-Rabi for $\theta_N \in [90°, 180°]$ and $\phi_N \in [0°, 90°]$. The dark purple circle is located at θ_N and the light purple circle is the circle over which $|\psi\rangle_N$ moves in an x-Rabi measurement (side view X) or y-Rabi measurement (side view Y).

1. Determine α and β by fitting the x- and y-Rabi oscillations. The values of both angles need to lie between $-180°$ and $180°$. If not, add or subtract $360°$. When α and β are in the range of -90 to 90 degrees, use $\alpha' = |\alpha|$ and $\beta' = |\beta|$, otherwise use $\alpha' = 180° - |\alpha|$ and $\beta' = 180° - |\beta|$.
2. Calculate θ'_N and ϕ'_N from formulas (17) and (18).
3. Inspect the signs of α and β to determine the offset of ϕ'_N, so that ϕ_N is equal to this offset plus or minus $|\phi'_N|$. The results in the table below can be verified with figure 9.

α	β	ϕ_N
-	+	$90° - \lvert\phi'_N\rvert$
-	-	$90° + \lvert\phi'_N\rvert$
+	-	$270° - \lvert\phi'_N\rvert$
+	+	$270° + \lvert\phi'_N\rvert$

4. Inspect whether the x- and y-Rabi oscillations start above or below their mean value. If they start below their mean value, this means that $\theta_N < 90°$ and $\theta_N = \theta'_N$. If they start above, this means that $\theta_N > 90°$ and $\theta_N = 180° - |\theta'_N|$.

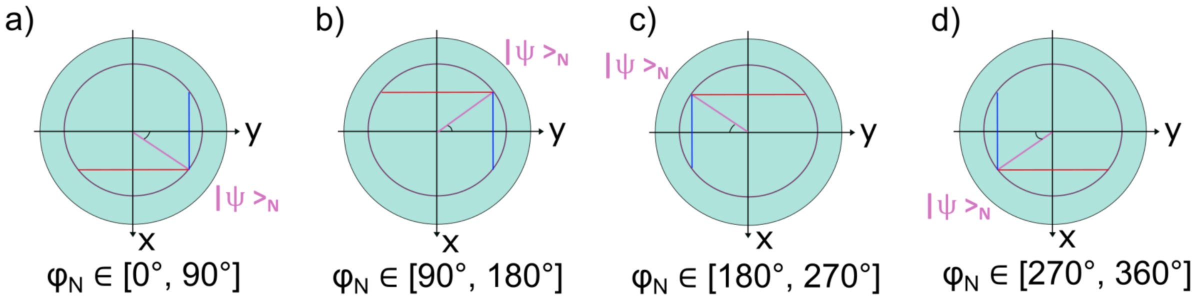

Figure 9: Determination of the relation between ϕ_N and the signs of α and β, the phase angles of the x- and y-Rabi measurements. The top view of the Bloch sphere is shown for each possible quadrant in which ϕ_N can lay. Projections of the Rabi rotations around the x- and y-axis are shown as respectively red and blue lines. When keeping in mind the positive direction of rotation, this allows to determine the sign of α and β. a) $\phi_N \in [0°, 90°]$ has $\alpha < 0$ and $\beta > 0$. b) $\phi_N \in [90°, 180°]$ has $\alpha < 0$ and $\beta < 0$. c) $\phi_N \in [180°, 270°]$ has $\alpha > 0$ and $\beta < 0$. d) $\phi_N \in [270°, 360°]$ has $\alpha > 0$ and $\beta > 0$.

Experimentally, both AQST and PQST have their advantages and drawbacks. For example, because AQST uses a reference measurement, the obtained coordinates can be verified using this redundant information. On the other hand, the amplitude of the Rabi oscillations is very susceptible to sample drifts that occur when applying RF magnetic fields (see section 7.1.3). If the NV center drifts out of focus during one of the three Rabi measurements, this means that the amplitude of that particular measurement will be lower than it should be. This is particularly true for states along one of the axes, where x- and y-Rabi oscillations should have either the same amplitude as the reference Rabi or amplitude zero. Due to small measurement errors or sample drift it can occur that the reference Rabi amplitude is actually smaller than the x- or

y-Rabi, which results in complex coordinates. Methods exist to correct for this mathematical inconvenience, but can make the calculations cumbersome. The phase of the Rabi measurements is less affected by this sample drift and is therefore more useful when it's difficult to keep the NV center in focus.

5.6.3 Fidelity of QST measurements

As stated, the goal of QST is to recover the elements of the density operator of a known quantum state and to determine the elements of the density operator of an unknown quantum state. To quantify the reliability of QST, the fidelity F [36] of the experimentally determined density operator (of a known quantum system) can be calculated using formula (19). The fidelity expresses how much two quantum states are alike as a number from zero (orthogonal states) to one (identical states). In this formula, ρ_e is the experimentally determined density operator and ρ_t is the theoretically calculated density operator of the prepared quantum state.

$$F = \frac{T(\rho_t \rho_e)}{\sqrt{Tr(\rho_t^2)Tr(\rho_e^2)}} \qquad (19)$$

Another way of visualizing the similarity between the created and measured state is to plot the expected Rabi oscillations for the created state over the experimental data. For this, the Rabi signal of this ideal (created) state can be simulated using the formula $c_x + A^2 sin^2(\frac{\omega t+\alpha}{2})$ for the x-Rabi and $c_y + B^2 sin^2(\frac{\omega t+\beta}{2})$ for the y-Rabi. If necessary, c_x, c_y can be fitted using the experimental data to create a nice visualization. In AQST, the amplitudes A_x and A_y can calculated using a reference Rabi measurement (giving A_R) and theoretically calculated x^2 and y^2 values. In PQST the phases can be determined from θ_N and ϕ_N and geometrical arguments, as already showed in equations (15) and (16) (but paying attention to the definition of the angles and the offset). The frequency can be determined using T_π in both cases. Apart from A_R and T_π no experimental values must be used. By plotting the resulting x- and y-Rabi oscillations on top of the experimental fits, the correspondence of the created and measured states can be visualized. The more closely the two Rabi sequences overlap, the better the two states correspond and the higher the fidelity of the QST measurement.

5.7 The NV center as quantum Otto engine

5.7.1 Quantum engines

An engine [1] is an omnipresent thermodynamic device that is used to convert one form of energy into another, in particular heat to work for a heat engine. Part of the heat from a hot bath is hereby ejected to a cold bath, which limits the efficiency of power generation and is the essence of the second law of thermodynamics. Classic heat engines are well known -think about the steam engine that fueled the industrial revolution for example- but so are some of their quantum counterparts. The primary quantum heat engine is the laser, because of the equivalence of the three-level laser with the Carnot engine.

The difference of classical and quantum heat engines lies mostly in the renewed interpretation of classical concepts in the quantum world. Therefore, to determine what is a quantum heat engine, it is instructive to determine first what a classical heat engine exactly is. The classical Otto cycle will be used as an example, because it can be realized in practice quite easily, as opposed to the ideal Carnot cycle. The classical Otto cycle [37] consists out of a sequence of isentropic (adiabatic) and isochoric strokes and is visualized in figure 10. Here, the cycle starts with a working substance at a low temperature T_l. The first stroke ($1 \rightarrow 2$) adiabatically compresses the substance and an amount of work W_{in} is done on the system. Then in the second stroke ($2 \rightarrow 3$), the working substance is brought into contact with a thermal reservoir at temperature $T_h > T_l$ and heated at constant volume. Then in the third stroke ($3 \rightarrow 4$), also called the power stroke, the working substance is expanded adiabatically, delivering work W_{out} to its environment. Lastly, the system is brought into contact with a thermal reservoir at temperature T_l, cooling the working substance at constant volume and reaching back the initial state.
From this figure it can be concluded that the working substance in the classical Otto cycle is characterized by two properties:

1. It can heat up/ cool down.
2. It can perform work/ work can be performed on it (the internal energy U can change).

Any working substance -be it a gas, a liquid, or something else- that has these two properties can be used as Otto engine. Therefore, a quantum working substance with these two properties can be used as a quantum Otto engine. It will be seen that spins (electronic or nuclear) can be used as possible quantum working media. So when looking at what the concepts work/ heat and

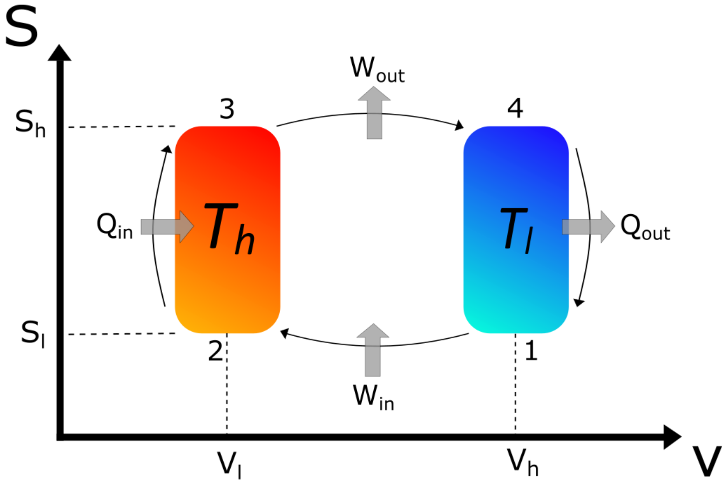

Figure 10: Classical Otto cycle. The vertical axis represents the entropy of the working substance, which is varied between a low value S_l and a high value S_h. The horizontal axis represents the volume of the working substance, which is also varied from a low value V_l to a high value V_h. Stroke 1 → 2 and stroke 3 → 4 are isentropic (adiabatic) and stroke 2 → 3 and 4 → 1 are isochoric.The entire cycle is reversible and the working substance is always in thermodynamic equilibrium.

energy/ volume/ temperature mean in quantum mechanics, this system will sometimes be used.

The interpretation of internal energy in quantum mechanics is not surprising. To find the internal energy of a quantum system, one first needs to find the spectrum of energy eigenvalues, which can be determined by solving the Schrödinger equation. Then the particular energy eigenstate (internal energy) of system with density operator ρ and Hamiltonian $\hat{H}(t)$ can be found in the following way [38]:

$$E(t) = tr[\rho(t)\hat{H}(t)] \quad (20)$$

The first law of thermodynamics links a change in internal energy to both work and heat and the same thing can be done in quantum thermodynamics.

$$\begin{aligned} dE &= \delta Q + \delta W && \text{(21a)} \\ &= tr[\hat{H}(t)\mathbf{d}_t\rho(t)]dt + tr[\rho(t)\mathbf{d}_t\hat{H}(t)]dt && \text{(21b)} \end{aligned}$$

This can be integrated over a time τ to determine the energy change of a quantum system during a certain process, as is illustrated by the following formulas.

$$
\begin{aligned}
\Delta E &= \int_0^\tau \delta Q + \int_0^\tau \delta W && \text{(22a)}\\
&= \langle Q\rangle + \langle W\rangle && \text{(22b)}\\
&= tr[\rho(\tau)\hat{H}(\tau)] - tr[\rho(0)\hat{H}(0)] && \text{(22c)}
\end{aligned}
$$

These formulas confirm that (just as in classical thermodynamics) the change in internal energy only depends on the end points of the process, whereas heat and work are path-dependent. Note that in quantum thermodynamics, the minimal requirements are the existence of a meaningful Hamiltonian and meaningful states at the beginning and end of the process. They do not necessarily need to be available, nor meaningful during the time-resolved evolution [38]. Furthermore, the formulas show that in a unitary evolution, heat relates to the Liouville-von Neumann equation $\mathbf{d}_t\rho(t) = -\frac{i}{\hbar}[\hat{H}(t), \rho(t)]$ and work to a change in the time-dependent Hamiltonian $\mathbf{d}_t\hat{H}(t)$.

Now that the quantum interpretations of internal energy, work and heat are clear, the concepts of volume and temperature can be investigated, as well as the working substance itself. Focusing on quantum working substances based on spins, the concept of spin temperature [39] will be explained. Spins inside a solid state material interact with the lattice through spin-lattice relaxation, resulting in the lattice acting as a sort of thermostat for the spins. At thermal equilibrium, the lattice temperature can also be assigned to the present spins, meaning that the properties of the system can be predicted by Boltzmann's law $p_i \sim e^{-E_i/k_B T}$. Here, p_i is the population of a certain spin energy level E_i and T is the lattice temperature. Using the density operator formalism, such a Boltzmann thermal state can also be written as $\rho \sim= e^{-\hat{H}/k_B T}$. This description is valid when the driving field of the spins is relatively weak and varies relatively slowly. For stronger, quickly fluctuating (pulsed) driving fields, the concept of spin temperature distinct from the lattice temperature can be introduced. In this case, for a spin $1/2$ system, the spin temperature T is introduced through the relation $p_+/p_- = e^{-\hat{H}/k_B T}$, where p_+ and p_- are the populations of the two possible spin states. When $p_+ = p_-$ the spin temperature grows to infinity, whereas a π-pulse (flipping the spin populations) can create negative temperatures. It needs to be remarked that the concept of spin temperature will be used loosely here, since steady-states do not always correspond to thermal equilibrium states. This is the case when they result from an optical pumping process and not from coupling to a thermal reservoir. One can see that the state resulting from optical pumping is no thermal state because it generates approximately equal populations for $|0,-1\rangle$, $|0,0\rangle$ and $|0,1\rangle$ even though their energies are split by the ambient magnetic field [2].

So for quantum working substances, heat is linked to polarization through the concept of spin temperature. Therefore to be able to heat up or cool down a working substance, it needs to have a certain amount of energy levels that can be occupied with certain probabilities. The other required property is to be able to have a change in internal energy. In quantum mechanics, this corresponds to a change in the energy levels due to a time-varying Hamiltonian. The time variance of this system Hamiltonian is often expressed using a control parameter λ. Using these two requirements, it is clear that a two-level system is the most simple quantum system that can be used as a working substance in a quantum Otto engine. As was stated in the previous sections, both the electronic and nuclear spin of the NV center can be seen as a two-level spin qubit system, implying that they can be used as working media for Otto engines. Lastly, to find a quantum analog for volume, one can look at the classical expansion and compression strokes. The engine delivers work in the expansion stroke, when going from a small volume to a large one. In quantum mechanics, the work is related to the energy difference between the two energy levels. Therefore, the 'volume' of the quantum system can also be linked to the distance between the two energy levels of a system. If the energetic difference is large, more work can be performed when transitioning to the lower energy state than when the energetic difference is small. Therefore, the inverse size of the energy gap between the two energetic states can be used as a quantum analog of volume, so that for a quantum Otto engine the work will be delivered in the energy gap compression stroke (whereas for a classic Otto engine this would be in the volume expansion stroke). Using this interpretation, the quantum isochoric processes [3] involve changing the energy level occupations (and thus the system entropy), without changing the energy levels themselves, until the working substance is in equilibrium with a certain heat bath. This shows quantum isochoric processes are quite similar to classical isochoric processes, since they both involve a change in temperature through a heat exchange without any work performed.

Apart from the change in interpretation of work and heat, the concept of adiabaticity [40] also changes going from a classical engine to a quantum engine. The isentropic strokes $1 \to 2$ and $3 \to 4$ are necessarily adiabatic in both the classical and quantum heat engine. A classical adiabatic process can be achieved through rapid expansion and compression over the working substance to guarantee that there is no heat exchange with the thermal baths. This requires a fast driving. In contrast, quantum adiabatic processes require that the populations of energy levels of the working substance remain constant as a certain internal (e.g. volume) or external (e.g.

magnetic field) variable changes, ensuring that the entropy remains unchanged. This implies a quasi-static process, where a very slow driving assures that no excitations are happening in the system and the populations remain constant. Deffner and Campbell define this difference in interpretation [3] as follows: “Quantum adiabatic processes form only a subset of classical adiabatic processes”. This refers to the fact that the classical and quantum Otto cycles are different not only in timescale, but also in their physical concept.

Note also that a classical Otto cycle has all the four stages in thermodynamic equilibrium so that the cycle as a whole is a reversible process. A quantum Otto cycle only reaches thermal equilibrium in two stages of the cycle, which introduces irreversibility [38]. It still equilibrates with the thermal reservoirs, as in the classical case, but there is no equilibrium reached in the isentropic strokes. This means that in the isentropic strokes, only points 1 and 3 are equilibrium points, which is enough to ensure the entropy conservation along the adiabatic paths and allows to calculate the entropy values S_2 and S_4 using the same thermal probabilities as in points 1 and 3. This local thermal equilibrium condition at the end of each stroke is also what separates the quantum Otto cycle from the Carnot cycle [3]. In the Carnot cycle, the adiabatic strokes are also isothermal, which requires that both work and heat must be exchanged with the thermal reservoir in order to keep the temperature of the working substance equal to the reservoir temperature. This results in a thermodynamically reversible isothermal process and there is zero irreversible entropy production. As the Otto cycle on the other hand only requires a local thermal equilibrium at the end of each stroke, the working substance will be in a thermal state with temperature T_h at the end of the power stroke $3 \to 4$. The subsequent thermalization of the working substance through isochoric cooling in contact with the cold thermal reservoir is accompanied with an irreversible entropy production.

5.7.2 The Quantum Otto cycle in a two level system

Consider a generic two level system with energy eigenvalues $\{E_g, E_e\}$ and eigenvectors $\{|\psi_g\rangle, |\psi_e\rangle\}$. The Hamiltonian of such a system is given by formula (23) [3].

$$\hat{H} = E_g|\psi_g\rangle\langle\psi_g| + E_e|\psi_e\rangle\langle\psi_e| \quad (23)$$

Rescaling this Hamiltonian such that $E_g = 0$, this gives:

$$\begin{aligned} \hat{H} &= (E_e - E_g)|\psi_e\rangle\langle\psi_e| && \text{(24a)} \\ &= \Delta|\psi_e\rangle\langle\psi_e| && \text{(24b)} \end{aligned}$$

The thermal state corresponding to this two-level system at a temperature T is given by formula (25). Here, p_g and p_e are the probabilities of the system being in the ground or excited state. During the Otto cycle, these probabilities will vary from p_g^i and p_e^i to p_g^f and p_e^f and back again. The energy level splitting will be varied between Δ_i and Δ_f, with $\Delta_f > \Delta_i$.

$$\rho^{eq} = p_g|\psi_g\rangle\langle\psi_g| + p_e|\psi_e\rangle\langle\psi_e| \quad (25)$$

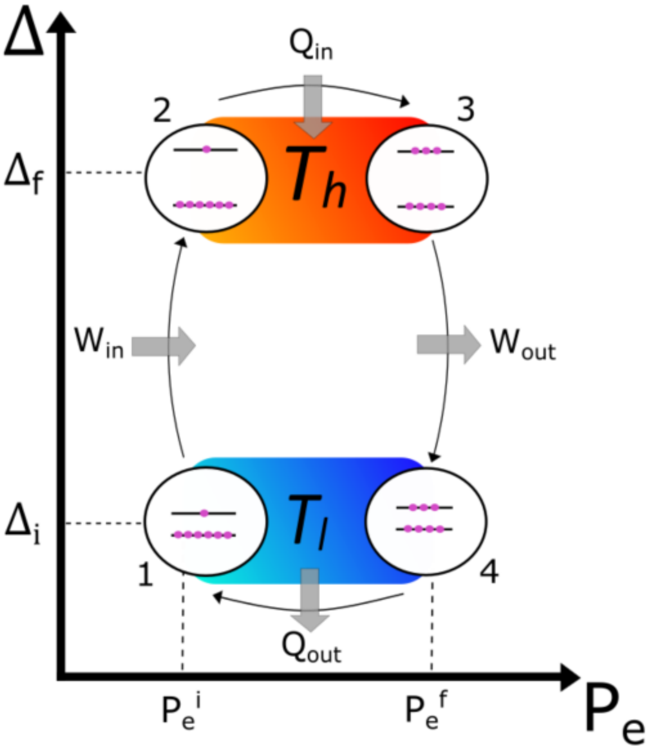

Figure 11: Quantum Otto cycle. The vertical axis represents the gap between the two energy levels of the working substance, which is varied between a low value Δ_1 and a high value Δ_2. The horizontal axis represents the probability of being in the excited state, which is also varied from a low value p_e^1 to a high value p_e^2. Stroke $1 \rightarrow 2$ and stroke $3 \rightarrow 4$ are isentropic (adiabatic) and stroke $2 \rightarrow 3$ and $4 \rightarrow 1$ are isochoric. The circles indicate the energy levels in the cycle and their populations.

The quantum Otto cycle then consists out of four strokes [3] which will be explained in detail below.

Isentropic energy gap expansion

Assuming that the working substance is initially in thermal equilibrium with the cold bath, T_1

is equal to T_l. Then, during the adiabatic stroke $1 \to 2$, work is performed to increase the energy splitting from Δ_i to Δ_f. Since no heat is exchanged during this isentropic expansion, the populations at the start and end of this stroke are equal: $p_g^1 = p_g^2 = p_g^i$ and $p_e^1 = p_e^2 = p_e^i$. However, in order for these equations to hold, the state of the working substance at point 2 cannot be in the thermal equilibrium with the cold bath anymore. An effective local temperature can be defined at point 2 as follows:

$$\begin{array}{rlll} & p_e^1 & = & p_e^2 \\ \Rightarrow & e^{-\Delta_i/k_B T_l} & = & e^{-\Delta_f/k_B T_2} \\ \Rightarrow & T_2 & = & \frac{\Delta_f}{\Delta_i} T_l \end{array} \qquad (26)$$

As the process is adiabatic, the change in internal energy going from point 1 to point 2 is entirely due to work $W_{1\to2}$.

$$W_{1\to2} = \sum_{n=g,e} \int_1^2 p_n dE_n \qquad (27)$$

Keeping the ground state energy fixed at zero, this can be rewritten as follows:

$$\begin{aligned} W_{1\to2} &= (E_e^2 - E_g^2)p_e^2 - (E_e^1 - E_g^1)p_e^1 && (28a) \\ &= \Delta_f \frac{e^{-\Delta_f/k_B T_2}}{1+e^{-\Delta_f/k_B T_2}} - \Delta_i \frac{e^{-\Delta_i/k_B T_l}}{1+e^{-\Delta_i/k_B T_l}} \\ &= \Delta_f \frac{e^{-\Delta_i/k_B T_l}}{1+e^{-\Delta_i/k_B T_l}} - \Delta_i \frac{e^{-\Delta_i/k_B T_l}}{1+e^{-\Delta_i/k_B T_l}} \\ &= \frac{\Delta_f - \Delta_i}{2} \frac{2e^{-\Delta_i/k_B T_l}}{1+e^{-\Delta_i/k_B T_l}} \\ &= \frac{\Delta_f - \Delta_i}{2}[1 - tanh(\frac{\Delta_i}{2k_B T_l})] && (28b) \end{aligned}$$

Isochoric heating

After the isentropic expansion, the two-level system is connected to the thermal reservoir at high temperature T_h. While equilibrating with the bath, the energy eigenvalues remain constant. The internal energy change in this isochoric heating stroke is thus equal to the heat exchange from the bath to the working substance $Q_{2\to3}$.

$$\begin{aligned} Q_{2\to3} &= \sum_{n=g,e} \int_2^3 p_n dE_n && (29a) \\ &= (E_e^3 - E_g^3)p_e^3 - (E_e^2 - E_g^2)p_e^2 && (29b) \\ &= \Delta_f \frac{e^{-\Delta_f/k_B T_h}}{1+e^{-\Delta_f/k_B T_h}} - \Delta_f \frac{e^{-\Delta_f/k_B T_2}}{1+e^{-\Delta_f/k_B T_2}} \\ &= \frac{\Delta_f}{2}[tanh(\frac{\Delta_f}{2k_B T_2}) - tanh(\frac{\Delta_f}{2k_B T_h})] && (29c) \end{aligned}$$

Isentropic energy gap compression

During the isentropic compression, also called the power stroke, work is extracted by reducing the energy gap of the working substance from Δ_f to Δ_i. Similar to the first stroke, no heat is exchanged and the occupations remain invariant: $p_g^3 = p_g^4 = p_g^f$ and $p_e^3 = p_e^4 = p_e^f$. This means that analogously to the isentropic expansion stroke, one can derive a local effective temperature at point 4.

$$T_4 = \frac{\Delta_i}{\Delta_f} T_h \tag{30}$$

And one can determine a formula for the delivered work $W_{3\to4}$.

$$W_{3\to4} = \sum_{n=g,e} \int_3^4 p_n dE_n \tag{31a}$$

$$= (E_e^4 - E_g^4)p_e^4 - (E_e^3 - E_g^3)p_e^3 \tag{31b}$$

$$= \Delta_i \frac{e^{-\Delta_i/k_B T_h}}{1+e^{-\Delta_i/k_B T_h}} - \Delta_f \frac{e^{-\Delta_f/k_B T_4}}{1+e^{-\Delta_f/k_B T_4}}$$

$$= -\frac{\Delta_f - \Delta_i}{2}[1 - tanh(\frac{\Delta_f}{2k_B T_h})] \tag{31c}$$

Isochoric cooling

The isochoric cooling stroke returns the two level system back to its initial state. For this, the working substance is connected to a thermal reservoir at low temperature T_l and heat is exchanged with this bath. Similar to the isochoric heating stroke, one can derive that the heat $Q_{4\to1}$ lost to the cold bath is given by:

$$Q_{4\to1} = \sum_{n=g,e} \int_4^1 p_n dE_n \tag{32a}$$

$$= (E_e^1 - E_g^1)p_e^1 - (E_e^4 - E_g^4)p_e^4 \tag{32b}$$

$$= \Delta_i \frac{e^{-\Delta_i/k_B T_l}}{1+e^{-\Delta_i/k_B T_l}} - \Delta_i \frac{e^{-\Delta_i/k_B T_4}}{1+e^{-\Delta_i/k_B T_4}}$$

$$= -\frac{\Delta_i}{2}[tanh(\frac{\Delta_i}{2k_B T_4}) - tanh(\frac{\Delta_i}{2k_B T_l})] \tag{32c}$$

5.7.3 Efficiency of the quantum Otto cycle and positive work condition

Using the formulas (26) and (30) for the effective temperatures of the working substance at point 2 and 4, the work and heat exchanges can be expressed purely in terms of the bath temperatures and the energy splittings.

$$W_{1\to2} = \frac{\Delta_f - \Delta_i}{2}[1 - tanh(\frac{\Delta_i}{2k_B T_l})] \tag{33a}$$

$$Q_{2\to3} = \frac{\Delta_f}{2}[tanh(\frac{\Delta_i}{2k_B T_l}) - tanh(\frac{\Delta_f}{2k_B T_h})] \tag{33b}$$

$$W_{3\to4} = -\frac{\Delta_f - \Delta_i}{2}[1 - tanh(\frac{\Delta_f}{2k_B T_h})] \tag{33c}$$

$$Q_{4\to1} = -\frac{\Delta_i}{2}[tanh(\frac{\Delta_f}{2k_B T_h}) - tanh(\frac{\Delta_i}{2k_B T_l})] \tag{33d}$$

The net work W that can be extracted from the working substance in the quantum Otto cycle is given by formula (34) below [3]. The minus sign in the first equation is added to receive a positive output work (conventionally, work leaving the system is negative).

$$\begin{aligned} W &= -(W_{1\to 2} + W_{3\to 4}) && \text{(34a)} \\ &= \tfrac{\Delta_f - \Delta_i}{2}[1 - tanh(\tfrac{\Delta_f}{2k_BT_h})] - \tfrac{\Delta_f - \Delta_i}{2}[1 - tanh(\tfrac{\Delta_i}{2k_BT_l})] \\ &= \tfrac{\Delta_f - \Delta_i}{2}[tanh(\tfrac{\Delta_i}{2k_BT_l}) - tanh(\tfrac{\Delta_f}{2k_BT_h})] && \text{(34b)} \end{aligned}$$

The Otto efficiency [3] can then be calculated as follows:

$$\begin{aligned} \eta &= \tfrac{W}{Q_{2\to 3}} && \text{(35a)} \\ &= 1 - \tfrac{\Delta_i}{\Delta_f} && \text{(35b)} \end{aligned}$$

Because of the assumption that $\Delta_f > \Delta_i$, the net work output is positive when:

$$\begin{aligned} & tanh(\tfrac{\Delta_i}{2k_BT_l}) && > && tanh(\tfrac{\Delta_f}{2k_BT_h}) \\ \Rightarrow\ & \tfrac{\Delta_i}{T_l} && > && \tfrac{\Delta_f}{T_h} \\ \Rightarrow\ & \tfrac{T_h}{T_l} && > && \tfrac{\Delta_f}{\Delta_i} && \text{(36)} \end{aligned}$$

This quantum positive work condition limits the quantum Otto efficiency to be smaller than the Carnot efficiency, just as in the classical case. For a classical Otto engine, work can be extracted when T_h is larger than T_l. For quantum Otto engines, this condition is necessary but not sufficient. Work can only be extracted when T_h is larger than $\frac{\Delta_f}{\Delta_i}T_l$. This indicates that the second law in quantum thermodynamics is not just an expansion of the classical second law of thermodynamics, but a refinement of it [41].

5.7.4 Counteradiabatic driving

The active manipulation of quantum systems is both the strength of quantum thermodynamics and one of its major roadblocks. Traditionally, thermodynamic transformations are always quasi-static, meaning that the system of interest is always kept at equilibrium. If an arbitrary finite time transformation has to be made, then this would always require some thermodynamic control [6] that has the power to avoid any form of irreversibility induced by manipulating the system on short timescales. An example of such thermodynamic controls are the *Shortcuts to adiabaticity* (STA) which make sure that the system of interest reaches an adiabatic state of a certain transformation within a finite time. A specific example of such an STA technique is called counteradiabatic driving (CD). This technique stands out among other STA methods because it ensures that the system follows the adiabatic eigenstates at all times (instead of just ending up in an adiabatic state) by introducing an external control Hamiltonian $\hat{H}_{CD}$. This is important because if there are transitions between the eigenstates in the finite-time driving, this leads to the build up of quantum coherences in the energy basis and the additional energy stored in these coherences is dissipated in the subsequent thermal stages of the engine cycle. This is why the term "quantum internal friction" is sometimes used to describe the effect [42].

Practical heat engines (both classical and quantum) operate far from the maximum efficiency condition set by Carnot and are optimized for maximum power, sacrificing efficiency. For quantum heat engines, this trade-off is much larger, because they require an infinitely slow driving of the adiabatic strokes to reach maximum efficiency, limiting output power to zero. Therefore, quantum heat engines can benefit a lot from the aforementioned quantum controls [4].

To see how CD works, imagine a quantum system with Hamiltonian $\hat{H}_0(t)$ and instantaneous eigenstates and energies given by:

$$\hat{H}_0(t)|n(t)\rangle = E_n(t)|n(t)\rangle \quad (37)$$

A time-varying Hamiltonian typically introduces transitions between the quantum states that are driven by it. If the change is slow, one can refer to this change using the adiabatic basis, which is the eigenbasis of the instantaneous ('frozen') Hamiltonian $\hat{H}_0(t)$. In this approximation, the states (containing both dynamical and geometrical phases) driven by $\hat{H}_0(t)$ are:

$$|\psi_n(t)\rangle = \exp\left[\frac{1}{i\hbar}\int_0^t dt' E_n(t') - \int_0^t dt' \langle n(t')|\delta_{t'} n(t')\rangle\right]|n(t)\rangle \quad (38)$$

Although the transition amplitude is small when slowly varying $\hat{H}_0$, it is not zero. Therefore, in the counteradiabatic driving method, one searches a Hamiltonian $\hat{H}_{CD}(t)$ for which the transition probabilities are zero. In other words, one searches $\hat{H}_{CD}(t)$ such that:

$$i\hbar\delta_t|\psi_n(t)\rangle = \hat{H}_{CD}(t)|\psi_n(t)\rangle \quad (39)$$

For this CD-Hamiltonian, the eigenstates must follow $|n(t)\rangle$ exactly, so that there are no transitions between the eigenstates of $\hat{H}_0(t)$ at any time (instead of just at infinity). M. V. Berry demonstrated [43] that this counteradiabatic driving Hamiltonian can be written as:

$$\begin{aligned}\hat{H}_{CD}(t) &= \textstyle\sum_n |n(t)\rangle E_n(t)\langle n(t)| + i\hbar \sum_n (|\delta_t n(t)\rangle\langle n(t)| - \langle n(t)|\delta_t n(t)\rangle |n(t)\rangle\langle n(t)|) && (40a)\\ &= \hat{H}_0(t) + \hat{H}_1(t) && (40b)\end{aligned}$$

A more involved derivation of this formula can be found in appendix A. By differentiating equation (37) with respect to time and then multiplying with the bra $\langle m(t)|$ on the left, it can be found that:

$$\langle m(t)|\delta_t n(t)\rangle \quad = \quad \frac{\langle m(t)|\delta_t \hat{H}_0(t)|n(t)\rangle}{E_n(t)-E_m(t)} \qquad (41)$$

Inserting a decomposition of the identity into formula (40) and substituting formula (41), provides a convenient expression for $\hat{H}_1(t)$. Note that this single CD Hamiltonian works for all the states $|n(t)\rangle$, so that $\{|n(t)\rangle\}$ can be regarded as the set of 'moving eigenstates' of $\hat{H}_{CD}(t)$.

$$\hat{H}_1(t) \quad = \quad i\hbar \sum_n \sum_{m\neq n} \frac{|m(t)\rangle\langle m(t)|\delta_t \hat{H}_0(t)|n(t)\rangle\langle n(t)|}{E_n - E_m} \qquad (42)$$

The Hamiltonian $\hat{H}_{CD}(t)$ is only specified up until a constant energy term, meaning there are infinitely many CD Hamiltonians that can generate the evolution $|n(t)\rangle$ and they differ only in a constant. The simplest choice is to take $E_n(t)$ equal to zero, so that the corresponding eigenstates $|n(t)\rangle$ have no phase factors and are driven by:

$$\hat{H}_{CD}(t) \quad = \quad i\hbar \sum_n |\delta_t n(t)\rangle\langle n(t)| \qquad (43)$$

As a special example, the following Hamiltonian can be used to drive a spin system in an ambient magnetic field without transitions [43]. This is relevant, because the envisioned NV-based quantum Otto engine shall consist of two spins in an ambient magnetic field. The derivation of this formula can be seen in appendix B.

$$\hat{H}_{CD}(t) \quad = \quad [\gamma \boldsymbol{B}_0(t) + \tfrac{1}{B_0(t)^2}\boldsymbol{B}_0(t) \times \delta_t \boldsymbol{B}_0(t)] \cdot \boldsymbol{S} \qquad (44)$$

5.7.5 Theoretical design of a quantum Otto engine based on NV centers

NV centers are interesting working substances for quantum Otto engines because of their coupling to naturally occurring spin baths in diamond, such as ^{13}C or ^{14}N spins, their long coherence times and the optical polarization of the NV electron spin ($\sim$ 95% ground state polarization, corresponding to a spin temperature of $\sim$ 7 mK at zero magnetic field) [2]. These properties inspired Klatzow et al. [16] to demonstrate quantum effects in microscopic heat engines for the first time in 2017 using ensembles of NV centers. These quantum effects, also called the quantum thermodynamic signatures, are what truly differentiates quantum heat engines from their classical counterparts. The origin of these signatures is the fact that quantum heat engines may posses coherence between their internal states, which can act as a power boost in some circumstances (as compared to classical heat engines using the same resources) [44] or can result in the thermodynamic equivalence of different quantum heat engine types [45].

The purpose of this thesis is to propose a simple quantum Otto cycle prototype in diamond using the NV electron and associated ^{14}N spin. Because the electron spin and nuclear spin are weakly coupled by the hyperfine interaction, the two-qubit system resembles the set-up used by Peterson et al. [46] [47] to create a finite-time quantum Otto engine based on a spin-$1/2$ system and nuclear magnetic resonance (NMR) techniques. As the proposed NV-based quantum Otto engine has almost the same protocol as the NMR-based one, apart from the initialization protocol and coupling mechanism of the spins, the work by Peterson et al. will be explained first. All the changes in the density operators in the presented pulse protocol were verified using MatLab.

In the NMR-based quantum Otto engine, a ^{13}C labeled CHCl$_3$ liquid sample diluted in Acetone-D6 was used, providing the working medium (^{13}C nuclear spin), heat bus (^{1}H nuclear spin), and weakly coupled environment (chlorine isotopes). This sample was placed in a large static magnetic field, which defined the z-axis. The magnetization of the nuclear spins was controlled using time-modulated RF fields in the x- and y-direction and longitudinal field gradient pulses. The hot environment was created by high-RF modes near the Larmor frequency of ^{1}H (~ 500 MHz), and the cold environment by low-RF modes near the Larmor frequency of ^{13}C (~ 125 MHz). The rotating frame is used to simplify calculations. This is the case both for the ^{13}C spin and the ^{1}H spin. Figure 12 shows the protocol used to extract work from the carbon spin.

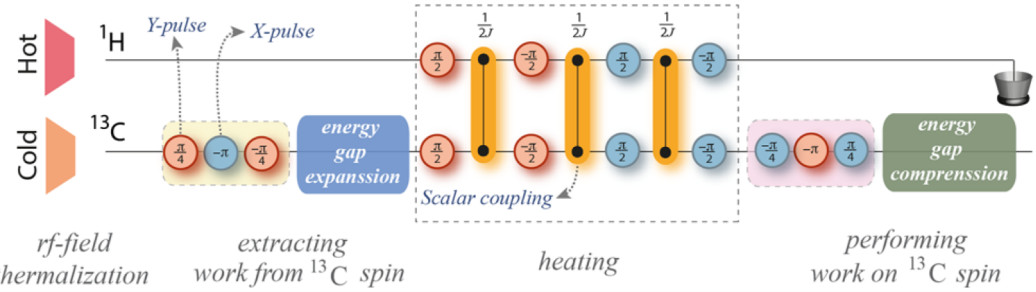

Figure 12: Simplified NMR-based quantum Otto pulse protocol. The ^{1}H and ^{13}C spins are initially prepared in a hot and a cold thermal state. Blue circles represent RF pulses inducing rotations around the x-axis, and red circles around the y-axis. Orange connections indicate an evolution under the scalar interaction $\hat{H}_J$ for a time $1/2J$. Here, the ^{1}H spin is used as a heat bus, delivering heat to ^{13}C. The unitary driving for expansion and compression is implemented using a time-modulated RF field on resonance with the carbon Larmor frequency. [46].

At the start of this protocol, both spins have been prepared in pseudothermal states. For ^{13}C the prepared state corresponds to $k_B T_l = 6.6 \pm 0.1$ peV and for ^{1}H both $k_B T_h^1 = 21.5 \pm 0.4$ and

$k_BT_h^2 = 40.5 \pm 3.7$ are used and compared. This initial state preparation is performed using spatial average techniques using RF and gradient fields, and represents the cooling stroke. The approximate density matrices rho_C^1 and rho_H^1 after this state preparation are given in formula (45) for high temperature T_h^1.

$$\rho_C^1 \approx \begin{pmatrix} 0.78 & 0 \\ 0 & 0.22 \end{pmatrix} \quad \rho_H^1 \approx \begin{pmatrix} 0.67 & 0 \\ 0 & 0.33 \end{pmatrix} \quad (45)$$

After this, three RF pulses are applied to the carbon spin, changing its density operator to $\rho_C^2 = \rho_{eq}^1 = exp(\frac{-\hat{H}_1^C}{kBT_l})/Z_1$, where $\hat{H}_1^C = -h\nu_1 I_x^C$ ($\nu_1 = 2.0$ kHz) and $Z_1 = Tr[exp(\frac{-\hat{H}_1^C}{kBT_l})]$. Filling in the formulas, this gives:

$$\rho_C^2 \approx \begin{pmatrix} 0.5 & 0.28 \\ 0.28 & 0.5 \end{pmatrix} \quad (46)$$

To obtain this density operator from ρ_C^1, one needs an expression for the unitary rotation operator $\hat{U}_R^i(\alpha)$ over an angle α around the i-axis (i = x, y or z). This formula [48] is given below and can be adapted to any α and i present in the pulse sequence. After creating the rotation operator, one can apply this to the density matrix ρ in the following manner: $\hat{U}_R^i(\alpha)^\dagger \rho \hat{U}_R^i(\alpha)$. This gives the same result as ρ_{eq}^1.

$$\hat{U}_R^i(\alpha) = exp(-i\alpha S_i) \quad (47)$$

In the expansion stroke, the energy level splitting is increased by changing the RF field gradually during a certain time τ. This time was varied by the authors between 100 and 700 μs to better understand the effect of finite-time driving. Starting at $t = 0$, the Hamiltonian $\hat{H}_{exp}^C = -h\nu(t)[cos(\pi t/2\tau)S_x^C + sin(\pi t/2\tau)S_y^C]$ (with $\nu(t) = \nu_1[1 - t/\tau] + \nu_2 t/\tau$) changes from $\hat{H}_1^C$ to $\hat{H}_2^C = -h\nu_2 S_y^C$ ($\nu_2 = 3.6$ kHz). Because of this, the density matrix of the carbon spin is no longer diagonal in the energy eigenbasis of the final Hamiltonian.

In the heating stroke, heat is transferred from ^{1}H to ^{13}C via the scalar coupling (J-coupling) between the two spins. This happens gradually using four sets of RF pulses and three intermediate evolutions under the J-coupling Hamiltonian (each for a duration of $1/2J$). To simulate this coupling, it is important to work with the combined density matrix of the two-spin system $\rho_{C,H} = \rho_C^2 \otimes \rho_H^1$ so that the scalar coupling Hamiltonian $\hat{H}_J = 2\pi\hbar J I_z^C I_z^H$ can work on both spins at the same time. The unitary operator that evolves the system state under $\hat{H}_J$ is given by

$\hat{U}_J(t) = exp(-i\hat{H}_J t/\hbar)$, which can be found by inspection of the time dependent Schrödinger equation. This operator is then applied to the combined density matrix in the same manner as the previous rotation operators were applied to the carbon density matrix. After heating, the individual density operators can be found using formula (11). This gives:

$$\rho_C^3 \approx \begin{pmatrix} 0.67 & 0 \\ 0 & 0.33 \end{pmatrix} \quad \rho_H^3 \approx \begin{pmatrix} 0.5 & 0.28 \\ 0.28 & 0.5 \end{pmatrix} \tag{48}$$

After thermalization with the RF field (using three RF-pulse induced rotations of the Bloch vector), the carbon spin has reached the hot thermal state given by $\rho_C^4 = \rho_{eq}^2 = exp(\frac{-\hat{H}_2^C}{kBTh^1})/Z_2$, where $\hat{H}_C^2$ was given above and $Z_2 = Tr[exp(\frac{-\hat{H}_2^C}{kBTh^1})]$. The approximate density operator is given below.

$$\rho_C^4 \approx \begin{pmatrix} 0.5 & -0.17i \\ 0.17i & 0.5 \end{pmatrix} \tag{49}$$

Lastly, an energy gap compression is performed using the time-reversed process of the expansion protocol. This means that the system evolves under $\hat{H}_{comp}^C(t) = -\hat{H}_{exp}^C(\tau - t)$.

The delivered work and absorbed heat can be calculated using the following formulas, also taken from Peterson et al. [46]. These formulas take into account the reduction of delivered work and absorbed heat due to the occurrence of transitions (with probability ξ) in the expansion and compression strokes.

$$W = \tfrac{\Delta_f - \Delta_i}{2}[tanh(\tfrac{\Delta_i}{2k_BT_l}) - tanh(\tfrac{\Delta_f}{2k_BT_h})] - \xi[\Delta_i tanh(\tfrac{\Delta_f}{2k_BT_h}) + \Delta_f tanh(\tfrac{\Delta_i}{2k_BT_l})] \tag{50}$$

$$Q = \tfrac{\Delta_f}{2}[tanh(\tfrac{\Delta_i}{2k_BT_l}) - tanh(\tfrac{\Delta_f}{2k_BT_h})] - \xi\Delta_f tanh(\tfrac{\Delta_i}{2k_BT_l}) \tag{51}$$

When using a counteradiabatic driving Hamiltonian, the second term in both formulas can be discarded since one is certain that no transitions will occur. However, as this is not the case, one must account for the possibility of transitions. Using the experimentally determined transition probability $\xi \approx 0.02$ for a compression and expansion time of 700 μs, the results from Peterson et al. [46] are checked. In particular, extracted work W, efficiency $\eta = W/Q$ and output power P. As these values were only provided in a graph, they have a high uncertainty, but seem to lie close to the obtained result, indicating a successful simulation of the experiment. This is also the case when using T_h^2 as temperature of the hot bath. However, it must be noted that the power values were determined using a cycle time of 1.4 ms, which is equal to the duration of the expansion and compression strokes. However, when taking into account the duration of the other strokes as well (without the initialization of the spins), the duration of the protocol is longer and the output power drops.

As stated, an NV-based Otto engine can be created similarly to the ^{13}C-based engine. In the current version, the NV electron spin is assigned the role of the heat bus, the associated ^{14}N spin becomes the working substance, MW modes near the electron Larmor frequency ν_e make up the hot environment and RF modes near the ^{14}N Larmor frequency ν_N the cold environment. These frequencies are equal to respectively 280.24 MHz [49] and -30.766 [50] kHz in an ambient magnetic field of 10 mT. The opposite signs express the opposite rotation direction when precessing around the magnetic field. The hyperfine coupling between the electron and nuclear spin allows for the heat exchange. Apart from the initial state preparation of the two nuclear spins, the pulse protocol from the NMR-based Otto engine can essentially be used with an adapted coupling mechanism (hyperfine coupling through an evolution under the Hamiltonian $H_{hfs} = 2\pi\hbar A S_z I_z$ for a time of $1/2A$). This is depicted on figure 13 below.

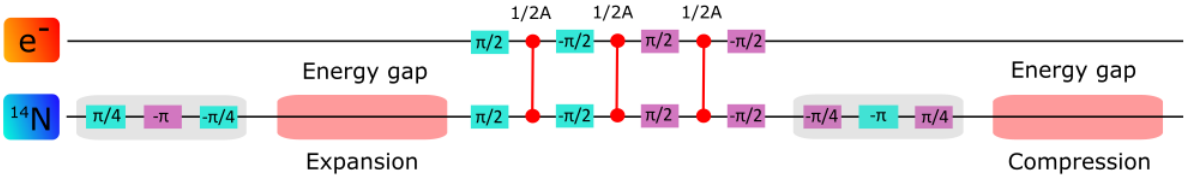

Figure 13: Simplified prototype of an NV-based quantum Otto pulse protocol. The pulse sequence is based on the work of Peterson et al. [46]. Only the use of the NV electron and nuclear spin in this sequence is new. The electron and ^{14}N spins are initially prepared in a hot and a cold thermal state. Purple boxes represent RF pulses inducing rotations around the x-axis, and blue boxes around the y-axis. Red connections indicate an evolution under the hyperfine interaction during a time $1/2A$, where A is the hyperfine coupling constant. Lastly, the unitary driving for expansion and compression is implemented using a time-modulated RF field on resonance with the nitrogen Larmor frequency.

Although the actual Otto cycle protocol is almost identical to the work by Peterson at al. [46], I designed a prototype initalization protocol for both spins. To create the desired thermal starting states, the NV electron spin and associated ^{14}N nuclear spin are manipulated using MW-, RF- and laser pulses. Since both spins have $S = 1$, the system is actually a three-level system, but it can be used as an approximate two-level system. For this to be true, one has to reduce the population of the third energy level and withhold from any manipulation of this level. Here, the states $|0\rangle_e$ and $|-1\rangle_e$ are chosen as the electronic two-level system and the $|0\rangle_N$ and $|1\rangle_N$ as the nuclear one. The initialization protocol is illustrated in figure 14 and was also experimentally verified (see page 62). It starts with both spins in a maximally mixed state, where the probability of having any nuclear or electronic spin is equal to $1/3$.

A long laser pulse is applied to the system, polarizing the electron spin to $|0\rangle_e$. Then a nuclear spin-selective MW pulse is applied to the electron spin. This pulse flips the electron spin based on the value of the nuclear spin, a property made possible by the hyperfine interaction between both spins. Specifically, the electron spin is flipped to $|-1\rangle_e$ when the nuclear spin is equal to $|-1\rangle_N$. Then, an RF pulse induces a nuclear spin transition $|-1\rangle_N \rightarrow |0\rangle_N$, while the electron spin is still in the excited $|-1\rangle_e$ state. Lastly, a laser pulse is applied to bring the electron spin back to $|0\rangle_e$, while leaving the nuclear spin untouched. If this laser pulse is long enough, the electron spin will once again be polarized to $|0\rangle_e$, while the nuclear spin will be partly polarized to $|0\rangle_N$. This is also what is presented experimentally. However, by reducing the length of the laser pulse, a tunable mixed state can be created between $|0\rangle_e$ and $|-1\rangle_e$: the longer the laser pulse, the more population will be in the lower energy level. This allows to control the electron spin temperature. However, this is also linked to the nuclear spin temperature, since the population of the $|0\rangle_N$ energy level increases as well, when the electron spin polarizes. For the moment, the specific rates of these transitions are not known. They should be determined experimentally by performing a significant amount of parametric studies of laser power duration. Once the rate is known, it can be used to determine the laser pulse duration and amount of iterations for a certain set of initial temperatures. Note that during the initialization, the electron and ^{14}N spin are actively manipulated together (e.g. nuclear spin-selective MW pulses inducing rotations of the electron spin). Afterwards, the two spins shall only be manipulated separately, apart from allowing them to exchange heat due to their hyperfine coupling.

After determining the rate of laser-induced polarization and the temperatures to be used, another property of the nuclear spin must be calculated: the transition probability between the energy levels in the expansion and compression protocols. These probabilities can either be determined theoretically (e.g. using the Suzuki-Trotter approximation [51]) or experimentally (by QST). Alternatively, one could employ a counteradiabatic driving Hamiltonian to reduce

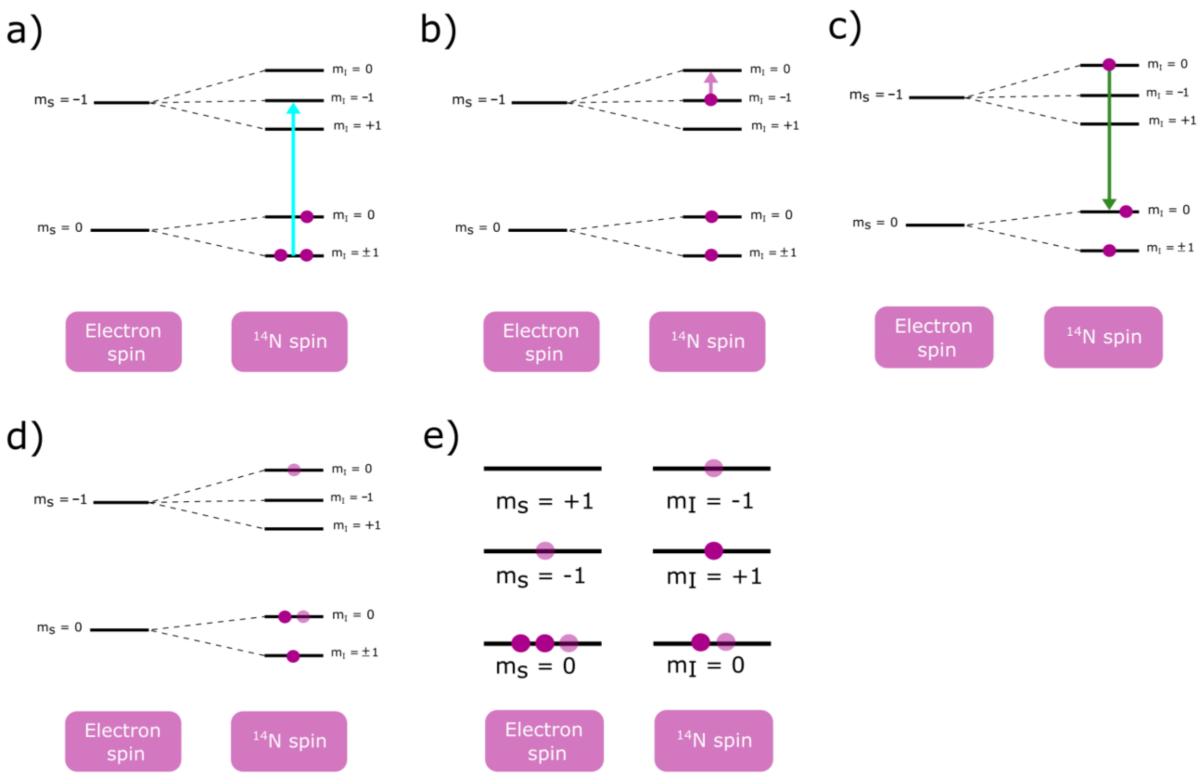

Figure 14: Initialization protocol of electron and ^{14}N nuclear spin for an NV-based quantum Otto engine. Populations are indicated by purple dots. In a) to d) electronic energy levels are shown, as well as the splitting due to the nuclear spin. In e) both electronic and nuclear energy levels are shown. The bottom two levels are always used in the two-level system, while the top energy level is mostly depleted. a) A nuclear spin-selective MW pulse flips the electron spin from $m_S = 0$ to $m_S = -1$ when $m_I = -1$. b) An RF-pulse flips the nuclear spin to $m_I = 0$, while leaving the electron spin untouched. c) A laser pulse partially repolarizes the electron spin to $m_S = 0$. d) The final state expressed using electron energy levels. Depending on the duration of the laser pulse, a certain amount of population was transferred to $|0, 0\rangle$. This is indicated by the sheer dot. e) The final state expressed using both electron and nuclear energy levels. As the distance between the electronic energy levels is much higher than for the nuclear energy levels, a certain population in $m_S = -1$ compared to $m_S = 0$ generates a much higher spin temperature than the same population would generate in $m_I = 1$ compared to $m_I = 0$.

these probabilities to zero. However, in this case, the work must be corrected in another manner because of the energetic cost of the CD driving source. It was demonstrated [42] that the total cost during the driving time of a general quantum Otto cycle is given by:

$$\langle \hat{H}_{CD}(\tau) \rangle \quad = \quad \int_0^\tau Tr[\rho_0(t) \tfrac{d}{dt} \hat{H}_{CD}(t)] dt \qquad (52)$$

When the transition probabilities are known, the NV-based quantum Otto cycle could be simulated using either a regular finite-time driving or using counteradiabatic driving. The work, efficiency and power output can then be compared to discover the optimal operation regime. After this, the experimental implementation of the Otto cycle using a single NV center in diamond can be pursued.

6 Experimental set-up

I have performed all experimental demonstrations in this thesis on the set-up shown schematically in figure 15. All experiments start with an optical initialization of the NV center spins. This is performed using a continuous wave, solid-state Gem 532 laser manufactured by Laser Quantum with an emission wavelength of 532 nm. The laser light passes a WPHSM05-532 half wave plate from Thorlabs and a PBS201 - 20 mm polarizing qube from Thorlabs, together providing power control. After focusing the laser light with a Thorlabs lens (L1) of type AC254-150-A-ML with a focus distance of 150.0 mm, pulsed operation is made possible by an acousto-optic modulator (AOM) of type AOMO 3200-146 made by Crystal Technology, Inc. The beam is focused by a set of lenses (L2) and pinholes (P1), which block the out-of-focus laser light and is finally reflected by a dichroic mirror (DM) of type DMLP567R from Thorlabs. All pinholes used in the set-up are Thorlabs P30S pinholes with a diameter of $30 \pm 2\mu$m, although the exact types of lenses and pinholes are not relevant here, as they are simply used to guide the beam towards the diamond sample. The dichroic mirror reflects light with a wavelength less than 567 nm, while light with longer wavelengths can pass through. This means that the laser light is reflected towards the diamond sample (where it is focused by a set of lenses (L2) on a certain single NV center) and that the red fluorescence emitted by the NV center can pass through towards the detector. Behind the dichroic mirror, a long-pass filter is placed to ensure that the laser light is blocked. This is a FELH05550 filter from Thorlabs and has a cut-off wavelength of 550 nm. After filtering, the light passes through a pinhole (P2) once again blocking the out-of-focus light. Then the beam is collimated by a final lens (L3), which is an FELH0550 type lens from Thorlabs, onto an SPCM-AQRH-14 single photon counter from Excelitas Technologies capturing the signal, which is then sent to the control PC. All signals are generated and read out on this PC via a LabView program. The constructed pulse sequences then go to a pulse generator, which is an arbitrary wave generator (AWG) of model M8190A from Keysight. This device generates the desired signals and sends them to the correct instruments: laser signals to the AOM, MW signals to the MW switch and RF signals to the RF switch. Both switches are connected separately to either a microwave or radiofrequency wave generator and an amplifier on the other end. The source of both the MW and RF signals is the mentioned AWG and the MW amplifier is a ZHL-16W-43-S+ type amplifier from Mini-Circuits, while the RF amplifier is a ZX60-100VH+ from Mini-Circuits. After amplification, both signals are sent to a diplexer of type D1276-0-250/2000-4000H-A from TTE, which combines them and then sends them through a copper wire towards the sample. After passing through an antenna fabricated on top of the diamond surface, the wire ends with a 50 Ohm terminator, which is necessary to avoid reflection back into the wire causing interference with the original signal. A detail of this PCB can also be seen in figure 15. On this detail, the diamond can be seen in the center with the lithographically deposited electrodes and MW/ RF antenna on top. The antenna is seen as a horizontal line connecting the diplexer and a 50Ω terminator and the electrodes are wirebonded vertically to the voltage source and preamplifier. These electrodes are present to perform electrically read measurements, but are not used in this thesis. They do make it easier to locate and distinguish NV centers based on their relative position to the antenna and electrodes.

The quality of the diamond sample is very important in experiments, since the T_2^* spin coherence time of the NV electron and nucleus are mostly limited by their interactions with the paramagnetic impurities embedded in the diamond matrix [21]. This spin bath is related to the electronic spins of nitrogen impurities and the nuclear spins of ^{13}C atoms. HPHT diamonds contain a lot of of nitrogen impurities and a low NV concentration. In contrast, isotopically purified CVD diamond is a very pure material which gives long spin coherence times, both for the longitudinal spin relaxation time ($\sim$ 5 ms) and the transversal relaxation time T_2 ($\sim$ 2 ms). These were at the time (2014) the longest ever observed values in a solid-state system at room temperature. A coherence of several orders of magnitude higher can be achieved at low temperatures [52]. The coherence time of the spins is important because it dictates the timescale on which a certain spin state can be kept constant. In this master thesis, measurements are performed on a single NV center in a type IIa electronic grade diamond with a (111)-surface, located between a nanofabricated antenna and electrode. In figure 16, the location of this NV center can be seen. The left side of figure 16 is an optical scan of the diamond sample parallel to the surface and the color legend indicates the amount of photons detected when a certain pixel is in focus of the laser light. On the left, the brighter part indicates the presence of an electrode and on the right this is the antenna. In between lies diamond filled with islands of fluorescence that correspond to defects. These defects are not necessarily NV centers: an ODMR measurement must be performed with the laser focused on this center to confirm this. Using the cursor, the in-plane focusing can be performed (this is not done on figure 16, but the NV center of interest is indicated with a white circle). Then a scan is conducted in the perpendicular direction (a z-scan) to focus on the correct depth within the diamond. Such an exemplary z-scan is shown on the right side of figure 16.

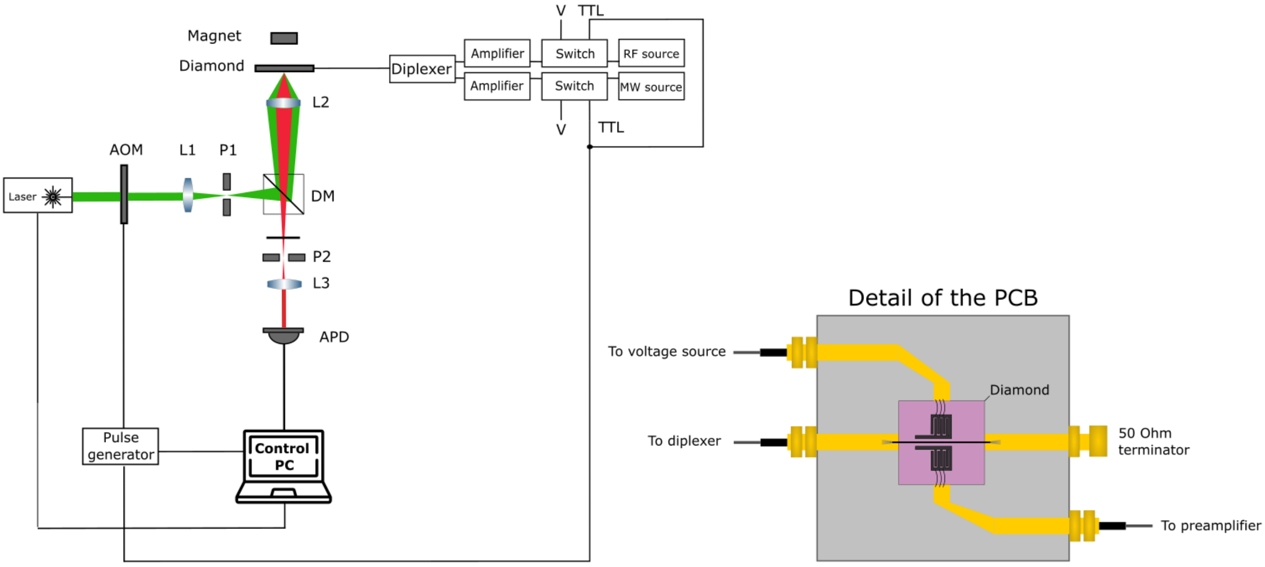

Figure 15: Simplified diagram of experimental set-up used to perform optical measurements of NV spin states. Left: components and optical paths. Right: detail of the PCB containing the diamond sample.

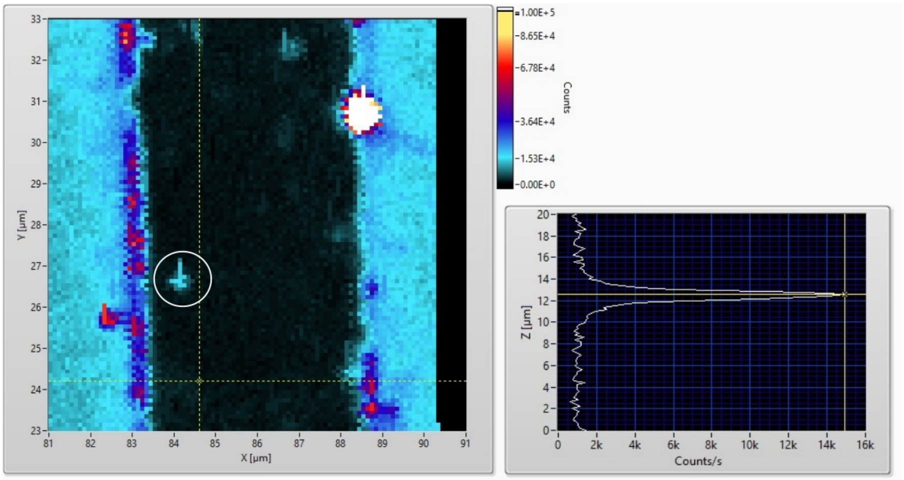

Figure 16: Optical determination of the location of defects in diamond. Left: xy-scan parallel to the diamond surface. Different colors indicate the amount of photons emitted by a certain pixel when in focus. Right: z-scan perpendicular to the diamond surface. The highest counts indicate the location of the defect. Note that it is not possible to distinguish NV centers from other fluorescent defects using this method, but can be done by performing ODMR or spectroscopy measurements.

7 Results and discussion

The experimental progress of this master thesis can be divided in two consecutive steps: manipulating the electronic and nuclear ^{14}N spin of a single NV center, and preparing the nuclear spin in an arbitrary state, of which the fidelity was checked with via the electron spin through quantum state tomography. Each of these steps will now be discussed in more detail. Note that in each experiment, the presented pulse sequence is repeated many times and the result is averaged over time.

7.1 Manipulation and read out of the electronic and nuclear NV spin

7.1.1 Electronic spin

As the electronic spin of an NV center is easily manipulated and read out optically [27] this is the starting point of the measurements. In fact, when performing a continuous wave ODMR read out, the presence of a dip at the resonance frequency of 2.87 GHz is seen as proof that the laser is focused on an NV center. Resolving individual hyperfine transitions requires the presence of a magnetic field, lifting the degeneracy of the electronic spin states $m_S = \pm 1$. Figure 17a) shows the protocol used for CW ODMR measurements and 17c) shows the result of such a measurement. The presence of two dips in intensity, located symmetrically around 2.87 GHz, confirms that there is an NV center in the focus of the laser. This measurement only shows the effect of of the ZFS and Zeeman term in the Hamiltonian. Using CW ODMR with a higher resolution, it is possible to see the effects of the hyperfine splitting as well. Power broadening can obscure this hyperfine structure, which is why pulsed ODMR (protocol in figure 17b)) is used instead. It's important to resolve this hyperfine structure (which is made possible through the long coherence time of the NV center providing small spectral linewidths of electron spin transitions [53]), because this is what gives access to the nuclear spin states through ENDOR measurements of the electronic spin. When one knows the resonance frequency of a certain $|0, m_I\rangle \leftrightarrow |\pm 1, m_I\rangle$ transition, one can selectively excite the nuclear state m_I in other pulse protocols. The result can be seen in figure 17d). From the Lorentzian fit, the resonance frequency of the $|0, 0\rangle \leftrightarrow |-1, 0\rangle$ transition is 2852 MHz, the resonance frequency of the $|0, 1\rangle \leftrightarrow |-1, 1\rangle$ transition is 2849.84 MHz and for the $|0, -1\rangle \leftrightarrow |-1, -1\rangle$ transition this is 2854.16 MHz. Note that these resonance frequencies are not fixed, but depending both on the magnetic field strength and other environmental effects. Therefore, later on other MW frequencies will be used to address the same transitions.

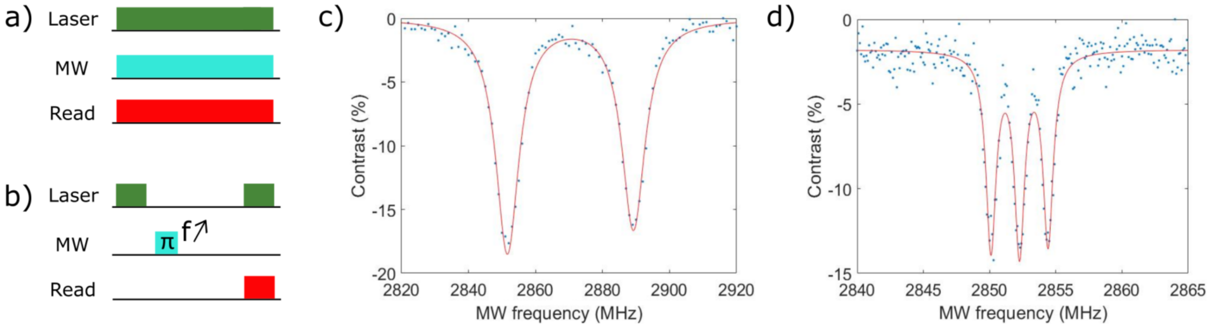

Figure 17: Manipulation and read-out of the electronic state of the NV center. a) Continuous wave ODMR protocol. b) Pulsed ODMR protocol. The symbol above the MW π-pulse indicates that the frequency of this pulse is swept. This means that in every iteration of the sequence, the frequency of the MW magnetic field is increased stepwise between two predefined values. When all frequencies have been employed, the next pulse sequence uses again the first frequency and the protocol repeats itself. c) PL spectrum measured in a CW ODMR experiment. d) PL spectrum measured in a pulsed ODMR experiment. Hyperfine and quadrupole effects are visible due to a decreased power broadening and an increased resolution.

As the intensity of the measured PL signal says little about the measurement (it relies on many experimental parameters, e.g. the used objective lens), the ODMR is shown using contrast C instead of intensity. The formula for contrast is given below:

$$C = \frac{-(I_{max} - I)}{I_{max}} * 100\% \quad (53)$$

In the above formula, I_{max} is the maximum value of the experimentally measured PL intensities. The minus sign is present to achieve a signal that looks qualitatively similar to the regular intensity signal. This is important as later on, in certain calculations, the visual properties of Rabi oscillations will be used. It will be seen on all figures using contrast data, that the baseline is never at $C = 0$. This is due to experimental noise, increasing I_{max} above (or decreasing I_{min} below) the fitted baseline.

To find the duration of the π-pulse (used in the pulsed ODMR protocol), the electronic Rabi protocol was performed first. The Rabi sequence [54] consists out of an initial laser pulse polarizing the NV center to state $|0\rangle_e$ after which a microwave field is applied for a variable time τ. This sequence is repeated for some time with the same MW power and frequency, while increasing τ from zero to some value τ_F. The laser pulse starting the second iteration is also the readout laser pulse of the first iteration and so on. The influence of the MW field on the NV center is mostly due to the magnetic component, which can be written as:

$$\boldsymbol{B}_{MW}(t) \quad = \quad \boldsymbol{B}_{MW} \cdot cos(2\pi f t) \quad (55)$$

This field addresses the spin operation on the transition $|0\rangle \leftrightarrow |\pm 1\rangle$ with a transition frequency of $\omega_0 = D - \gamma B_{NV}$. The resonance condition $2\pi f = \omega_0$ can be fulfilled by adjusting B_{NV} and should be kept in all iterations of the sequence. The component of $\boldsymbol{B}_{MW}$ perpendicular to S_z can be seen as the sum of two circularly polarized fields, rotating in the opposite sense. The left-hand rotating field B_1 directly drives the spin rotation and in this reference frame the approximate electronic Hamiltonian (without hyperfine and quadrupole interactions) can be written as $H = \gamma B_1 S_x$. This results in the spin state oscillating between $|0\rangle$ and $|-1\rangle$ with Rabi frequency $\Omega_R = \gamma B_1$. In the Bloch sphere representation, the spin state vector rotates around B_1 by an angle $\theta = 2\pi\gamma B_1 \tau$ after a time τ. The NV center photoluminescence will vary sinusoidally with the Rabi frequency while the spin state vector rotates in the Bloch sphere. A successful demonstration of Rabi oscillations means that coherent control has been achieved [55]. The resulting signal can then be used to determine the duration of π-pulses. The measurement in figure 18 reveals a π-pulse of $\sim$ 800 ns.

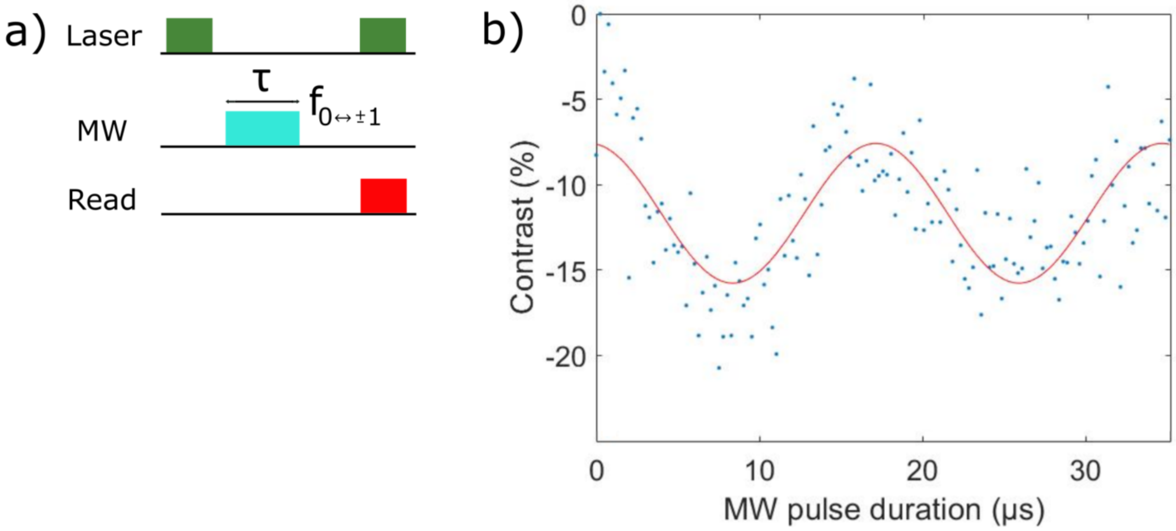

Figure 18: Electronic Rabi oscillations of the NV center. a) Electron Rabi protocol. b) PL spectrum measured in an electron Rabi experiment.

7.1.2 Nuclear spin

In the previous section, it became clear that to manipulate the electronic spin of an NV center, microwave magnetic fields need to be applied during times on the order of hundreds of nanoseconds. For ^{14}N nuclear spins one has to apply RF magnetic fields on timescales of tens of microseconds [5]. The manipulation of nuclear spin states is also more difficult than its electronic counterpart because the nuclei lack the optical polarization mechanism and easy read-out of the electrons. Therefore, the electronic spin will be used to manipulate the nuclear spin state, by applying narrowband nuclear spin-state selective MW pulses, that flip the electron spin depending on the state of the nuclear spin. This operation is equivalent to a CNOT gate [53] and the resonance frequencies of the pulses can be found by inspection of the hyperfine peaks in pulsed ODMR measurements. Via ENDOR, the nuclear spin can also be read through the electron spin.

The first protocol to be addressed is the nuclear Rabi protocol (see fig. 19a)), which can be used to determine the duration of the nuclear π-pulse. It consists out of a first laser pulse that polarizes the electronic spin state to $|0\rangle_e$ and completely depolarizes the nuclear state (so that the probabilities of occupancy of a certain nuclear energy level are all equal to $1/3$). Then follows a MW π-pulse with a frequency corresponding to the transition between the $|0, 1\rangle$ state and the $|-1, 1\rangle$ state. An RF pulse of frequency 7.11 MHz and variable duration τ is then used to drive transitions between nuclear spin states $m_I = 1$ and $m_I = 0$. This resonance frequency can be calculated theoretically as the sum of the nuclear quadrupole splitting (4.95 MHz) and the hyperfine splitting (2.16 MHz), which is shown in figure 19b). The next laser pulse has a duration of 500 ns, chosen specifically to bring back the electronic spin to zero, while leaving the nuclear spin untouched. The exact duration of this pulse will be addressed later on. If there was any nuclear spin transfer during the RF pulse in the $|-1\rangle_e$ state, then this will remain present in the $|0\rangle_e$ state. The second MW π-pulse has the same frequency as the first one and is used to probe the probability of being in the $|0, 1\rangle$ state, which is approximately equivalent to the probability of having $m_I = 1$, as the electron spin is largely polarized to zero at this point. The last laser pulse is used to read out the photoluminescence coming from the NV center: this value will be high when the probability of being in $|0, 1\rangle$ is high and low in the other case. As the protocol starts with a depolarized nuclear spin, the PL at time zero defines the minimum value (all three hyperfine peaks are well visible). The maximum PL then indicates the duration of a π-pulse, which completely flips the $|1\rangle_N$ part of the nuclear spin to

$|0\rangle_N$ (the left hyperfine peak, corresponding to the $|0,1\rangle \leftrightarrow |-1,1\rangle$ transition, has less contrast or disappears completely). From figure 19c) it is clear that the nuclear π-pulse is $\sim 16.5\mu$s.

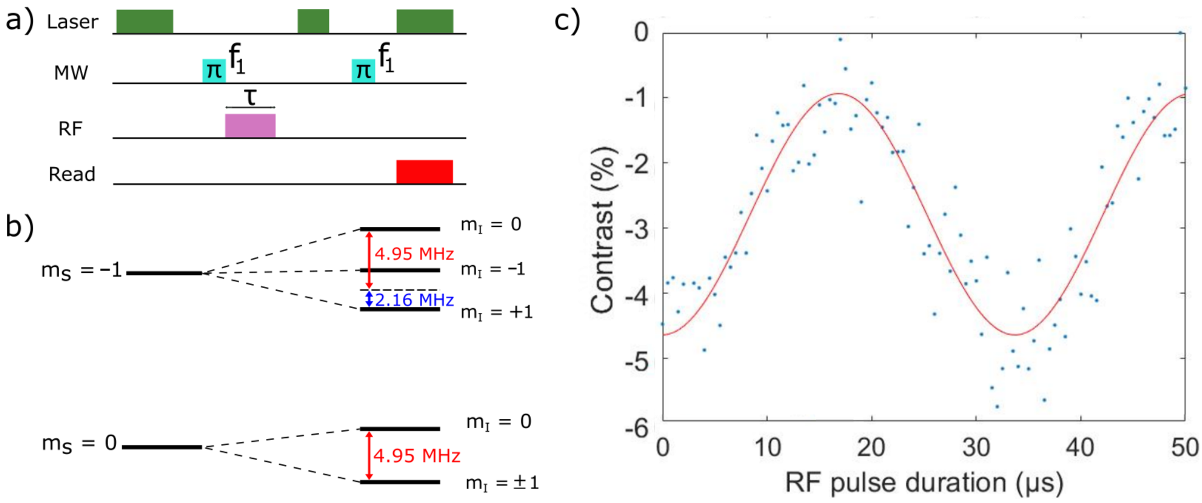

Figure 19: Nuclear Rabi measurement. a) Pulse protocol. MW frequency f_1 corresponds to the $|0,1\rangle \leftrightarrow |-1,1\rangle$. b) PL spectrum measured in a nuclear Rabi experiment.

Once the duration of the nuclear π-pulse is known, the resonance frequency can be verified using nuclear ODMR. In addition, another manipulation of the nuclear spin based on the quadrupole splitting was checked. This reveals a resonance frequency of ~ 4.95 MHz, also in line with theoretical calculations [25]. The nuclear ODMR protocol looks similar to the electron ODMR explained earlier, but now the RF frequency is sweeped instead of the MW frequency. This is depicted in figure 20a). The MW π-pulse frequency is set to the resonance frequency of the $|0,1\rangle \leftrightarrow |-1,1\rangle$ transition in both experiments.

As stated, two different transitions will be investigated here. The first one is the transition between $|-1,1\rangle$ and $|-1,0\rangle$. In the pulse protocol used for this transition, the first MW pulse brings the population of $|0,1\rangle$ to $|-1,1\rangle$. Then the RF pulse is swept around the transition $|-1,1\rangle \rightarrow |-1,0\rangle$. The following laser pulse repolarizes the electronic spin to zero, but does not alter the nuclear spin. The next MW π-pulse is used to probe the population of the $|0,1\rangle$ energy level. Therefore, when the RF pulse is on-resonance, population is transferred from $|0,1\rangle$ to $|0,0\rangle$, lowering the population in the $|0,1\rangle$ state. However as before, a low population corresponds to a high PL signal, so a resonance peak is seen in the RF frequency spectrum. Using a Lorentzian fit of the data as seen in figure 20 a resonance frequency of 7.104 MHz was

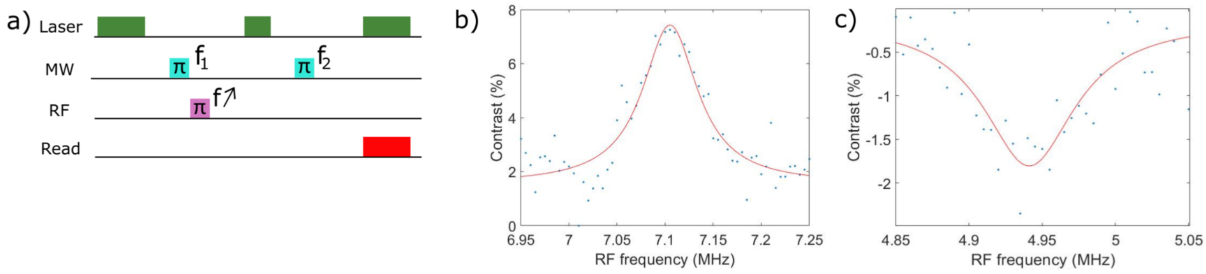

Figure 20: Nuclear ODMR measurement. a) Pulse protocol. Frequency f_1 corresponds to the $|0,1\rangle \leftrightarrow |-1,1\rangle$ in both measurements. Frequency f_2 also corresponds to the $|0,1\rangle \leftrightarrow |-1,1\rangle$ transition, but this does not necessarily need to be so. For example the $|0,0\rangle \leftrightarrow |-1,0\rangle$ transition could also be chosen and this would invert contrast. b) PL spectrum measured in a nuclear ODMR experiment centered at the $|-1,1\rangle \leftrightarrow |-1,0\rangle$ transition. c) PL spectrum measured in a nuclear ODMR experiment centered at the $|0,0\rangle \leftrightarrow |0,1\rangle$ transition.

found. This is not far away from the original guess of 7.11 MHz and given the large linewidth (0.32 MHz) of the resonance the theoretically predicted value still drives the transition efficiently. Note that for this measurement the contrast (see formula (54)) was determined using the minimum value of the PL intensity I_{min} instead of I_{max} and the minus sign was dropped. The reason for this is that the PL intensity was seen to rise with respect to the baseline at this resonance frequency, whereas other resonances dropped with respect to the baseline. Therefore, I_{min} technically fulfills the role of I_{max} in this situation.

The second measurement investigates the transition between $|0,0\rangle$ and $|0,1\rangle$. These energy levels are splitted only due to the nuclear quadrupole effect (m_I = 0 and m_I = ± 1) and very slightly by the nuclear Zeeman effect ($m_I = 1$ and $m_I = -1$). As the first MW π-pulse induces a transition between the $|0,1\rangle$ and $|-1,1\rangle$ states, the first state becomes vacant. Therefore an RF pulse with the correct frequency can induce a transition from the $|0,0\rangle$ state to the $|0,1\rangle$ state. This increases the population of the $|0,1\rangle$ state, so that the PL signal decreases at the resonance frequency and a dip is seen in the RF frequency spectrum.

Once the RF pulse duration (16.5μs) and frequency (7.11 MHz) are known, they can be used in other protocols designed to manipulate the nuclear spin, collectively known as QNMR protocols. QNMR stands for Quantum Nuclear Magnetic Resonance and describes any protocol that measures nuclear resonance frequencies. In this thesis, the nuclear Rabi and nuclear ODMR are QNMR protocols. Another QNMR protocol is used to polarize the nuclear spin, either partially or fully. The pulse sequence for partial polarization can be seen in figure 21a) and 21b) shows the resulting PL spectrum. First a MW π-pulse is used to excite the $|0,1\rangle \rightarrow |-1,1\rangle$ transition, after which an RF π-pulse excites this state further to $|-1,0\rangle$. Then a short laser pulse is used to bring the electronic state back to zero, after which pulsed ODMR is used for the readout. In comparison to the regular pulsed ODMR measurement depicted in figure 17, it is clear that the left hyperfine peak is much smaller. As this peak corresponds to the $|0,1\rangle \rightarrow |-1,1\rangle$ transition, it proves that the nuclear spin has been partially polarized from $|1\rangle_N$ to $|0\rangle_N$. In the ideal case, all population from $|1\rangle_N$ would be transferred to $|0\rangle_N$, creating a mixed state with a probability of $2/3$ to be in state $m_I = 0$ and $1/3$ to be in state $m_I = -1$. As could be seen that the population transfer is not complete, the probability to find the system in a state $m_I = 0$ will be slightly lower than $2/3$ since there is some residual probability to find the system in state $m_I = 1$. This pulse protocol was also suggested for the spin initialization in the NV-based Otto cycle. However, to create thermal states of choice, the rate of laser-induced population transfer must be better characterized.

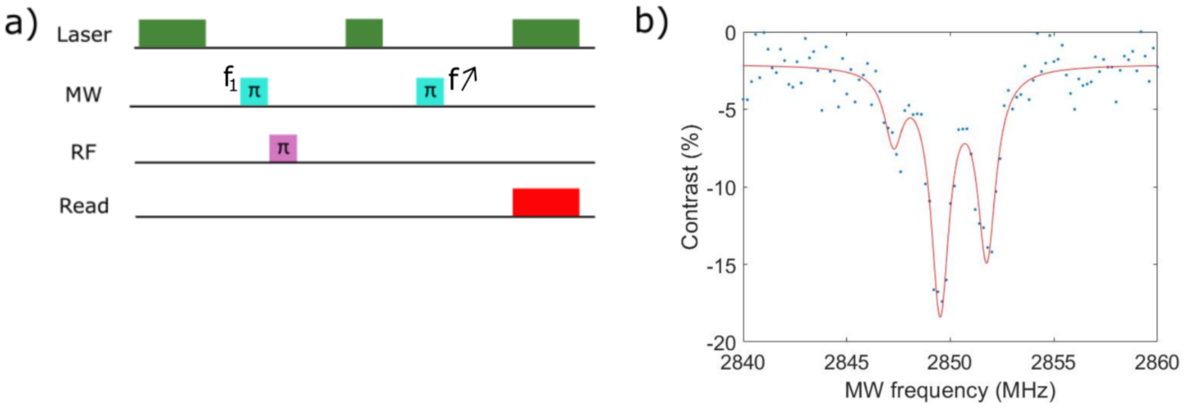

Figure 21: Partial polarization of the nuclear spin. a) Pulse protocol. b) PL spectrum showing the depletion of the $|0,1\rangle$ state (left hyperfine peak).

To achieve a full nuclear polarization, the $m_I = -1$ spin must also be flipped to zero. This can be done by inserting a second pair of consecutive MW and RF π-pulses as was done by Chakraborty et al. [25]. However, since the nuclear ODMR measurement (see figure 20) showed broad resonances, a single RF pulse can be used to excite both the $|-1,1\rangle \rightarrow |-1,0\rangle$

transition and the $|1,-1\rangle \rightarrow |1,0\rangle$ transition. It is important for the second transition to be performed with $m_s = 1$ instead of -1 as in the first one, to achieve two-level system transitions. Should this not be the case, the RF pulse would excite both the $|-1,1\rangle$ and the $|-1,1\rangle$ state to the $|-1,0\rangle$ state. This would generate three-level system dynamics, which is more difficult to interpret. Therefore, the NV center under consideration is always placed inside an ambient magnetic field, splitting the ZFS resonance and providing two two-level systems to manipulate nuclear spins. The complete protocol used for a full polarization can be seen in figure 22a). The first MW π-pulse is at the resonance frequency of $|-1,1\rangle \rightarrow |-1,0\rangle$ and the second one at the resonance frequency of $|1,-1\rangle \rightarrow |1,0\rangle$. The RF pulse has a frequency of 7.11 MHz and polarizes both nuclear spins to m_I = 0. The resulting PL spectrum is plotted in figure 22b). It can be seen that only the central peak, corresponding to the $|0,0\rangle \leftrightarrow |-1,0\rangle$ transition remains, proving that the spin system has been fully polarized to $|0,0\rangle$. Note that if the other two resonance peaks would have disappeared completely, the system would be in the pure state $|0,0\rangle$. This is not the case, meaning that a small population of $m_I = \pm 1$ energy levels remains. However, because this population is small, the system can still be assigned the pseudopure state $|0,0\rangle$ to good approximation, as is also done here.

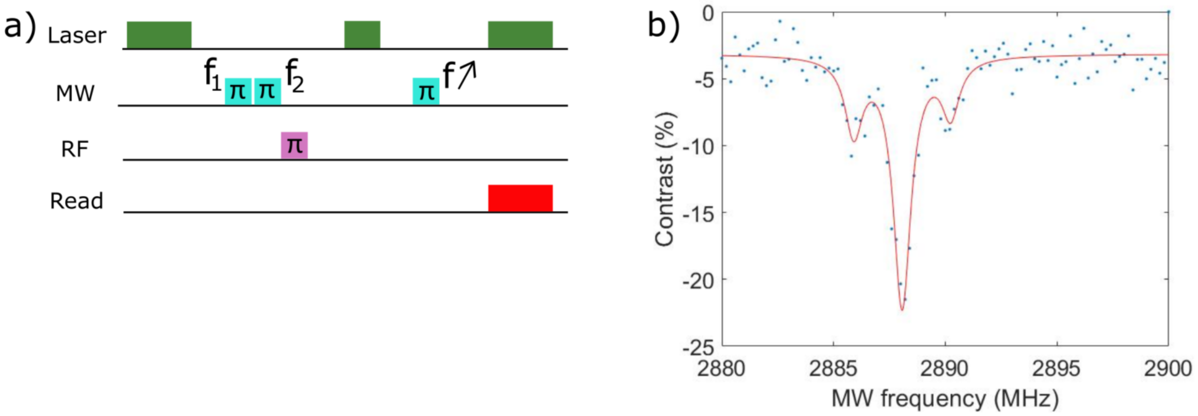

Figure 22: Full polarization of the nuclear spin. a) Pulse protocol. b) PL spectrum showing the depletion of the $|0,1\rangle$ state (left hyperfine peak) and $|0,-1\rangle$ state (right hyperfine peak).

This full polarization protocol can also be attached before the normal nuclear Rabi protocol to create Rabi oscillations with a larger contrast. As the system is polarized each time to the $|0,0\rangle$ state before driving the Rabi oscillations, the resulting signal will show approximately three times as much contrast, since three hyperfine peaks are now concentrated into one. The resulting protocol can be seen in figure 23, together with the measured signals. For the Rabi oscillations without initialization, the noise level is approximately 3% ($\sim$ 200 counts/ s in absolute intensity), which is of the same order of magnitude as the amplitude ($\sim$ 300 counts/ s). The maximum contrast of these oscillations is $\sim 3\%$. With initialization, the noise level is the same as before, but the oscillation amplitude is larger, giving a better maximum contrast of $\sim$ 6 $\%$. For a full polarization, one would expect a threefold increase in contrast since the population of $|0\rangle_N$ is increased approximately threefold in the initial polarization stage. However, it was seen that only an approximate polarization could be achieved, hence the smaller contrast increase.

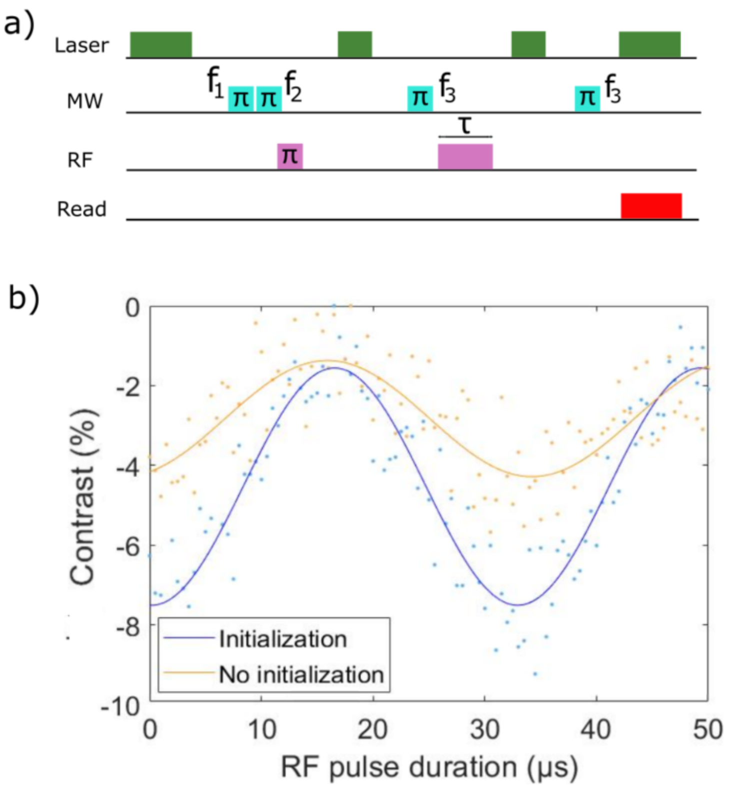

Figure 23: Nuclear Rabi measurement with intialization. a) Pulse protocol. b) PL spectrum showing Rabi oscillations of the nuclear spin in depolarized state (with the pulse sequence presented in figure 19) in orange and completely polarized to $m_I = 0$ in blue. The contrast of the Rabi oscillations of the polarized state is approximately twice the contrast of the depolarized Rabi oscillations.

7.1.3 Optimization of the pulse sequences

In order to achieve the best manipulation, which in turn generates the highest nuclear polarization, the pulse sequence must be optimized. The duration of the MW and RF π-pulses was determined using respectively electron and nuclear Rabi measurements. In this section, I have determined the optimal duration of laser pulses via parametric studies at 1 MW laser power. In addition, I have investigated and mitigated the negative effects of applying RF waves to the diamond sample.

Optimization of the laser pulse duration

In the pulse protocol for a full nuclear polarization depicted in figure 22a), three laser pulses can be distinguished. The first one is the initialization pulse and is taken to be 3000 ns long to ensure that the system starts out in a state with a polarized electronic spin $|0\rangle_e$ and a depolarized nuclear spin. The last laser pulse is used to read out the final system state and then initialize it back to the aforementioned starting state. In this sense, the first and last laser pulse are equivalent, which is why they have the same duration. The laser pulse in between serves a different purpose. It is used to repolarize only the electron spin that has been depolarized by the previous MW and RF pulses, without changing the nuclear spin. More specifically, the laser pulse should be long enough to repolarize the electron spin to zero, but at the same time short enough to prevent depolarization of the nuclear spin. The loss of nuclear spin polarization during laser excitation has multiple origins [25]. First, the ground and excited state of the NV center have different energy eigenstates, so that the laser excitation projects nuclear spin eigenstates corresponding to the electronic ground state onto superpositions of those nuclear spin states in the excited state. Furthermore, as the laser pulse duration increases, so does the probability of NV^- to NV^0 charge conversion somewhere during this pulse. The neutral NV complex has different hyperfine couplings and nuclear quadrupole interactions, resulting in a different energy splitting between the nuclear spin eigenstates. Lastly, the spin-lattice relaxation time T_1 is shorter for the neutral NV center, resulting in an increased loss of spin polarization.

To determine the optimal duration of the laser pulse, an alternate version of the half polarization QNMR protocol is used in which no RF pulse is being applied (see fig. 24) so that after the electron spin is changed to $|-1\rangle_e$, there is no change in nuclear spin state. Therefore, the second laser pulse should restore the initial state of electron polarization and nuclear depolarization. If this is not the case, it means that the laser pulse was not long enough to polarize the system back from $|-1,1\rangle$ to $|0,1\rangle$, which leaves only $|0,0\rangle$ and $|0,-1\rangle$ to be detected. This is tested for increasing laser pulse durations, demonstrating that a pulse of 500 ns is sufficient to reach the electronic ground state again. The pulse protocol and the results of a few of these measurements (with laser pulse durations ranging from 100 ns to 1000 ns) are depicted in figure 25. For all these measurements, the laser power was equal to 1 mW.

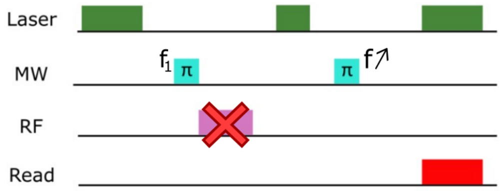

Figure 24: First pulse protocol for the parametric study of laser pulse duration.

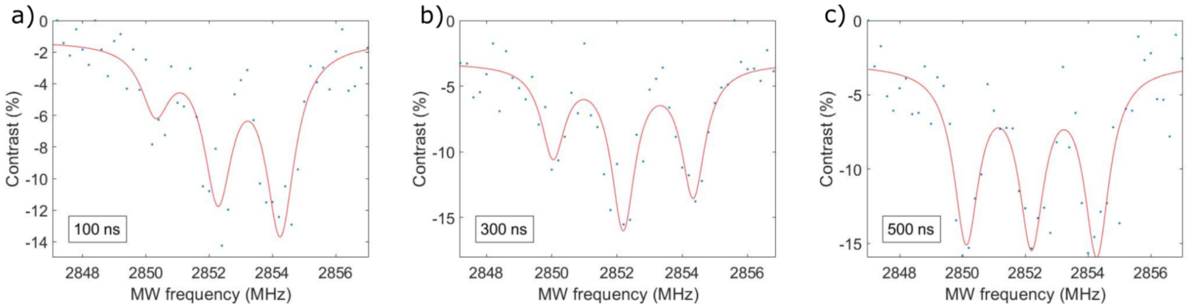

Figure 25: First parametric study of laser pulse duration. a) Result for 100 ns laser pulse. b) Result for 300 ns laser pulse. c) Result for 500 ns laser pulse.

I investigate the effect of the laser pulse duration on the electronic spin using an alternative pulse sequence without RF application (without nuclear polarization) because it makes it easier to detect changes in population. In principle, the ineffective polarization of the electronic spin to the ground state at low laser pulse durations could also be seen when the nuclear spin is polarized to $|0\rangle_N$. When doing so, the depth of the $|0,0\rangle \leftrightarrow |-1,0\rangle$ hyperfine peak would have to be compared for different laser pulse durations. Once it reaches maximum depth, then the electron spin is fully polarized to zero. However, this method is not optimal as there are other factors affecting peak depth as well, for example how well the NV center is kept in focus during the measurement (sample drift). To eliminate those factors, it's better to have all three peaks present in the signal, so that the relative peak depths can be investigated. Here, the only difference in peak depth between the resonances comes from a population difference.

A laser pulse of 500 ns is just long enough to polarize the electronic spin to $|0\rangle_e$, so the pulse needs to be at least this long. Besides polarizing the electronic spin, laser pulses also depolarize the nuclear spin [25]. This can be seen by repeating the parametric study for a system in the state $|0, 0\rangle$, which means that this time the regular full polarization protocol is used with the RF π-pulse present. The results for a few of these measurements are presented in figure 26. It is clear that if the laser pulses become longer, the nuclear polarization is lost. The measurement at 500 ns shows a significant amount of nuclear polarization, which is why this duration is chosen for the laser pulse used to repolarize the electron spin after excitation. At 3000 ns, which is the duration of the initializing laser pulse presented here, almost all polarization has disappeared. This means that each measurement starts with a practically depolarized nuclear spin. In literature [25] an optimal duration of $\sim$ 5000 ns was found to create a full nuclear depolarization using a laser power of $\sim$ 150μW at the sample, which is much less than the laser power of 1 mW used in the experiments presented here. Therefore, it is interesting to investigate also the optimal duration of this first initializing laser pulse and compare the results at a lower laser power.

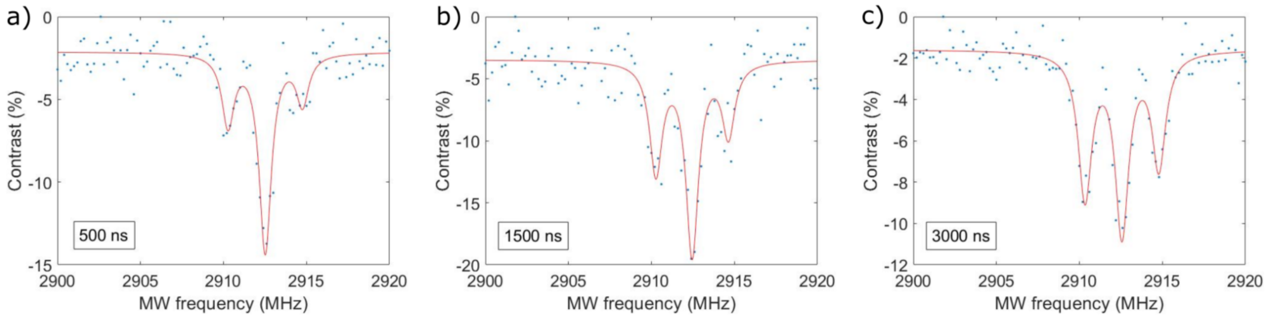

Figure 26: Parametric study of laser pulse duration for a spin-polarized NV center. a) Result for 500 ns laser pulse. b) Result for 1500 ns laser pulse. c) Result for 3000 ns laser pulse.

Effect of RF pulse duration on the sample and the resonances

Applying RF pulses is seen to affect the location of the sample in both the directions parallel and perpendicular to the diamond plane. Furthermore, the resonance frequencies of the system change under RF application. As all hyperfine resonances move together in the same direction (to lower frequencies), the shift is proven to be a shift in ZFS. The approximate Hamiltonian presented in formula (3) cannot explain this behavior and the current hypothesis is that it is linked to heating of the sample. The resulting sample drift and frequency shift depend on which sample stage is used. This may be because the second sample holder allows for more movement, since it had been installed more recently and the sample needs some time to properly set. Figure 27 illustrates this behavior for the first sample holder. It can also be seen that for the application of an RF π-pulse, the left hyperfine peak is depopulated. This is because these measurements were performed using the partial polarization protocol as seen in figure 21.

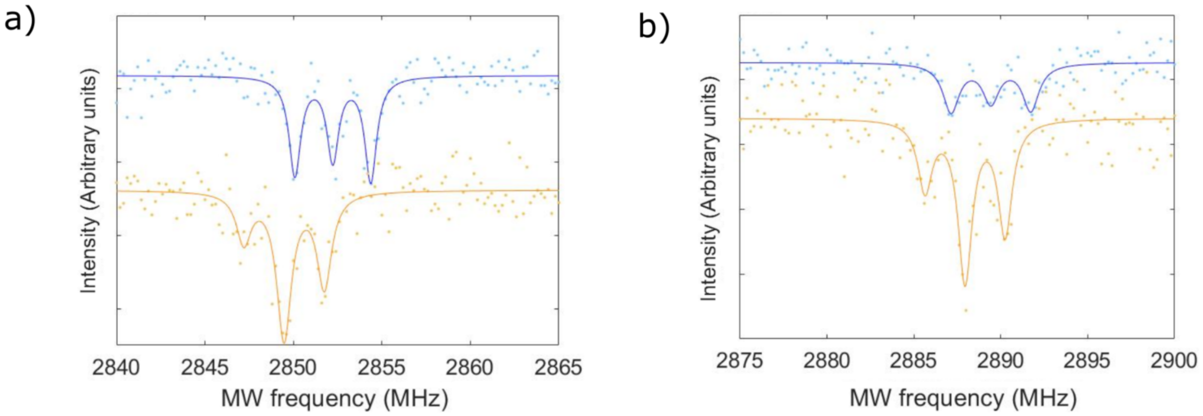

Figure 27: Effect of RF application on resonance frequencies. Intensity is plotted in arbitrary units so that both the blue and orange data points can be plotted on the same graph. Only relative peak depths and frequency shifts are important. The blue data points show the result of a regular pulsed ODMR measurement. All three hyperfine peaks have approximately equal contrast. The orange data points show the result of a QNMR measurement were RF waves are applied. It can be seen that they induce a transition from $|1\rangle_N$ to $|0\rangle_N$, as the relative depths of the hyperfine peaks changes, and that they also induce a frequency shift. a) Left hyperfine peaks. b) Right hyperfine peaks.

In order to correct for this unforeseen behavior, two steps are taken. First, to correct for sample drift a *target lock* functionality is implemented in the software. To use this functionality, one has to put the NV center of interest in the laser focus manually and then enable the target lock. This saves the current amount of measured photons and compares the counts at each point in time to this reference value. If the counts change by a significant amount (in this case 50% of the original value), the laser scans around the previous focus point and moves into the direction where the measured counts are closest to the reference counts. This is repeated until the difference is once again smaller than the threshold, indicating that the NV center is back in focus. Secondly, to correct for the frequency shift, alternative pulse protocols have been designed where the RF and MW frequencies are varied at the same time. For example, a microwave frequency sweep experiment can be performed while applying an off-resonant RF field in the background. The resulting PL spectrum will then look like a pulsed ODMR measurement, but with resonance frequencies influenced by the RF waves. This means that for every pulse protocol including RF pulses, two or three measurements must be performed: one or two (depending on the protocol, one could need resonance frequencies of one or two Zeeman peaks) with an MW frequency sweep to determine the resonance frequencies and then another one without that uses the correct frequencies.

7.2 Quantum Tomography of the nuclear spin state

Now that the necessary tools to manipulate the nuclear spin are in hand, quantum state tomography measurements can be performed. The validity of this technique must be checked using known nuclear spin states, before it can be used to determine unknown nuclear spin states. The protocol used for QST of a known state can be seen in figure 28. It blends the process of creating a nuclear state and then determining it, and is identical to the protocol used for measuring initialized nuclear spin Rabi oscillations (see fig. 23) apart from two things. First, there is an additional RF pulse with duration T_{RF} after the third MW pulse. Secondly the RF pulses with duration τ (the ones that drive Rabi oscillations) now have a definite phase. To see the effect of these alterations, go through all the steps of the pulse protocol. They can be divided in an initialization stage, a Rabi driving stage and a readout stage. The initialization stage consists of the first seven pulses (and technically the phase of the Rabi driving RF pulse). The system is brought to the $|0, 0\rangle$ state by the first five pulses (laser - MW - MW - RF - laser) and then the nuclear state can be altered from here to any generic state $|\psi\rangle_N$. To do so, the system is brought first to $|-1, 0\rangle$ and then an RF pulse of duration T_{RF} is used to rotate the $|0\rangle_N$ state over an angle $\theta_N = \pi\frac{T_{RF}}{T_\pi}$ around the x-axis, where T_π is the RF pulse duration of a π-pulse. Note that this also changes ϕ_N, because the rotation around the x-axis tilts $|\psi\rangle_N$ towards the negative y-axis ($\phi_N = 270°$). Alternatively, if one defines the natural rotation axis of Rabi oscillations as the positive y-axis, then ϕ_N would remain zero. This is an easier viewpoint, but would require different measurement parameters, so I have decided to keep the current viewpoint.

The initialization stage and Rabi driving stage intersect slightly, because (apart from the aforementioned offset) ϕ_N is controlled via the phase in the Rabi driving stage. When the phase difference between these two RF pulses is zero, that would mean that the second one would start with the ending phase of the first one. This means that the Rabi oscillations are still driven around the x-axis, so that the starting state $|\psi\rangle_N$ is still defined by $(\theta_N = \frac{T_{RF}}{T_\pi}180°, \phi_N = 270°)$. If now a phase difference $\Delta\phi \neq 0$ is added to this second RF pulse, then the rotations of the Bloch vector $|\psi\rangle_N$ are no longer driven around the x-axis but around an axis that makes an angle $\Delta\phi$ with the x-axis. Alternatively, one could state that the Bloch vector does rotate around the x-axis defined by $\phi_N = 0$ but that $|\psi\rangle_N$ itself has acquired a phase $-\Delta\phi$ with respect to the negative y-axis. This second viewpoint will be adopted here, so that in this way any generic state $|\psi\rangle_N$ can be created with any (θ_N, ϕ_N). After driving Rabi oscillations of this state, the fluorescence is read out in the readout stage consisting of the last three pulses (laser - MW - laser). As before the MW pulses have a frequency corresponding to the $|0,1\rangle \leftrightarrow |-1,1\rangle$, $|0,-1\rangle \leftrightarrow |-1,-1\rangle$ and $|0,0\rangle \leftrightarrow |-1,0\rangle$ (twice) transitions.

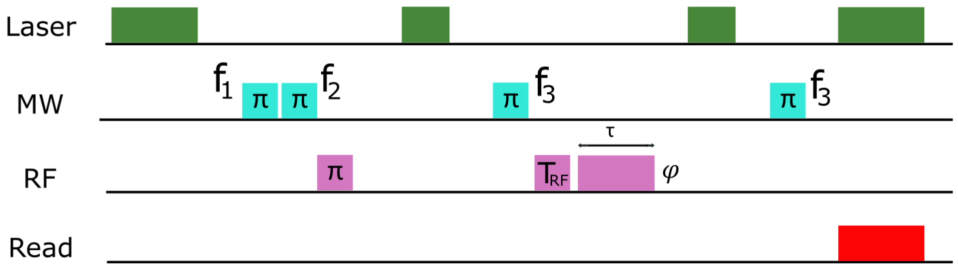

Figure 28: Pulse protocol used to prepare the nuclear spin qubit in an arbitrary state $|\psi\rangle_N = cos(\frac{\theta_N}{2}) + e^{i\phi}sin(\frac{\theta_N}{2})$ and subsequent tomography of this state. T_RF is used to control θ_N and ϕ is used to control ϕ_N.

It was stated before that three Rabi measurements were necessary for QST: a reference Rabi, an x-Rabi (rotation of the Bloch vector around the x-axis) and a y-Rabi (rotation of the Bloch vector around the y-axis). It was explained in the previous paragraph how an x-Rabi can be performed on a state $|\psi\rangle_N$ characterized by the angles θ_N and ϕ_N. However, a rotation of this vector around the y-axis must also be driven. The selection of the rotation axis also happens through the phase of the MW/ RF field. If phase $0°$ corresponds to the positive x-axis, then phase $90°$ corresponds to the positive y-axis. This means that to create a state with phase $270° - \phi_N$ the x-Rabi measurement must be performed with phase ϕ_N and the y-Rabi measurement must be performed with phase $90^\circ + \phi_N$. Therefore in the x-Rabi measurement the RF pulses are in phase with $|\psi\rangle_N$, whereas in the y-Rabi measurement the RF pulses are 90 degrees out of phase.

The described QST protocol will be tested using three different nuclear spin states. First, two random states are measured to check whether the QST technique works and if the results are reproducible. Then, a state very close to the negative y-axis on the Bloch sphere is measured to test the limits of operation. For each state, at least two full QST measurements have been performed, allowing to check the validity of the results. The results of all these measurements are summarized in table 1 at the end of this section. Furthermore, using 95% confidence intervals of the fit parameters, the QST calculations are repeated using the 'worst' combination of fit parameters within these intervals. This gives more insight in how robust the technique is. Lastly, it will be seen that the used protocols, specifically the AQST, are susceptible to sample drift which degrades their fidelity. This negative effect can be mitigated both during and after the measurements. For example, the three Rabi measurements are taken directly after each other using the target lock function of the software to compensate as much as possible for the sample drift over time. Because of the change in sample drift and resonance frequencies with the amount of RF waves applied, the reference measurement is also performed in presence of the same T_{RF}-pulse that is used in the x-Rabi and y-Rabi measurements, but off-resonance (9.11 MHz). This way, each measurement applies the same amount of RF waves to the diamond sample, so that equal measurement conditions are achieved. After the measurements one can perform the QST calculations on the contrast amplitude of Rabi oscillations instead of their intensity amplitude. To do so, the contrast C of the Rabi oscillations is calculated using formula (53). When the sample drift lowers the overall intensity of the measured NV photoluminescence (because the center moves out of the laser focus), the contrast is unchanged. Therefore the effects of sample drift are partially removed from the resulting AQST calculations. For PQST, this is not the case and the results and fidelities of PQST are invariant under this transformation, because phase angles α and β do not change. The PQST calculations will always be performed using regular intensity data (as is measured in the experiment). The AQST calculations will be performed both for intensity and contrast data, after which the results can be compared.

As a concluding remark, note that the described pulse protocol for determination of a known nuclear state can be easily adapted to perform QST of unknown nuclear states. For this, the state preparation is no longer needed: the RF pulse with duration T_RF can be omitted and the phases of the RF pulses of duration τ can be adapted to 0° for an x-Rabi and 90° for an y-Rabi. The calculations performed on the measured data remain the same for both AQST and PQST.

7.2.1 QST of the state (θ_N = $58.41°$, ϕ_N = $249°$)

First, the AQST protocol is tested using the generic state $|\psi\rangle_N = cos(\frac{\theta_N}{2})|0\rangle_N + e^{i\phi_N}sin(\frac{\theta_N}{2})$ with θ_N = $58.41°$ and ϕ_N = $249°$. This state has the following density operator ρ_t, which was calculated using MatLab:

$$\rho_t = \frac{1}{2}\begin{pmatrix} 1.5238 & -0.3053+0.7952i \\ -0.3053-0.7952i & 0.4762 \end{pmatrix}$$

When determining the density operator of the system using QST, this is the ideal result. In figure 29 the used results of Rabi measurements as reference and in the x- and y-direction are given. To create the desired state, T_{RF} was taken equal to $T_\pi * \frac{58.41°}{180°}$ creating a 58.41 degree pulse. The phases of the x-Rabi and y-Rabi were taken to be 21 and 111 degrees.

Amplitude quantum state tomography

Using the intensity measurements presented above (first row), the values for x^2, y^2 and z^2 (the coordinates of the nuclear spin Bloch vector) can be determined. Each Rabi signal is fitted with a function of the form $c + A^2 sin^2(\omega t + \phi)$ using MatLab, where the fit parameters are estimated starting from given guessed values. The amplitude of a Rabi measurement is equal to $\frac{A^2}{2}$ and by looking at the 95% confidence interval one can see how good the estimation is. From the Matlab fits follow A_R $=$ 339.3013 counts/ s, A_x $=$ 316.5128 counts/ s and A_y $=$ 248.6450 counts/ s, generating x^2, y^2 and z^2:

$$\begin{aligned} x^2 &= 1-(\tfrac{A_x}{A_R})^2 &&= 0.1298 \\ y^2 &= 1-(\tfrac{A_y}{A_R})^2 &&= 0.4630 \\ z^2 &= \tfrac{A_x^2+A_y^2}{A_R^2}-1 &&= 0.4072 \end{aligned}$$

Using the rules for sign determination, x, y and z can be uniquely determined. Here, x is negative as the y-Rabi starts off in a decreasing trend, y is negative as the x-Rabi starts off in an increasing fashion, and z is positive as both the x- and y-Rabi start below their mean value.

$$\begin{aligned} x &= -0.3603 \\ y &= -0.6804 \\ z &= 0.6381 \end{aligned}$$

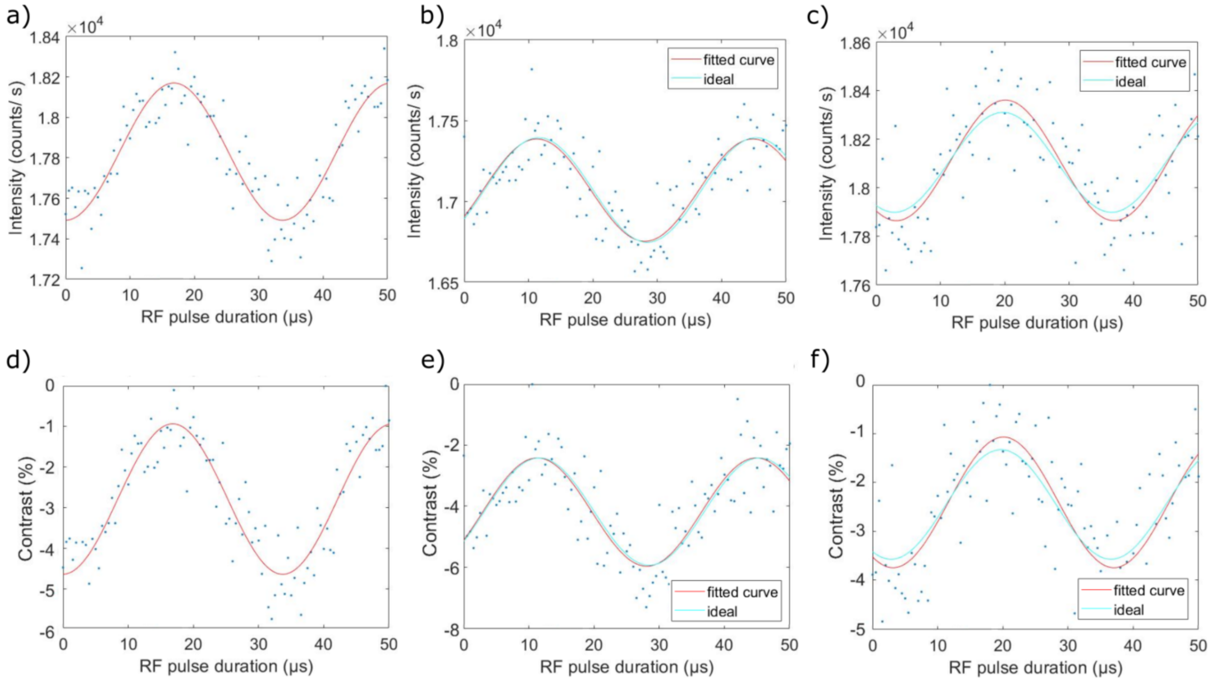

Figure 29: Nuclear tomography of the ($\theta_N = 58.41°, \phi_N = 249°$) state using intensity data in (a to c) and intensity contrast data (d to f). a) Intensity reference Rabi oscillations, measured with an off-resonance $58.41°$ pulse and zero phase difference. b) Intensity x-Rabi measured with an on-resonance $58.41°$ pulse and $21°$ phase difference. The match with the ideal case is nearly perfect. c) Intensity y-Rabi measured with an on-resonance $58.41°$ pulse and $111°$ phase difference. The match between the Rabi oscillations of the theoretical and experimental case is less good than for the x-Rabi. d) Contrast reference Rabi oscillations. e) Contrast x-Rabi oscillations. f) Contrast y-Rabi oscillations.

From these coordinates and formula 13, θ_N = 50.3479° and ϕ_N = 242.0980°. Because x is negative, an angle π had to be added to $tan^{-1}(y/x)$ to get the correct angle. Using these values, the experimentally recovered density operator $\rho_{e,A}$ can be determined:

$$\rho_{e,A} = \frac{1}{2}\begin{pmatrix} 1.6381 & -0.3603 + 0.6804i \\ -0.3603 - 0.6804i & 0.3619 \end{pmatrix}$$

Phase quantum state tomography

The described MatLab program also fits the phases of the Rabi oscillations. Using the phase angles of the x- and y-Rabi, one can determine the experimental density operator $\rho_{e,P}$ via PQST calculations. The x-phase α is found to be $59.0147°$ and the y-phase β is $-33.3519°$. Using the step by step plan presented in section 5.6.2, this gives $\theta_N = 60.8178°$ and $\phi_N = 248.4340°$.

The signs of α and β determine a 270° offset for ϕ and from inspection of the Rabi signals it is inferred that $\theta_N < 90^\circ$. This allows to determine $\rho_{e,P}$.

$$\rho_{e,P} = \frac{1}{2}\begin{pmatrix} 1.4876 & -0.3209 + 0.8120i \\ -0.3209 - 0.8120i & 0.5124 \end{pmatrix}$$

Discussion and verification of the results

The measured density operators both look quite similar to the ideal case ρ_t, which can also be showed graphically by plotting the real and imaginary values of the different density operators. This is depicted in figure 30.

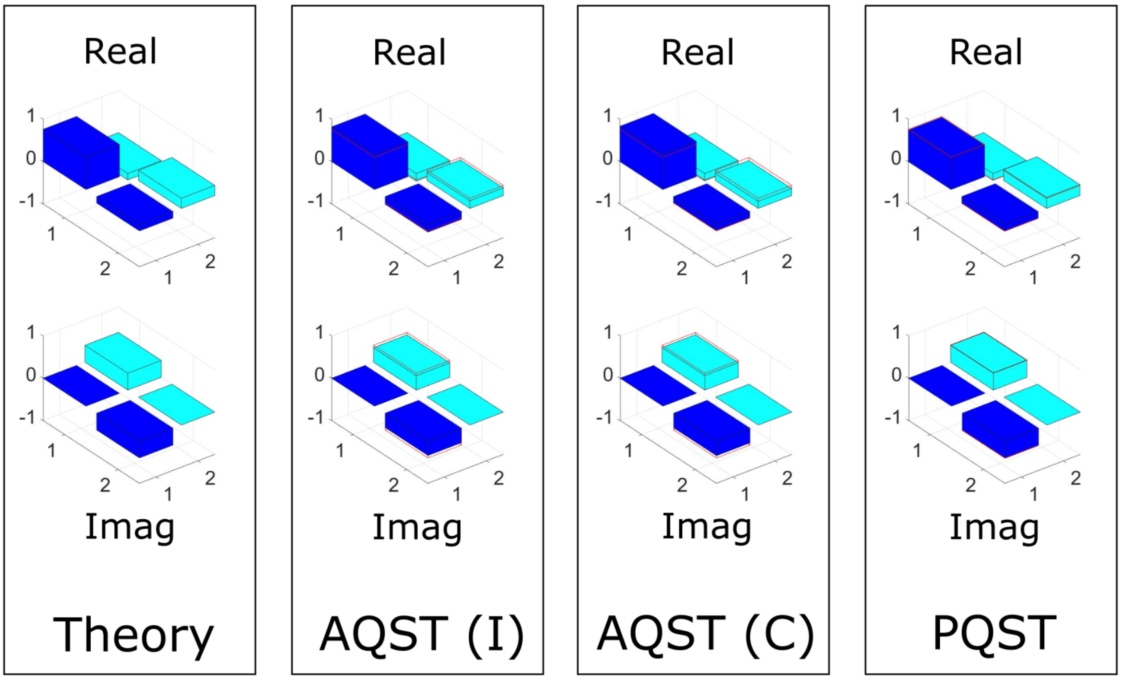

Figure 30: Comparison of the real and imaginary parts of the theoretical density operator (see ”Theory”) with the experimentally determined density operators. ”AQST (I)” shows the density operator calculated in amplitude tomography based on intensity data. ”AQST (C)” shows the density operator determined in amplitude tomography based on contrast data. Lastly, ”PQST” shows the density operator calculated in phase quantum state tomography. The red outline in the last three columns shows the theoretically expected values.

The fidelity F of the different density operators can be calculated using formula (18), given in section 5.6.3. Using the obtained density operators, a fidelity of 0.9927 is determined for the presented AQST measurement and a fidelity of 0.9995 is determined for the presented PQST. Alternatively, one can compare the Rabi oscillations expected for the theoretical (ideal) state (blue) with the measured Rabi oscillations (red). This can be seen also on figure 29. The oscillations are quite close together, indicating the correspondence between the created and measured state. For these ideal Rabi oscillations, the baselines were fitted using experimental data, the frequencies were calculated using T_π, the amplitudes using the reference measurement and the x and y coordinates of the ideal state and the phase angles using formulas (15) and (16), resulting in phases $\alpha = 56.62°$ of the x-Rabi and $\beta = -30.23°$ These values are close to the fitted phases of the experimental data.

To check the result, the 95% confidence intervals of the fit parameters can be inspected. Using these confidence intervals, one can determine what the 'worst case' fidelity would be for the presented measurement given the noise levels. These 'worst case' scenarios combine top and bottom limits of the confidence intervals to generate the worst possible fidelities. This is calculated for the QST presented in figure 29. The 'worst case' amplitude tomography gives angles: $\theta_N = 31.6542°$ and $\phi_N = 205.8829°$ and a fidelity of $F_A = 0.8861$. The 'worst case' phase tomography gives angles $\theta_N = 59.5791°$ and $\phi_N = 213.8623°$ and a fidelity of $F_P = 0.9330$.

Another way to verify the results obtained in this subsection, is to repeat the entire procedure (reference Rabi, x-Rabi and y-Rabi). These measurements were performed at a different time to allow for slightly different experimental conditions. AQST measurements gave the following angles: $\theta_N = 58.3851°$ and $\phi_N = 243.3618°$ resulting in a fidelity F_A of 0.9982. PQST measurements gave angles: $\theta_N = 58.9123°$ and $\phi_N = 254.185°$ resulting in a fidelity F_P of 0.9985.

Both of the QST measurements show good fidelities, which hints that sample drift was limited during these measurements. To verify this, AQST and PQST calculations can be repeated using the same measurement data, but adapted to contrast (see formula (53)) instead of the absolute intensity. This was illustrated for the first measurement in the second row of figure 29. Using these measurements the results of AQST are slightly altered, leading to new angles $\theta_N^C = 48.1344°$ and $\phi_N^C = 247.8780°$ and a new fidelity $F_A^C = 0.9919$ that can be compared with the previously calculated fidelity $F_A = 0.9927$. In this case, the low amount of sample drift already resulted in a good QST measurement, so that using the contrast cannot offer much improvement. In fact, in this case the fidelity slightly drops. For the second measurement of this state, the fidelity of the intensity contrast measurement is given by $F_A^C = 0.9985$ which is slightly higher than $F_A = 0.9982$.

Lastly, calculating the 'worst case' tomography using contrast data, the fidelity rises a little bit compared to the 'worst case' AQST fidelity determined two paragraphs ago. The results are $\theta_N^C = 33.4903°$, $\phi_N^C = 204.7013°$ and $F_A^C = 0.8866$. The 'worst case' PQST fidelity does not change upon using contrast data.

7.2.2 QST of the state (θ_N = $137.02°$, ϕ_N = $53°$)

In order to verify the reproducibility of the presented AQST and PQST method, it was tested on another generic state $|\psi\rangle$ with $\theta_N = 137.02°$ and ϕ_N = $53°$. The density operator of this state is given below:

$$\rho_t = \frac{1}{2}\begin{pmatrix} 0.2684 & 0.4103 - 0.5445i \\ 0.4103 + 0.5445i & 1.7316 \end{pmatrix}$$

The used pulse sequence and the resulting Rabi oscillations are shown in figure 31. To create $|\psi\rangle_N$, T_{RF} is taken to be $T_\pi * \frac{137.02°}{180°}$. The phases of the x-Rabi and y-Rabi were taken to be 217 and 307 degrees.

Amplitude quantum state tomography

During these measurements, sample drift was seen to be more pronounced. Because of this reason and to illustrate the methodology, the results in this section will be discussed using the contrast first, after which they are compared with the results obtained from intensity data. From the three Rabi signals in figure 31 (second row), the following amplitudes are found: $A_R = 2.093058\%$, $A_x = 2.0220605\%$ and $A_y = 1.7242245\%$. Both the x- and y-Rabi start off above their mean PL intensity, which means that z is negative. The x-Rabi starts off in a downward trend, which signifies that y is positive, and the y-Rabi starts off in an upward trend, which means that x is positive. This gives the following coordinates of $|\psi\rangle_N$:

$$\begin{aligned} x &= 0.2582634314 \\ y &= 0.5669215113 \\ z &= -0.7822403723 \end{aligned}$$

Similar to before one can calculate $\theta_N = 141.4678°$ and $\phi_N = 65.5091°$. Using these values, the experimentally recovered density operator $\rho_{e,A}$ can be determined:

$$\rho_{e,A} = \frac{1}{2}\begin{pmatrix} 0.2177 & 0.2582 - 0.5669i \\ 0.2582 + 0.5669i & 1.7823 \end{pmatrix}$$

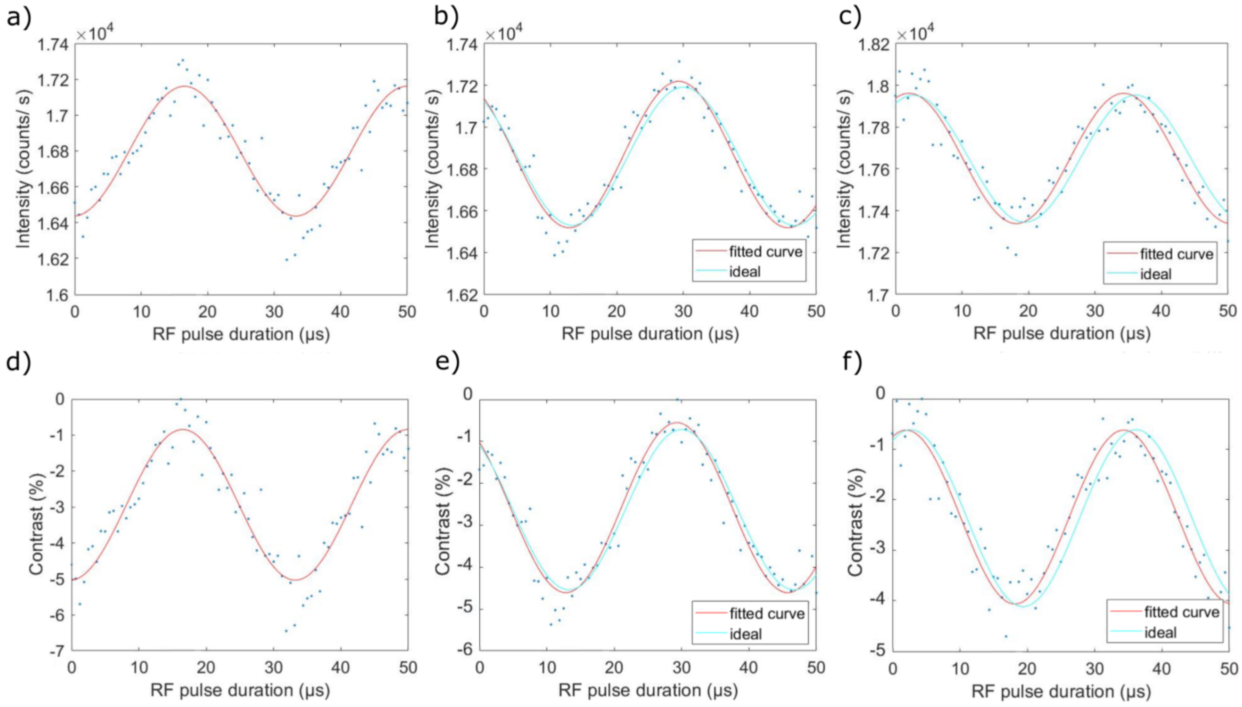

Figure 31: Nuclear tomography of the $(\theta_N = 137.02°, \phi_N = 53°)$ state using using intensity data in (a to c) and intensity contrast data (d to f). The duration of the π-pulse found in the reference measurement does not exactly match with the x- and y-Rabi. However, the initial phases and amplitudes match rather well. a) Intensity reference Rabi oscillations, measured with an off-resonance $137.02°$ pulse and $0°$ phase difference. b) Intensity x-Rabi measured with an on-resonance $137.02°$ pulse and $217°$ phase difference.c) Intensity y-Rabi measured with an on-resonance $137.02°$ pulse and $307°$ phase difference. d) Contrast reference Rabi oscillations. e) Contrast x-Rabi oscillations. f) Contrast y-Rabi oscillations.

Phase quantum state tomography

The x-phase α is found to be $-140.0881809°$ and the y-phase β is $157.2769148°$. As both angles are larger than 90 degrees in absolute value, the formulas (17) and (18) must be solved using $180° - |\alpha| = 39.9118191°$ and $180° - |\beta| = 22.72308524°$. From the signs of α and β it is clear that $\phi \in [0°, 90°]$ and thus an offset of 90 degrees is to be used. This gives θ_N = $136.9100°$ and ϕ_N = $63.4052°$, from which $\rho_{e,P}$ can be determined.

$$\rho_{e,P} = \frac{1}{2}\begin{pmatrix} 0.2697 & 0.3058 - 0.6109i \\ 0.3058 + 0.6109i & 1.7303 \end{pmatrix}$$

Discussion and verification of the results

As before, the experimentally obtained density operators are similar to the theoretical one. This is illustrated in figure 32.

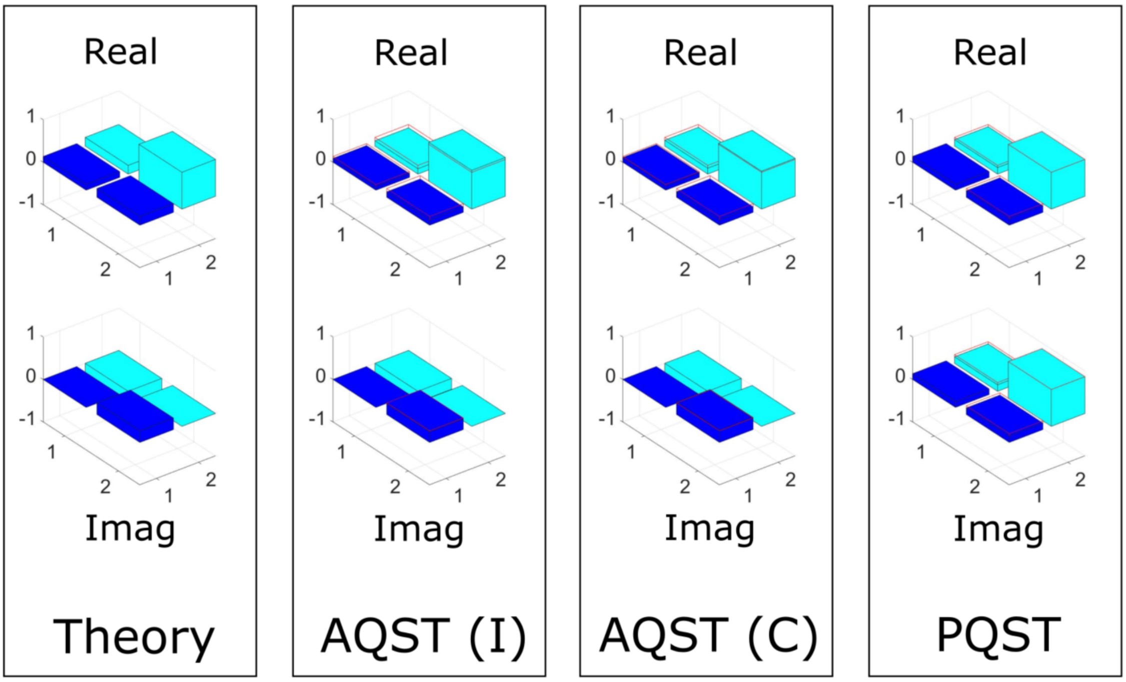

Figure 32: Comparison of the real and imaginary parts of the theoretical density operator with the experimentally determined density operators, using AQST on intensity and contrast data, and PQST.

Using these density operators, the fidelities of both measurements can be determined. The contrast AQST measurement has a fidelity of $F_A^C = 0.9935$ (compare with $F_A = 0.9914$) and the PQST measurement has a fidelity of 0.9962. On figure 31, the ideal Rabi oscillations expected for ρ_t were also plotted in blue over the experimental data. The frequency of the x- and especially the y-Rabi are slightly larger than the frequency of the reference Rabi. Because of this, the ideal Rabi oscillations (with the same frequency as the reference Rabi) look less similar to the experimental data. The separation between the ideal curves and the fitted Rabi signal is still within noise level and therefore the deviation of the reference frequency can be attributed to the fit itself. Using a larger RF pulse duration interval, this error might be corrected, as it allows to better fit the frequency.

The calculated fidelities can be compared with a ’worst case’ tomography as was done in the previous subsection. These calculations give AQST angles $\theta_N^C = 162.7402°$ and $\phi_N^C = 58.3218°$ resulting in a fidelity $F_A^C = 0.9500$ for contrast data and give $\theta_N = 168.0179°$, $\phi_N = 44.2536°$ and $F_A = 0.9278$ for intensity data. The ’worst case’ PQST calculations give $\theta_N = 132.6006°$

and $\phi_N = 77.6463°$ and a fidelity of $F_P = 0.9757$.

The entire QST measurement protocol (reference Rabi, x-Rabi, y-Rabi) was repeated two more times, to check the obtained results. The first repetition suffered most from sample drift and showed an AQST fidelity of $F_A^C = 0.9642$ (a significant improvement compared to the fidelity calculated using regular intensity data $F_A = 0.9004$) and a PQST fidelity of 0.9993, showing once again that PQST is less affected by sample drift than AQST. The second repetition showed an AQST fidelity of $F_A^C = 0.9969$ (compared to $F_A = 0.9876$) and a PQST fidelity of 0.9919.

7.2.3 QST of the state (θ_N = $87.6°$ and ϕ_N = $270°$)

For state vectors close to the axes, it's harder to perform QST using these Rabi-based protocols, especially for AQST. This has multiple reasons. For example, when $|\psi\rangle_N$ is aligned with the z-axis, this means that the reference Rabi, x-Rabi and y-Rabi all have the same (maximum) amplitude. Due to small measurement errors or sample drift, the x- or y-Rabi amplitude could become a bit larger than the reference Rabi, leading to complex coordinates in the calculation, which needs to be corrected. The same thing can happen when performing AQST on a state along the x- or y-axis. Here, either the x-Rabi or y-Rabi will have approximately the same amplitude as the reference Rabi and the other one will have zero amplitude. Apart from the fact that it is hard to measure this zero-amplitude Rabi (one has to wait a long time for noise to cancel out and to be sure that the amplitude really is zero), it is also hard to fit reliably because of the low signal-to-noise ratio (SNR). PQST also shares this problem. The lower the SNR, the harder it becomes to determine the phase correctly.

To test this limiting behavior, QST of the state (θ_N = $87.6°$, ϕ_N = $270°$) is performed. This state lies closely to the negative y-axis, but not exactly along it, so some y-Rabi oscillations should still be detectable. The density operator of this state is given below:

$$\rho_t = \frac{1}{2}\begin{pmatrix} 1.0419 & 0.9991i \\ -0.9991i & 0.9581 \end{pmatrix}$$

In figure 33 the results of the reference Rabi measurement and the Rabi measurements in the x- and y-direction are given for both the regular and contrast intensity data. To create the desired state, T_{RF} was taken equal to $\frac{87.6°}{180°}T_\pi$ creating a $87.6°$-pulse and the phases of the x-Rabi and

y-Rabi were taken to be 0 and 90 degrees.

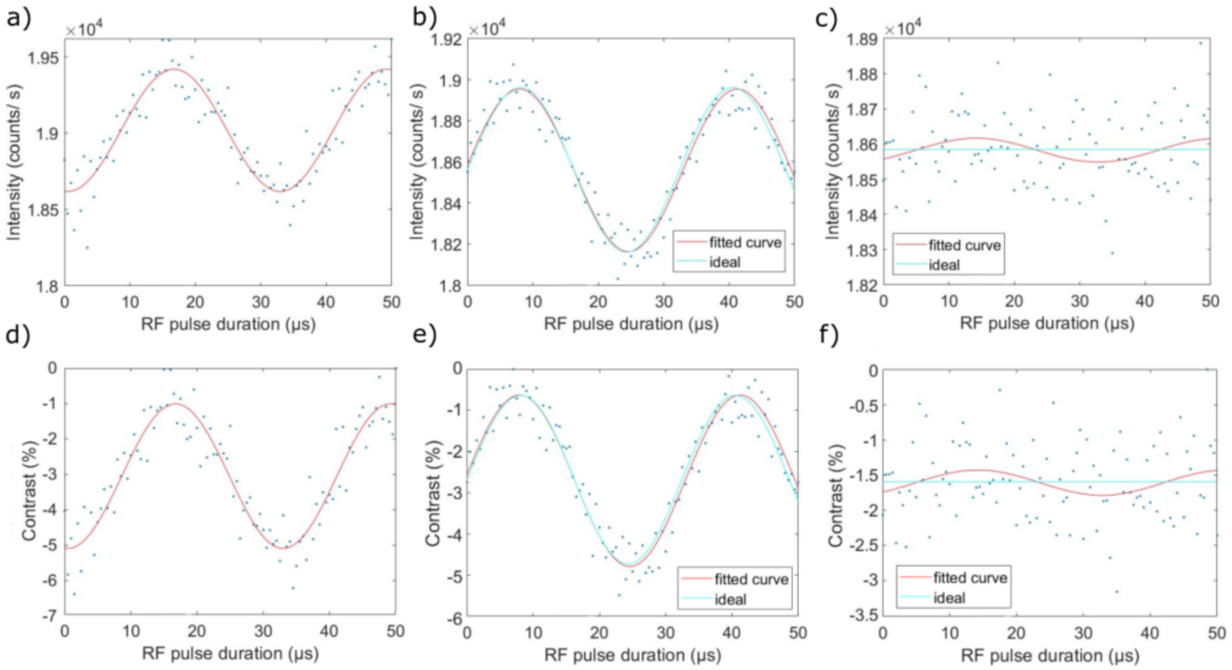

Figure 33: Nuclear tomography of the $(\theta_N = 87.6°, \phi_N = 270°)$ state using intensity data in (a to c) and intensity contrast data (d to f). a) Reference Rabi oscillations, measured with an off-resonance $87.6°$ pulse and zero phase difference. b) x-Rabi measured with an on-resonance $87.6°$ pulse and $0°$ phase difference. c) y-Rabi measured with an on-resonance $87.6°$ pulse and $90°$ phase difference. d) Contrast reference Rabi oscillations. e) Contrast x-Rabi oscillations. f) Contrast y-Rabi oscillations.

Amplitude quantum state tomography

Using the presented contrast measurements, the values for x^2, y^2 and z^2 can be determined. The amplitudes of the Rabi oscillations are $A_R = 2.042221\%$, $A_x = 2.074685\%$ and $A_y = 0.001788\%$. This gives for the coordinates of $|\psi\rangle_N$:

$$\begin{aligned} x^2 &= -0.0320455334 \\ y^2 &= 0.9999992335 \\ z^2 &= 0.0320463 \end{aligned}$$

It can be seen that, using these values, x would get a complex value. This is not possible of course, but can be overcome by taking $x = \sqrt{|x^2|}$. For small values of x this is a good approximation. Both the x- and y-Rabi start off in a increasing fashion, implying that x is positive and y is negative. Furthermore, the x-Rabi starts above its mean value (techically the first datapoint lies above, but it's better to look at the fit here) and the y-Rabi starts off below. Normally, this should not happen, but at this limiting case it is possible that there are slight deviations from this rule. As the y-Rabi is much weaker than the x-Rabi, the sign of z will be determined using the latter and is found to be negative. All of this leads to the following coordinates:

$$\begin{aligned} x &= 0.1790126627 \\ y &= -0.9999996167 \\ z &= -0.1790148038 \end{aligned}$$

Formula 13 then allows to calculate $\theta_N = 99.9937°$ and $\phi_N = 280.1492°$. An angle of 180° had to be added to θ_N and an angle of 360° to ϕ_N to get the correct results. In this way, the AQST density operator can be found:

$$\rho_{e,A} = \frac{1}{2}\begin{pmatrix} 0.8265 & 0.1735 + 0.9694i \\ 0.1735 - 0.9694i & 1.1735 \end{pmatrix}$$

Phase quantum state tomography

With PQST, the intensity data is fitted to find the phases of the x- and y-Rabi oscillations. This gives: $\alpha = 93.79319106°$ and $\beta = 42.19261203°$. Normally, it's not possible for α to be larger then 90 degrees when β is not, but as stated before this is a limiting case. As the y-Rabi has a much weaker signal than the x-Rabi, α is used to determine that θ_N is larger than 90 degrees. The step-by-step plan presented in section 4.7.2 dictates that $\alpha' = 180° - |\alpha| = 86.20680894°$ and $\beta' = \beta$ should be used in the calculations. As α and β are both positive, this means that an offset of 270 degrees must be used. After calculation, one finds $\phi_N = 273.4395°$. This can be used in formula (17) to determine θ_N, which is found to be $93.7932°$. Then $\rho_{e,P}$ can be determined.

$$\rho_{e,P} = \frac{1}{2}\begin{pmatrix} 0.9340 & 0.0599 + 0.9960i \\ 0.0599 - 0.9960i & 1.0660 \end{pmatrix}$$

Discussion and verification of the results

Both of the experimental density operators correspond to some extent to the theoretical one, which is illustrated in figure 34.

The AQST measurement has a fidelity of $F_A^C = 0.9806$ and the PQST measurement has a fidelity of $F_P = 0.9962$. The AQST fidelity is lower than in previous measurements, but this

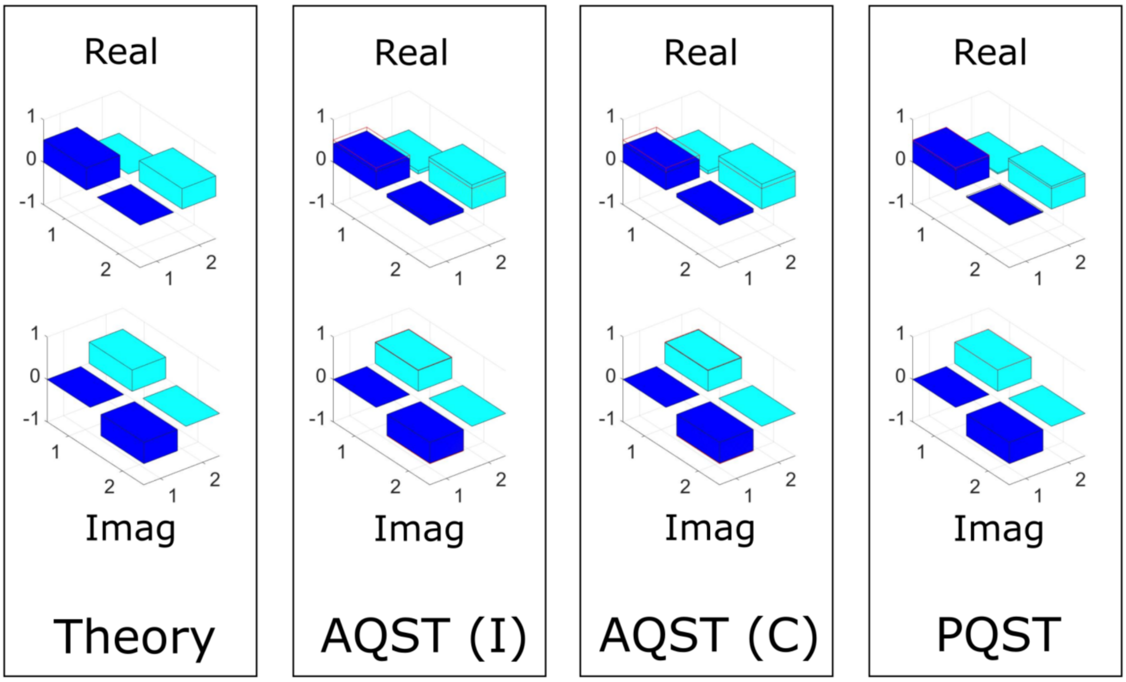

Figure 34: Comparison of the real and imaginary parts of the theoretical density operator with the experimentally determined density operators.

particular state is also harder to measure than the other ones because $|\psi\rangle_N$ was close to the y-axis. Without using the contrast, the AQST fidelity would be slightly higher at $F_A = 0.9863$. The PQST fidelity is high, even if β lies far from its ideal value of zero. This is because ϕ_N is calculated from the ratio of $tan(\beta)$ and $tan(\alpha)$ and α lies close to 90 degrees, making the denominator much bigger than the numerator. Therefore, even if the y-phase cannot be measured as accurately as normally, this does not necessarily matter as long as $\alpha \sim 90°$. The correspondence of the theoretical and experimental states can also be visualized by plotting the theoretical Rabi oscillations on top of the experimental ones, as was also depicted in figure 33. Especially the x-Rabi is close to the theoretical one.

For this particular measurement, the 'worst case' AQST gives angles $\theta_N = 117.7200°$ and $\phi_N = 299.7985°$ and a fidelity of $F_A = 0.8740$ for intensity data, and gives $\theta_N^C = 117.9902°$ and $\phi_N^C = 302.1060°$ and a fidelity of $F_A^C = 0.8638$ for contrast data. The 'worst case' PQST measurement gives angles $\theta_N = 99.7777°$ and $\phi_N = 281.7042°$ and a fidelity of $F_A = 0.9785$.

To quantify the reproducibility of this measurement technique, the presented QST was performed multiple times. However, because of the difficulties explained at the start of this subsection, most measurements were unsuccessful. This could be seen even before the calculations because A_x would become larger than A_R, which is theoretically not possible. If one sees this happening, one could choose to discard the measurement and start new measurements until $A_R > A_x$. Doing this, the above results and fidelity were obtained. Note that even though $A_R > A_x$ for intensity data, the reverse was true for contrast data, so even when one repeats the measurements until $A_R > A_x$, it could still be that the contrast data generates complex coordinates. Therefore, one could also choose to keep the measurement with $A_R < A_x$. The next paragraph illustrates what can happen in such a situation.

What to do when sample drift is clearly present in the QST measurements

Below, the results of a second QST measurement (using intensity data) of the state $|\psi\rangle_N$ with $\theta_N = 87.6°$ and $\phi_N = 270°$ are presented. For generic states, it may be hard to discern whether the amplitude of a certain Rabi measurement has been affected by drift, but for the presented measurement $A_x > A_R$ indicates that A_R is lower than it should be because of drift and no confusion is possible. The presented measurement suffered in particular from sample drift ($A_R << A_x$) and the measured amplitudes as a result do not provide correct information about the quantum state.

$$\begin{aligned}
A_R &= 394.8050 \text{ counts/ s}\\
A_x &= 450.9005 \text{ counts/ s}\\
A_y &= 80.6450 \text{ counts/ s}\\
A_R^C &= 2.2705805\%\\
A_x^C &= 2.188232\%\\
A_y^C &= 0.15691202\%\\
\alpha &= 87.6052°\\
\beta &= 49.5895°
\end{aligned}$$

These fit parameters, together with the fact that x is positive, y is negative and z is positive, can be used to determine θ_N and ϕ_N. Hereby, it must be noted that in the intensity AQST calculations a correction for the negative x^2 value was necessary, and in the contrast AQST calculations for the negative z^2 value. AQST calculations on intensity data give $\theta_N = 62.3661°$ and $\phi_N = 299.4042°$, which results in a low measurement fidelity of $F_A = 0.8953$. Using instead contrast data, the angles $\theta_N = 75.9849°$ and $\phi_N = 284.9765°$ can be determined, resulting in an increased fidelity of $F_A^C = 0.9733$. For PQST, sample drift does not necessarily deteriorate the resulting fidelity. Using α and β as presented, it can be determined that $\theta_N = 87.6081°$ and $\phi_N = 272.8122°$. This lies much closer to the theoretical values and gives a fidelity of $F_p = 0.9994$. It can thus be concluded that the effect of 'bad' amplitudes is mostly confined to AQST and has no visible effect on the fidelity of PQST. Therefore, if one wishes to use AQST, one should rerun the measurement until $A_R > A_x$ (or at least until the difference between A_R and A_x is small) and use contrast data. This is not necessary when one wishes to use PQST.

7.2.4 Summary of QST results

Table 1 summarizes the obtained angles and fidelities for all nuclear states on which tomography was performed. In this way, the results of AQST with intensity or contrast data and PQST can be compared within the measurement of a single nuclear spin state and across all measurements.

Taking the average fidelity of the first five measurements in table 1 (so excluding the limiting cases), the following numbers are found:

$$\begin{aligned} F_A &= 0.9741 \\ F_A^C &= 0.9890 \\ F_P &= 0.9971 \end{aligned}$$

Note that the fourth measurement was severely impacted by sample drift, so calculating the average AQST fidelity without taking this measurement into account results in $F_A = 0.9925$ and $F_A^C = 0.9952$. In this case, the fidelity of each QST protocol is approximately equal to or better than the two-qubit CNOT fidelity measured by Rong et al. [56] in a naturally abundant ^{13}C diamond at room temperature. Lastly, using the final two measurements the limiting average fidelities can be determined as $F_A = 0.9408$, $F_A^C = 0.9770$ and $F_P = 0.9978$. Taking all measurements into account, the average achievable two-qubit fidelity for QST of a general nuclear spin state is given by:

$$\begin{aligned} F_A &= 0.9646 \\ F_A^C &= 0.9856 \\ F_P &= 0.9973 \end{aligned}$$

When taking into account that two of the seven measurements were pushing the limits of the used QST protocols and that another measurement was clearly affected by sample drift, the resulting fidelities (especially for PQST) are high. The fault-tolerant threshold is typically proposed between 10^{-4} and 10^{-2}, depending on both the noise model that is used and the computational overhead [56]. For example, using the so-called fault-tolerant quantum computing, researchers aim to compute accurately even when the used quantum gates have a high error probability (or accordingly, a low fidelity). In 2005 Knill [57] showed that non-trivial quantum computations could be implemented using quantum resources comparable to the digital resources of the computers of that time with fidelities as low as 0.99. Using more involved computational overhead, this could even drop to 0.97, at which point contrast AQST and PQST give results sufficiently below the fault-tolerant threshold, and this at ambient conditions.

Note also that the calculated fidelities are the result of both the creation and subsequent measurement of the nuclear spin state via the electron spin. Therefore, the fidelity is limited by imperfect manipulations of the nuclear spin (for example because of imperfect control fields), interactions between the quantum system and the environment, and imperfect fitting due to residual noise. The fact that the two-qubit fidelity of the electronic readout of the nuclear spin is good, may be due to the quantum non-demolition (QND) nature of the measurement [58]. Such QND measurements are obtained when the Hamiltonian describing the interaction between the observable (in this case the nuclear spin) and the measurement apparatus (in this case the electron spin) commutes with the observable itself. In this case, the coupling between the nuclear and electron spin happens through hyperfine coupling and the approximate Hamiltonian $\hat{H} = DS_z^2 + g\mu_B B_{NV} S_Z + AS_Z I_Z + PI_Z^2$ that was presented in formula (3) clearly commutes with I_Z. As no non-commuting observables are present in the measurement, no uncertainty is introduced to the measurement in this way. This means that the predictability of a subsequent value of a once precisely measured observable is maintained [59]. Keep in mind however, that the QND character of the measurement is only approximate. The hyperfine coupling tensor $\boldsymbol{A}$ also contains contributions perpendicular to the NV axis, which results in spin mixing and quantum jumps (abrupt, discontinuous evolutions of a quantum state). If the jump time is longer than the measurement time, the QND measurement can be deemed successful. This is interesting to investigate in future work.

As a last remark, the adaptation of the presented QST protocols for mixed-state determination is envisioned. This will provide a more complete procedure to determine any nuclear spin state (pure or mixed), which is for example useful for quantum thermodynamic applications.

Table 1: Results of intensity AQST, contrast AQST and PQST calculations for all performed QST measurements.

$\boldsymbol{\theta_N = 58.41^\circ, \phi_N = 249^\circ}$	Measurement 1	Measurement 2	
θ_A	50.3479	58.3851	
ϕ_A	242.0980	243.3618	
F_A	0.9927	0.9982	
θ_A^C	48.1344	57.3224	
ϕ_A^C	247.8780	243.8386	
F_A^C	0.9919	0.9985	
θ_P	60.8178	58.9123	
ϕ_P	248.4340	254.1850	
F_P	0.9995	0.9985	

$\boldsymbol{\theta_N = 137.02^\circ, \phi_N = 53^\circ}$	Measurement 1	Measurement 2	Measurement 3
θ_A	145.3984	100.2758	126.6436
ϕ_A	63.58559	50.6054	42.9581
F_A	0.9914	0.9004	0.9876
θ_A^C	141.4678	115.2077	131.7113
ϕ_A^C	65.5091	53.7838	48.1563
F_A^C	0.9935	0.9642	0.9969
θ_P	136.9100	136.6825	142.7954
ϕ_P	63.4052	48.5976	39.7088
F_P	0.9962	0.9993	0.9919

$\boldsymbol{\theta_N = 87.6^\circ, \phi_N = 270^\circ}$	Measurement 1	Measurement 2	
θ_A	97.5928	62.3661	
ϕ_A	279.0506	299.4042	
F_A	0.9863	0.8953	
θ_A^C	99.9937	75.9849	
ϕ_A^C	280.1492	284.9765	
F_A^C	0.9806	0.9733	
θ_P	93.7932	87.6081	
ϕ_P	273.4395	272.8122	
F_P	0.9962	0.9994	

8 Conclusion

In this master thesis I investigated control and readout protocols of the ^{14}N nuclear spin associated to an NV center with the aim of future implementation in an NV-based quantum Otto engine, for which I discussed the theoretical foundation. In a broader context, this work contributes to the wide range of possible applications of NV centers in quantum thermodynamics and quantum information theory, which can be found in present-day literature.

The presented NV quantum Otto engine is mostly based on the work by Peterson et al. (which was also verified using MatLab simulations), since the system employed there is similar to the two-qubit system consisting of an NV electron and associated ^{14}N nuclear spin. In this cycle, the NV electron spin is used as a heat bus, the associated ^{14}N spin as working substance, MW modes near the electron Larmor frequency ν_e make up the hot environment and RF modes near the ^{14}N Larmor frequency ν_N the cold environment. I presented an initial state preparation of the two nuclear spins theoretically in section 5.7 and have experimentally demonstrated this to certain extent experimentally. The pulse protocol from the NMR-based Otto engine can essentially be used with an adapted coupling mechanism (hyperfine coupling).

To manipulate the electron and ^{14}N nuclear spin of an NV center, control parameters (resonance frequencies and π-pulse durations between different energy levels) had to be determined. For this, I have executed multiple measurements and derived the control parameters by fitting the acquired data. The electronic π-pulse was set at ~ 800 ns, which was verified by Rabi measurements, and at this long duration the hyperfine structure (due to the presence of the ^{14}N nuclear spin) could be resolved in pulsed ODMR measurements of the electronic spin. Narrowband nuclear spin-state selective MW pulses at these resonance frequencies can then be applied to flip the electronic spin depending on the state of the nuclear spin. This enables to manipulate nuclear spins (e.g. polarization) and to perform ENDOR measurements of the ^{14}N spin. For the nuclear spin, the duration of the π-pulse was set at $\sim 16.5\mu$s, which was also verified by Rabi measurements. The resonance frequency of the $|-1,0\rangle \leftrightarrow |-1,1\rangle$ transition was theoretically predicted to be ~ 7.11 MHz, which was verified using a nuclear ODMR protocol. The linewidth of this resonance was sufficiently broad to excite the $|0,-1\rangle \leftrightarrow |1,-1\rangle$ transition as well. The $|0,0\rangle \leftrightarrow |,1\rangle$ transition at ~ 4.95 MHz was also probed with nuclear ODMR.

With the electronic and nuclear control parameters in hand, the NV two-qubit system could be polarized to the $|0, 0\rangle$ state. After ENDOR readout, it was seen that the system was not completely polarized, but some population remained in the $m_I = \pm 1$ states. However, since the difference in contrast between the $|0\rangle_N$ ($C = \sim 19\%$) and $|0, \pm\rangle_N$ ($C = \sim 6.5\%$) resonances was $\sim 12.5\%$, the polarization is still sufficient. Then, I used this polarization sequence to generate nuclear Rabi oscillations with a higher contrast. For a perfect polarization, the contrast should increase threefold compared to the depolarized case. As the polarization was imperfect, the contrast increase was limited to approximately twofold. In future works, this polarization could be optimized by measuring the duration of the RF and MW π-pulses more precisely. This could be done using very long measurements (using large τ) providing a lot of Rabi periods.

Besides the necessary control parameters, I optimized other aspects of the pulse protocols as well to provide a good control of the nuclear and electronic spin. For example, the duration of the laser pulse responsible for the electronic spin flip from $m_S = \pm 1$ to $m_S = 0$ in the polarization protocol was optimized so that the required spin flip took place, but the nuclear spin was unaffected. Using a laser power of 1 mW, an optimal duration of 500 ns was found. In a further study, it is interesting to look at the duration of the initializing laser pulse of each sequence as well, since it was discovered to be too short to fully depolarize the nuclear spin. I also investigated the effects of the application of RF waves, namely the shift in resonance frequencies and drift of the diamond sample. With application of more (or longer) RF waves, the resonance frequencies shift more towards lower values. This is a shift in zero-field splitting as both the $|0\rangle_e \leftrightarrow |-1\rangle_e$ and $|0\rangle_e \leftrightarrow |1\rangle_e$ transition frequencies shift in the same direction. To overcome this problem, each measurement using RF waves was preceded by the same measurement protocol using off-resonance RF waves in presence of a swept MW field, indicating the RF modified resonance frequencies. The sample drift was also found to increase when the amount of applied RF fields increased. This was partly solved by implementing a function in the software to keep the NV center in focus by comparing measured PL intensities at all times and correcting the position of the laser focus when this intensity changed too much ($> 50\%$).

For the last experimental step, I created three different generic nuclear spin states $|\psi\rangle_N = cos(\frac{\theta_N}{2}) + e^{i\phi_N} sin(\frac{\theta_N}{2})$ and performed a subsequent tomography of this state. I have executed the measurement protocol and have modeled the data using the theory devised in section 5.6 for three nuclear states. Two of these states used randomly selected angles: ($\theta_N = 58.41$,

$\phi_N = 249$) and ($\theta_N = 237.02$, $\phi_N = 53$), the third state was chosen in the vicinity of the negative y-axis on the Bloch sphere to test the limits of the used QST protocol. I have measured the fidelity of the newly designed protocols and have demonstrated the overall superiority of the PQST method compared to the AQST method with a maximum fidelity of $F_P^{max} = 0.9995$ and an average fidelity (over seven measurements of the three mentioned states) of $F_P^{avg} = 0.9973$. This is close to the limits needed to execute effectively quantum error correction protocols, which is considered as a benchmark for executing computational operations and scaling up the quantum system. For the AQST calculations, two different methods were used. The first one determined the amplitudes of the Rabi oscillations using the PL intensity as measured, whereas the second one used the contrast amplitude. Because the presence of sample drift lowers the intensity measured, but does not affect the contrast, the second method was best suitable. With this method, I obtained a maximum two-qubit fidelity of $F_A^{C,max} = 0.9985$ (compare with $F_A^{max} = 0.9982$ for intensity data) and an average fidelity of $F_A^{C,avg} = 0.9856$ (compare with $F_A^{avg} = 0.9646$). Note that the maximum fidelities are not far apart, since the measurement for which they were obtained suffered little from sample drift. However, other measurements did, so the difference between the average fidelities is larger. Note also that these fidelities express how well a nuclear state could be created and then read out through the electron spin, as the used protocol combined the creation of a specific state and subsequent tomography. In future works, this state preparation could be decoupled from the QST measurement scheme, and the obtained fidelities could be compared to the ones obtained here. These QST protocols are essential to characterize the expansion and compression protocols in NV-based quantum Otto engines. In addition, the possibility of creating a protocol for mixed state QST can be investigated. This would make QST useful for validating thermal states in the quantum Otto cycle as well.

9 Acknowledgements

To start, I would like to express my gratitude to prof. dr. Milos Nesladek, without whom this project would not have been possible. I am extremely thankful to have been able to conduct my master thesis on the topic of NV centers, in which I am very much interested, and appreciate the opportunity given to me by prof. Nesladek, as well as all of his helpful remarks, advice and sharing of his expertise in the field. In this regard, I would also like to pay my special regards to prof. dr. Jacques Tempere of Antwerp University, who has kindly agreed to be my copromotor and who has given me the chance to present my work for him and his colleagues in Antwerp, while also helping me with the formalities of my thesis submission. For his help in guiding me through the principles of quantum thermodynamics, quantum heat engines and counteradiabatic driving, and for his most helpful remarks on my experimental progress and the design of an NV-based quantum Otto engine prototype, I would like to express my sincere gratitude to dr. Abhishek Shukla, my second copromotor. Special thanks also to PhD student Michael Petrov, who has been a tremendous help in working with the experimental set-up, understanding the software and implementing the pulse protocols, while also commenting on my progress. Finally, I am grateful to my parents and my friend Remy Vandebosch for proofreading my thesis.

References

[1] R. Kosloff and A. Levy, “Quantum Heat Engines and Refrigerators : Continuous Devices,” *Annu. Rev. Phys. Chem.*, vol. 65, no. 93, pp. 365–393, 2014.

[2] F. Binder and L. A. Correa, *Thermodynamics in the Quantum Regime*. Cham: Springer Nature Switzerland AG, 195 ed., 2018.

[3] S. Deffner and S. Campbell, *An introduction to the thermodynamics of quantum information*. San Rafael,: Morgan & Claypool Publishers, 2019.

[4] B. Çakmak, “Finite-time two-spin quantum Otto engines: Shortcuts to adiabaticity vs. Irreversibility,” *Turkish Journal of Physics*, vol. 45, no. 1, pp. 59–73, 2021.

[5] L. Childress and R. Hanson, “Diamond NV centers for quantum computing and quantum networks,” *MRS Bulletin*, vol. 38, no. 2, pp. 134–138, 2013.

[6] P. C. Maurer, G. Kucsko, C. Latta, L. Jiang, N. Y. Yao, S. D. Bennett, F. Pastawski, D. Hunger, N. Chisholm, M. Markham, D. J. Twitchen, J. I. Cirac, and M. D. Lukin, “Room-temperature quantum bit memory exceeding one second,” *Science*, vol. 336, no. 6086, pp. 1283–1286, 2012.

[7] J. Cramer, N. Kalb, M. A. Rol, B. Hensen, M. S. Blok, M. Markham, D. J. Twitchen, R. Hanson, and T. H. Taminiau, “Repeated quantum error correction on a continuously encoded qubit by real-time feedback,” *Nature Communications*, vol. 7, no. May, pp. 1–7, 2016.

[8] T. Xie, Z. Zhao, X. Kong, W. Ma, M. Wang, X. Ye, P. Yu, Z. Yang, S. Xu, P. Wang, Y. Wang, F. Shi, and J. Du, “Beating the standard quantum limit under ambient conditions with solid-state spins,” *Science Advances*, vol. 7, no. 32, pp. 1–11, 2021.

[9] K. Ullah, E. Köse, M. C. Onbaşlı, and Ö. E. Müstecaplıoğlu, “Steady state entanglement of distant nitrogen-vacancy centers in a coherent thermal magnon bath,” pp. 1–19, 2021.

[10] Y. Zhou, B. Li, X. X. Li, F. L. Li, and P. B. Li, “Preparing multiparticle entangled states of nitrogen-vacancy centers via adiabatic ground-state transitions,” *Physical Review A*, vol. 98, no. 5, pp. 1–11, 2018.

[11] J. W. Zhou, P. F. Wang, F. Z. Shi, P. Huang, X. Kong, X. K. Xu, Q. Zhang, Z. X. Wang, X. Rong, and J. F. Du, “Quantum information processing and metrology with color centers in diamonds,” *Frontiers of Physics*, vol. 9, no. 5, pp. 587–597, 2014.

[12] J. Zhang, S. S. Hegde, and D. Suter, “Efficient Implementation of a Quantum Algorithm in a Single Nitrogen-Vacancy Center of Diamond,” *Physical Review Letters*, vol. 125, no. 3, pp. 1–13, 2020.

[13] X. L. Ouyang, X. Z. Huang, Y. K. Wu, W. G. Zhang, X. Wang, H. L. Zhang, L. He, X. Y. Chang, and L. M. Duan, “Experimental demonstration of quantum-enhanced machine learning in a nitrogen-vacancy-center system,” *Physical Review A*, vol. 101, no. 1, pp. 1–6, 2020.

[14] J. Jiang and Q. Chen, “Selective nuclear-spin interaction based on a dissipatively stabilized nitrogen-vacancy center,” 2022.

[15] L. Schlipf, T. Oeckinghaus, K. Xu, D. B. R. Dasari, A. Zappe, F. F. De Oliveira, B. Kern, M. Azarkh, M. Drescher, M. Ternes, K. Kern, J. Wrachtrup, and A. Finkler, “A molecular quantum spin network controlled by a single qubit,” *Science Advances*, vol. 3, no. 8, pp. 3–10, 2017.

[16] J. Klatzow, J. N. Becker, P. M. Ledingham, C. Weinzetl, K. T. Kaczmarek, D. J. Saunders, J. Nunn, I. A. Walmsley, R. Uzdin, and E. Poem, “Experimental Demonstration of Quantum Effects in the Operation of Microscopic Heat Engines,” *Physical Review Letters*, vol. 122, no. 11, pp. 1–34, 2019.

[17] S. Hernández-Gómez, N. Staudenmaier, M. Campisi, and N. Fabbri, “Experimental test of fluctuation relations for driven open quantum systems with an NV center,” *New Journal of Physics*, vol. 23, no. 6, 2021.

[18] S. Hernández-Gómez, S. Gherardini, N. Staudenmaier, F. Poggiali, M. Campisi, A. Trombettoni, F. S. Cataliotti, P. Cappellaro, and N. Fabbri, “Autonomous dissipative Maxwell’s demon in a diamond spin qutrit,” pp. 1–19, 2021.

[19] Gordon Davies, *Diamond*. Bristol: Hilger, 1984.

[20] C. Teale, “Magnetometry with Ensembles of Nitrogen Vacancy Centers in Bulk Diamond,” no. 2000, pp. 1–195, 2017.

[21] L. Rondin, J. P. Tetienne, T. Hingant, J. F. Roch, P. Maletinsky, and V. Jacques, “Magnetometry with nitrogen-vacancy defects in diamond,” *Reports on Progress in Physics*, vol. 77, no. 5, 2014.

[22] P. Deák, B. Aradi, M. Kaviani, T. Frauenheim, and A. Gali, “The formation of NV centers in diamond: A theoretical study based on calculated transitions and migration of nitrogen and vacancy related defects,” pp. 1–20, 2013.

[23] N. Wang, C. F. Liu, J. W. Fan, X. Feng, W. H. Leong, A. Finkler, A. Denisenko, J. Wrachtrup, Q. Li, and R. B. Liu, “Zero-field magnetometry using hyperfine-biased nitrogen-vacancy centers near diamond surfaces,” *Physical Review Research*, vol. 4, no. 1, pp. 1–33, 2022.

[24] A. K. Dmitriev and A. K. Vershovskii, “High-contrast two-quantum optically detected resonances in NV centers in diamond in zero magnetic field,” no. 1, pp. 3–6, 2019.

[25] T. Chakraborty, J. Zhang, and D. Suter, “Polarizing the electronic and nuclear spin of the NV-center in diamond in arbitrary magnetic fields: Analysis of the optical pumping process,” *New Journal of Physics*, vol. 19, no. 7, p. 73030, 2017.

[26] ChEBI, “CHEBI:36938 - nitrogen-14 atom.”

[27] L. Robledo, H. Bernien, T. V. D. Sar, and R. Hanson, “Spin dynamics in the optical cycle of single nitrogen-vacancy centres in diamond,” *New Journal of Physics*, vol. 13, 2011.

[28] J. P. Tetienne, L. Rondin, P. Spinicelli, M. Chipaux, T. Debuisschert, J. F. Roch, and V. Jacques, “Magnetic-field-dependent photodynamics of single NV defects in diamond: An application to qualitative all-optical magnetic imaging,” *New Journal of Physics*, vol. 14, 2012.

[29] E. Bourgeois, M. Gulka, and M. Nesladek, “Photoelectric Detection and Quantum Readout of Nitrogen-Vacancy Center Spin States in Diamond,” *Advanced Optical Materials*, vol. 8, no. 12, pp. 1–29, 2020.

[30] L. Kulik and W. Lubitz, “Electron-nuclear double resonance,” *Photosynthesis Research*, vol. 102, no. 2, pp. 391–401, 2009.

[31] J. F. Barry, J. M. Schloss, E. Bauch, M. J. Turner, C. A. Hart, L. M. Pham, and R. L. Walsworth, "Sensitivity optimization for NV-diamond magnetometry," *Reviews of Modern Physics*, vol. 92, no. 1, 2020.

[32] I. S. Oliveira, T. J. Bonagamba, R. S. Sarthour, J. C. Freitas, and E. R. DeAzevedo, "Fundamentals of Quantum Computation and Quantum Information," *NMR Quantum Information Processing*, pp. 93–136, 2007.

[33] A. Harrow, "Quantum states and operations Administrivia Basics : States , operations , metrics," tech. rep., 2018.

[34] T. Dft, "Definition and properties of tensor products," pp. 212–225, 2012.

[35] D. Vrancken, *Quantum state tomography of electron and nuclear spin in NV center*. PhD thesis, Hasselt University, 2021.

[36] E. M. Fortunato, M. A. Pravia, N. Boulant, G. Teklemariam, T. F. Havel, and D. G. Cory, "Design of strongly modulating pulses to implement precise effective Hamiltonians for quantum information processing," *Journal of Chemical Physics*, vol. 116, no. 17, pp. 7599–7606, 2002.

[37] H. B. Callen, *Thermodynamics and an introduction to thermostatistics*. John Wiley & sons, second edi ed., 1985.

[38] F. Binder, S. Vinjanampathy, K. Modi, and J. Goold, "Quantum thermodynamics of general quantum processes," pp. 1–6, 2015.

[39] A. Abragam and W. G. Proctor, "Spin temperature," *Physical Review*, vol. 109, no. 5, pp. 1441–1458, 1958.

[40] F. J. Peña, O. Negrete, N. Cortés, and P. Vargas, "Otto engine: Classical and quantum approach," *Entropy*, vol. 22, no. 7, pp. 1–7, 2020.

[41] T. D. Kieu, "Quantum heat engines, the second law and Maxwell's daemon," *European Physical Journal D*, vol. 39, no. 1, pp. 115–128, 2006.

[42] B. Çakmak and Ö. E. Müstecaplloğlu, "Spin quantum heat engines with shortcuts to adiabaticity," *Physical Review E*, vol. 99, no. 3, pp. 1–10, 2019.

[43] M. V. Berry, “Transitionless quantum driving,” *Journal of Physics A: Mathematical and Theoretical*, vol. 42, no. 36, pp. 1–9, 2009.

[44] R. Uzdin, A. Levy, and R. Kosloff, “Equivalence of quantum heat machines, and quantum-thermodynamic signatures,” *Physical Review X*, vol. 5, no. 3, pp. 1–21, 2015.

[45] R. Uzdin, A. Levy, and R. Kosloff, “Quantum heat machines equivalence, work extraction beyond markovianity, and strong coupling via heat exchangers,” *Entropy*, vol. 18, no. 4, 2016.

[46] J. P. Peterson, T. B. Batalhão, M. Herrera, A. M. Souza, R. S. Sarthour, I. S. Oliveira, and R. M. Serra, “Experimental Characterization of a Spin Quantum Heat Engine,” *Physical Review Letters*, vol. 123, no. 24, p. 240601, 2019.

[47] J. P. Peterson, T. B. Batalhão, M. Herrera, A. M. Souza, R. S. Sarthour, I. S. Oliveira, and R. M. Serra, “Experimental Characterization of a Spin Quantum Heat Engine,” *Physical Review Letters*, vol. 123, no. 24, pp. 1–6, 2019.

[48] M. A Morrison and G. A Parker, “A Guide to Rotations in Quantum Mechanics,” *Australian Journal of Physics*, vol. 40, no. 4, p. 465, 1987.

[49] t. The NIST Reference on Constants, Units, and Uncertainty, “Electron gyromagnetic ratio,” 2018.

[50] M. Mirdrikvand, *NMR Methods for Characterization of Mass Transport and Reaction Processes in Porous Materials.* PhD thesis, 2020.

[51] Y. Sun, J.-Y. Zhang, M. S. Byrd, and L.-A. Wu, “Adiabatic Quantum Simulation Using Trotterization,” vol. 2, no. 1, pp. 1–5, 2018.

[52] N. Bar-Gill, L. M. Pham, A. Jarmola, D. Budker, and R. L. Walsworth, “Solid-state electronic spin coherence time approaching one second,” *Nature Communications*, vol. 4, 2013.

[53] P. Neumann, J. Beck, M. Steiner, F. Rempp, H. Fedder, P. R. Hemmer, J. Wrachtrup, and F. Jelezko, “Single-shot readout of a single nuclear spin,” *Science*, vol. 329, no. 5991, pp. 542–544, 2010.

[54] P. Wang, Z. Yuan, P. Huang, X. Rong, M. Wang, X. Xu, C. Duan, C. Ju, F. Shi, and J. Du, "High-resolution vector microwave magnetometry based on solid-state spins in diamond," *Nature Communications*, vol. 6, pp. 1–5, 2015.

[55] V. K. Sewani, H. H. Vallabhapurapu, Y. Yang, H. R. Firgau, C. Adambukulam, B. C. Johnson, J. J. Pla, and A. Laucht, "Coherent control of NV- centers in diamond in a quantum teaching lab," *American Journal of Physics*, vol. 88, no. 12, pp. 1156–1169, 2020.

[56] X. Rong, J. Geng, F. Shi, Y. Liu, K. Xu, W. Ma, F. Kong, Z. Jiang, Y. Wu, and J. Du, "Experimental fault-tolerant universal quantum gates with solid-state spins under ambient conditions," *Nature Communications*, vol. 6, 2015.

[57] E. Knill, "Quantum computing with realistically noisy devices," *Nature*, vol. 434, no. 7029, pp. 39–44, 2005.

[58] J. J. Pla, K. Y. Tan, J. P. Dehollain, W. H. Lim, J. J. Morton, F. A. Zwanenburg, D. N. Jamieson, A. S. Dzurak, and A. Morello, "High-fidelity readout and control of a nuclear spin qubit in silicon," *Nature*, vol. 496, no. 7445, pp. 334–338, 2013.

[59] C. S. Unnikrishnan, "Quantum non-demolition measurements: concepts, theory and practice," *Current Science*, vol. 109, no. 11, pp. 2052–2060, 2015.

A Derivation of the general CD Hamiltonian

In section 5.7.4, formula (40) gives a general expression for the counteradiabatic driving Hamiltonian. Using Berry's work [43] as a reference, the expression for $\hat{H}_{CD}$ is now derived using formula (37) as a starting point. This formula expresses the time independent Schrödinger equation for a general quantum system evolving under Hamiltonian $\hat{H}_0(t)$.

$$\hat{H}_0(t)|n(t)\rangle = E_n(t)|n(t)\rangle \tag{A1}$$

As stated, in the adiabatic approximation, the states driven by $\hat{H}_0(t)$ are:

$$|\psi_n(t)\rangle = \exp\Big[\tfrac{1}{i\hbar}\textstyle\int_0^t dt' E_n(t') - \int_0^t dt' \langle n(t')|\delta_{t'} n(t')\rangle\Big]|n(t)\rangle \tag{A2}$$

The goal now is to find a counteradiabatic driving Hamiltonian $\hat{H}_{CD}(t)$, so that the previous states are eigenvalues of this Hamiltonian (and therefore, no transitions can happen, even at finite time driving). To find the expression for $\hat{H}_{CD}(t)$, it is instructive to inspect first the unitary operator $\hat{U}(t)$ given in the following formula:

$$\hat{U}(t) = \textstyle\sum_n \exp\Big[\tfrac{1}{i\hbar}\int_0^t dt' E_n(t') - \int_0^t dt' \langle n(t')|\delta_{t'} n(t')\rangle\Big]|n(t)\rangle\langle n(0)| \tag{A3}$$

If the system is in state $|n(0)\rangle$ before the driving, then applying $\hat{U}(t)$ generates the state $|\psi_n(t)\rangle$. Then to find a Hamiltonian which will cause exactly this behavior, one can solve the Schrodinger equation using $\hat{U}(t)$ (as this is just the regular Schrödinger equation multiplied by $\langle n(0)|$ on the right).

$$\begin{aligned} i\hbar\delta_t\hat{U}(t) &= \hat{H}_{CD}(t)\hat{U}(t) && \text{(A4)} \\ \Rightarrow \quad \hat{H}_{CD}(t) &= i\hbar(\delta_t\hat{U}(t))\hat{U}^\dagger(t) && \text{(A5)} \end{aligned}$$

Formula (A3) can be substituted into formula (A5) as follows:

$$\begin{aligned} \hat{H}_{CD}(t) &= i\hbar\exp\Big[\tfrac{1}{i\hbar}\textstyle\int_0^t dt'(E_n(t') - E_m(t')) - \int_0^t dt'(\langle n(t')|\delta_{t'} n(t')\rangle - \langle m(t')|\delta_{t'} m(t')\rangle)\Big]\cdot \\ &\quad \textstyle\sum_n(|\delta_t n(t)\rangle\langle n(0)| + \frac{E_n(t)}{i\hbar}|n(t)\rangle\langle n(0)| - \langle n(t')|\delta_{t'} n(t')\rangle|n(t)\rangle\langle n(0)|)\cdot \\ &\quad \textstyle\sum_m |m(0)\rangle\langle m(t)| \\ &= i\hbar\textstyle\sum_n \frac{E_n(t)}{i\hbar}|n(t)\rangle\langle n(t)| + |\delta_t n(t)\rangle\langle n(t)| - \langle n(t')|\delta_{t'} n(t')\rangle|n(t)\rangle\langle n(t)| \end{aligned} \tag{A6}$$

To go from the first step to the second, one uses that $\langle n(0)|m(0)\rangle = \delta_{nm}$. Furthermore, the following expressions were used:

$$\hat{U}^{\dagger}(t) = \sum_n \exp\left[\tfrac{-1}{i\hbar}\int_0^t dt' E_n(t') + \int_0^t dt' \langle n(t')|\delta_{t'} n(t')\rangle\right] |n(0)\rangle\langle n(t)|$$

$$\begin{aligned} \delta_t \hat{U}(t) &= \sum_n \exp\left[\tfrac{1}{i\hbar}\int_0^t dt' E_n(t') - \int_0^t dt' \langle n(t')|\delta_{t'} n(t')\rangle\right] \\ &\quad \left(|\delta_t n(t)\rangle\langle n(0)| + \tfrac{E_n(t)}{i\hbar}|n(t)\rangle\langle n(0)| - \langle n(t')|\delta_{t'} n(t')\rangle |n(t)\rangle\langle n(0)|\right) \end{aligned}$$

This proves formula (40).

B Derivation of the CD Hamiltonian for 1/2-spins in an ambient magnetic field

A spin in an ambient magnetic field $\boldsymbol{B}_0(t)$ can be described by the following Hamiltonian:

$$\hat{H}_0(t) = \gamma \boldsymbol{B}_0(t) \cdot \hat{\boldsymbol{S}} \quad \text{(B1)}$$

Here, γ is the gyromagnetic ratio of the spin of interest and $\hat{\boldsymbol{S}}$ is the spin vector operator of this particular particle. As $H_{CD}(t)$ is derived in particular for $S = 1/2$ particles, this operator is given by:

$$\hat{\boldsymbol{S}} = \frac{\hbar}{2}\begin{pmatrix} 0 & 1 \\ 1 & 0 \end{pmatrix}\hat{\imath} + \frac{\hbar}{2}\begin{pmatrix} 0 & -i \\ i & 0 \end{pmatrix}\hat{\jmath} + \frac{\hbar}{2}\begin{pmatrix} 1 & 0 \\ 0 & -1 \end{pmatrix}\hat{k} \quad \text{(B2)}$$

From equation (42), taking $\boldsymbol{B}_0(t)$ in the z-direction for now, the extra term $\hat{H}_1(t)$ in the counteradiabatic driving Hamiltonian is given by:

$$\hat{H}_1(t) = i\hbar\gamma\delta_t \boldsymbol{B}_0(t) \textstyle\sum_{n=-1/2}^{1/2} \sum_{m\neq n} \displaystyle\frac{|m(t)\rangle\langle m(t)|\hat{\boldsymbol{S}}|n(t)\rangle\langle n(t)|}{E_n(t) - E_m(t)} \quad \text{(B3)}$$

In this formula, the energy is given by (where $B_0(t)$ is the magnitude of $\boldsymbol{B}_0(t)$):

$$E_n(t) = \gamma\hbar n B_0(t) \quad \text{(B4)}$$

Expanding the summations and inserting this into the formula (B3) gives:

$$\hat{H}_1(t) = \frac{i}{B_0(t)}\delta_t \boldsymbol{B}_0(t)[|\downarrow(t)\rangle\langle\downarrow(t)|\hat{\boldsymbol{S}}|\uparrow(t)\rangle\langle\uparrow(t)| - |\uparrow(t)\rangle\langle\uparrow(t)|\hat{\boldsymbol{S}}|\downarrow(t)\rangle\langle\downarrow(t)|] \quad \text{(B5)}$$

The matrix elements are given by:

$$\begin{aligned} \langle\downarrow(t)|\hat{\boldsymbol{S}}|\uparrow(t)\rangle &= \langle\downarrow(t)|\hat{S}_x\hat{\imath} + \hat{S}_y\hat{\jmath}|\uparrow(t)\rangle \\ &= \frac{\hbar}{2}(\hat{\imath} + i\hat{\jmath}) && \text{(B6)} \\ \langle\uparrow(t)|\hat{\boldsymbol{S}}|\downarrow(t)\rangle &= \langle\uparrow(t)|\hat{S}_x\hat{\imath} + \hat{S}_y\hat{\jmath}|\downarrow(t)\rangle \\ &= \frac{\hbar}{2}(\hat{\imath} - i\hat{\jmath}) && \text{(B7)} \end{aligned}$$

Formulas (B6) and (B7) were determined using the general formulas for matrix elements of Pauli spin operators:

$$\begin{aligned} \langle n \pm 1|\hat{S}_x|n\rangle &= \frac{\hbar}{2}\sqrt{s(s+1) - n(n\pm 1)} && \text{(B8)} \\ \langle n \pm 1|\hat{S}_y|n\rangle &= \mp\frac{i\hbar}{2}\sqrt{s(s+1) - n(n\pm 1)} && \text{(B9)} \end{aligned}$$

Before $\hat{H}_{CD}$ can be determined, only $|\downarrow(t)\rangle\langle\uparrow(t)|$ and $|\uparrow(t)\rangle\langle\downarrow(t)|$ must be calculated. This is done in the following basis:

$$|\uparrow(t)\rangle = \begin{pmatrix}1\\0\end{pmatrix} \quad \text{and} \quad |\downarrow(t)\rangle = \begin{pmatrix}0\\1\end{pmatrix} \qquad \text{(B10)}$$

Giving:

$$|\downarrow(t)\rangle\langle\uparrow(t)| = \begin{pmatrix}0&0\\1&0\end{pmatrix} \quad \text{and} \quad |\uparrow(t)\rangle\langle\downarrow(t)| = \begin{pmatrix}0&1\\0&0\end{pmatrix} \qquad \text{(B11)}$$

Substituting (B6), (B7) and (B11) into (B5) gives the proof of formula (44) for spin $1/2$ systems:

$$\begin{aligned}
\hat{H}_1(t) &= \tfrac{i}{B_0(t)}\delta_t\boldsymbol{B}_0(t)[\tfrac{\hbar}{2}(\hat{\imath}+i\hat{\jmath})\begin{pmatrix}0&0\\1&0\end{pmatrix} - \tfrac{\hbar}{2}(\hat{\imath}-i\hat{\jmath})\begin{pmatrix}0&1\\0&0\end{pmatrix}]\\
&= \tfrac{1}{B_0(t)}\delta_t\boldsymbol{B}_0(t)[\tfrac{\hbar}{2}(i\hat{\imath}-\hat{\jmath})\begin{pmatrix}0&0\\1&0\end{pmatrix} - \tfrac{\hbar}{2}(i\hat{\imath}+\hat{\jmath})\begin{pmatrix}0&1\\0&0\end{pmatrix}]\\
&= \tfrac{1}{B_0(t)}\delta_t\boldsymbol{B}_0(t)[\tfrac{\hbar}{2}\begin{pmatrix}0&-i\\i&0\end{pmatrix}\hat{\imath} - \tfrac{\hbar}{2}\begin{pmatrix}0&1\\1&0\end{pmatrix}\hat{\jmath}]\\
&= \tfrac{1}{B_0}\delta_t\boldsymbol{B}_0[\hat{S}_y\hat{\imath} - \hat{S}_x\hat{\jmath}]\\
&= \tfrac{1}{B_0}(\delta_t B_{0,x}S_y - \delta_t B_{0,y}S_x) \qquad \text{(B12)}
\end{aligned}$$

Although this result was derived for spin $1/2$ systems, it is valid for all possible S. Reverting back to general axes, formula (B12) can be expressed as:

$$\begin{aligned}
\hat{H}_1(t) &= \tfrac{1}{B_0^2}\delta_t\boldsymbol{B}_0 \times \boldsymbol{S}\cdot\boldsymbol{B_0}\\
&= \tfrac{1}{B_0^2}\boldsymbol{B}_0 \times \delta_t\boldsymbol{B_0}\cdot\boldsymbol{S} \qquad \text{(B13)}
\end{aligned}$$

Equation (B12) can be found back from (B13) by carrying out the cross and scalar product and then taking the z-component ($\boldsymbol{B}_0(t) = B_0(t)\hat{k}$). Together with the expression for $\hat{H}_0(t)$, the full counteradiabatic driving Hamiltonian is then given by (B14) below, which concludes the proof of formula (44).

$$\begin{aligned}
\hat{H}_{CD}(t) &= \hat{H}_0(t) + \hat{H}_1(t)\\
&= [\gamma\boldsymbol{B}_0(t) + \tfrac{1}{B_0(t)^2}\boldsymbol{B}_0(t)\times\delta_t\boldsymbol{B}_0(t)]\cdot\boldsymbol{S} \qquad \text{(B14)}
\end{aligned}$$